



저작자표시-비영리-변경금지 2.0 대한민국

이용자는 아래의 조건을 따르는 경우에 한하여 자유롭게

- 이 저작물을 복제, 배포, 전송, 전시, 공연 및 방송할 수 있습니다.

다음과 같은 조건을 따라야 합니다:



저작자표시. 귀하는 원저작자를 표시하여야 합니다.



비영리. 귀하는 이 저작물을 영리 목적으로 이용할 수 없습니다.



변경금지. 귀하는 이 저작물을 개작, 변형 또는 가공할 수 없습니다.

- 귀하는, 이 저작물의 재이용이나 배포의 경우, 이 저작물에 적용된 이용허락조건을 명확하게 나타내어야 합니다.
- 저작권자로부터 별도의 허가를 받으면 이러한 조건들은 적용되지 않습니다.

저작권법에 따른 이용자의 권리는 위의 내용에 의하여 영향을 받지 않습니다.

이것은 [이용허락규약\(Legal Code\)](#)을 이해하기 쉽게 요약한 것입니다.

[Disclaimer](#)

Doctoral Thesis

Study on Growth of Two-Dimensional Transition
Metal Dichalcogenides on Graphene: The Interface-
Driven Defects and Properties Relationship

Jung Hwa Kim

Department of Materials Science and Engineering

Graduate School of UNIST

2020

Study on Growth of Two-Dimensional Transition
Metal Dichalcogenides on Graphene: The Interface-
Driven Defects and Properties Relationship

Jung Hwa Kim

Department of Materials Science and Engineering

Graduate School of UNIST

Study on Growth of Two-Dimensional Transition Metal Dichalcogenides on Graphene: The Interface- Driven Defects and Properties Relationship

A thesis/dissertation
submitted to the Graduate School of UNIST
in partial fulfillment of the
requirements for the degree of
Doctor of Philosophy

Jung Hwa Kim

12.03.2019

Approved by



Advisor

Zonghoon Lee

Study on Growth of Two-Dimensional Transition Metal Dichalcogenides on Graphene: The Interface- Driven Defects and Properties Relationship

Jung Hwa Kim

This certifies that the thesis/dissertation of Jung Hwa Kim is approved.

12.03.2019

Signature



Advisor: Zonghoon Lee

Signature



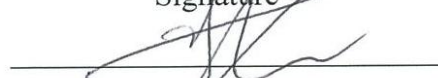
Soon-Yong Kwon: Thesis Committee Member #1

Signature



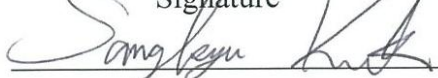
Hyung-Joon Shin: Thesis Committee Member #2

Signature



Jung-Woo Yoo: Thesis Committee Member #3

Signature



Sang Kyu Kwak: Thesis Committee Member #4

ABSTRACT

Vertically stacked heterostructures based on the different types of two-dimensional (2D) materials *via* van der Waals (vdW) interaction have been extensively researched due to their novel properties beyond the limitations of individual 2D materials. The development of chemical vapor deposition (CVD) method enables the fabrication of various vdW heterostructures with clean interface and mass production, compared to the conventional multiple transfer method. Given the 2D nature of these materials, the interface intrinsically plays an important role in modulating or modifying their properties. For example, graphene placed on hexagonal boron nitride shows high charge carrier mobility, but a non-negligible interaction leads to the observation of “Hofstadter’s butterfly”. In addition, in the case of transition metal dichalcogenides (TMDs), the transition from the direct band gap to the indirect band gap is apparent when the thickness increases due to the interface effect. Therefore, a systematic understanding of the impact of the interface on the intrinsic characteristics and performances of the vdW heterostructures is required in order to design desirable properties and expand the scope of applications of the vdW heterostructure.

It is well known that the structural features of the underlying substrate significantly affect the growth behavior and even the unique properties of the heterostructures. Therefore, in this dissertation, I studied novel defects in TMDs induced by an underlying graphene template with various structural features. For this research, I prepared 3 types of graphene templates: 1) Pristine, 2) wrinkle-rich, and 3) nanocrystalline graphene (ncG). Pristine graphene is a good substrate for synthesizing TMDs without dangling bonds and without friction. In addition, when TMDs grow on pristine graphene, the anti-phase boundaries (APBs) of the TMDs are generated more predominantly than the tilted grain boundaries (GBs) due to vdW epitaxial growth. Using this heterostructure, we discovered the anisotropic features of the APBs according to transition-metal-facing (saw-toothed) or chalcogen-facing (straight) APBs, and both types of APBs show metallic properties despite different in-plane charge mobility. Wrinkles in graphene cause significant friction due to out-of-plane deformation and result in AB/AC stacking boundaries (SBs) in epi-TMD layer driven by Shockley partial dislocations. AB/AC SB has a buckled structure for releasing in-plane strain and results in monolayer-like behavior by reducing interlayer coupling. Finally, ncG has lots of dangling bond based active sites for multilayer growth. Due to the diffusion limited growth regime on the ncG template, the synthesized WSe₂ domain shows a fractal morphology with many Se-terminated edge states. The WSe₂/ncG heterostructure shows a downshifted work function similar to the valence band maximum of WSe₂, resulting in a small Schottky barrier height at the metal-semiconductor-junction.

Interface-driven novel defects and their corresponding properties are mainly observed using multi-mode of transmission electron microscopy (TEM) and other surface analysis tools (*e.g.* Raman, x-ray spectroscopy, atomic force microscopy). Theoretical density functional theory (DFT) calculations and

TEM image simulations were supported to identify thermodynamically stable defect configurations and to confirm the exact atomic structures of novel defects. These studies could provide a systematic understanding of defect engineering, especially interface-driven defect formation mechanisms, atomic configurations, and their corresponding properties. It could pave the way for achieving and expanding the manipulation and commercialization of 2D material-based devices *via* defect engineering.

CONTENTS

ABSTRACT	i
LIST OF FIGURES.....	v
LIST OF TABLES	vii
LIST OF ABBREVIATIONS	viii
Chapter 1. Introduction	1
1.1. Introduction	1
1.2. Basic concepts for research	2
1.2.1. Transition metal dichalcogenides (TMDs)	2
1.2.2. Line defects in 2D TMDs	4
1.3. Objective and outline of the dissertation	8
Chapter 2. Investigation of defects using modern transmission electron microscopy (TEM).....	10
2.1. Modern TEM	10
2.1.1. Aberration corrected TEM	10
2.1.2. Electron energy loss spectroscopy with enhanced energy resolution.....	12
2.2. <i>in situ</i> TEM	13
2.2.1. Temperature (cryo / heating holder)	13
2.2.2. Stress (mechanical holder)	15
2.3. Defect study using modern TEM	16
2.3.1. Stacking order and dislocation analysis using dark-field TEM	16
2.3.2. Identification of low angle GB using artificial moiré pattern	20
2.3.3. Electron beam irradiated defect generation	23
Chapter 3. Metallic anti-phase boundary of TMDs grown on the pristine graphene	24
3.1. APBs in TMDs	24
3.2. Experimental methods	25
3.3. Structural analysis of two types of APBs	27
3.3.1. Characterization of orientation and overall structure of APB in synthesized WS ₂	27
3.3.2. Atomic configurations of WS ₂ APBs	34
3.3.3. Structural stability of APB configurations	37
3.4. Electronic properties of X- and M-facing APBs	44
3.5. Conclusion and outlook	48
Chapter 4. AB/AC stacking boundaries of TMDs grown on the wrinkled graphene	50
4.1. AB/AC SBs in 2D materials	50
4.2. Experimental section	52

4.3. Structural analysis of AB/AC SBs.....	53
4.3.1. AB/AC SBs in WS ₂	53
4.3.2. Burgers vector analysis and atomic structure in AB/AC SBs in WS ₂	59
4.4. Formation of AB/AC SBs on wrinkled graphene template.....	66
4.5. Buckling of AB/AC SBs and their electronic property.....	72
4.6. Conclusion and outlook.....	77
Chapter 5. Edge rich multilayered TMDs grown on the nanocrystalline graphene.....	79
5.1. TMDs grown on the graphene defects	79
5.2. Experimental section.....	80
5.3. Growth behavior of WSe ₂ grown on the nanocrystalline graphene	81
5.4. Edge rich multilayered WSe ₂	84
5.5. Electronic property of WSe ₂ /ncG heterostructure	89
5.6. Conclusion and outlook.....	90
Chapter 6. Conclusion	91
Chapter 7. Perspective and outlook	93
REFERENCES.....	94

LIST OF FIGURES

[Chapter 1]

Figure 1.1. Various polytypes of single-layer and stacked TMDs.

Figure 1.2. Atomic structure of various GBs in 1H-MoS₂.

Figure 1.3. Atomic-scale edge configurations in monolayer MoS₂ at 800 °C.

Figure 1.4. Atomic structure of WSe₂/MoSe₂ in-plane heterostructure boundary.

[Chapter 2]

Figure 2.1. Multipole lenses.

Figure 2.2. Ray diagrams for TEM and STEM with image and probe aberration corrector, respectively.

Figure 2.3. ADF STEM images and EEL spectra of 4-fold (purple) and 3-fold (green) coordination of the Si atom in graphene matrix.

Figure 2.4. Phase transition of 1T-TaS₂ according to the temperature using *in situ* cryo / thermal TEM.

Figure 2.5. Torn graphene with AC and ZZ edges after *in situ* tensile testing.

Figure 2.6. AA' and AB(C) stacking structures of TMDs.

Figure 2.7. Various stacking geometries of WS₂ bilayers and calculated formation energies and interlayer spacing.

Figure 2.8. Bloch-wave simulation for various stacking configurations of WS₂.

Figure 2.9. Determination of Burgers vector using series of $\{\bar{2}110\}$ DF-TEM analysis.

Figure 2.10. Moiré pattern according to the rotation angle including low-angle GB.

Figure 2.11. Rotational moiré fringe spacing and difference in spacing across the GB.

Figure 2.12. Identification of GB by overlaying artificial layer.

[Chapter 3]

Figure 3.1. Epitaxial growth of WS₂ on graphene substrate.

Figure 3.2. Tungsten-terminated growth of WS₂.

Figure 3.3. High probability of APBs in WS₂ grown on the pristine graphene.

Figure 3.4. Anisotropic features of APBs in single-layer WS₂ according to the W-facing and S-facing.

Figure 3.5. APBs in MoS₂ grown on the sapphire substrate.

Figure 3.6. Atomic structures of two types of APBs.

Figure 3.7. Inclined APB segments compared to the S-ZZ direction.

Figure 3.8. Possible atomic configurations of APBs.

Figure 3.9. Experimental atomic configurations of W-facing APBs.

Figure 3.10. Relaxed atomic configurations of (a) W-44, (b) W-88, (c) S-44, and (d) S-88 APBs.

Figure 3.11. Edge formation energy calculation of WS₂.

Figure 3.12. Atomic models for the formation energy calculation of APBs.

Figure 3.13. APB formation energy of S-facing and W-facing APBs as a function of chemical potential of sulfur.

Figure 3.14. Coordination numbers of S and W atoms consisting of W-S-W, S_{rhomb}, S-W-S, and W_{rhomb} configurations.

Figure 3.15. Energy diagrams of structural transition between (a) W-facing and (b) S-facing APBs.

Figure 3.16. Distribution of S_{rhomb} and W-S-W units in W-facing and S-facing APBs.

Figure 3.17. No migration of APBs under additional heat source.

Figure 3.18. Optimized structures of S_{rhomb} APB and energy profiles of initial state (*IS*), transition state (*TS*), intermediate state (*IM*), and final state (*FS*) for migrating S_{rhomb} APB in WS₂ ZZ nanoribbon.

Figure 3.19. Local variation of electronic properties at APBs.

Figure 3.20. MoS₂ FET devices for investigating effect of facet in TMDs' APBs.

Figure 3.21. The effects of APBs on electron transport properties.

Figure 3.22. Two types of edge in degraded MoS₂.

[Chapter 4]

Figure 4.1. AB and AC stacking geometries in bilayer WS₂ grown on large grain and wrinkled graphene.

Figure 4.2. Experimental and simulated AR-STEM images of various stacking configurations in WS₂ bilayer.

Figure 4.3. DF-TEM images obtained by adjacent diffraction spots, indicating stacking orders.

Figure 4.4. Experimental DF-TEM image series by specimen tilting.

Figure 4.5. Energy profile along an AC direction for bilayer WS₂ with (a) $\theta = 0^\circ$ and (b) $\theta = 60^\circ$.

Figure 4.6. Analysis of Burgers vector using DF-TEM and corresponding atomic resolution images.

Figure 4.7. AR-TEM images of AB/AC SBs in bilayer WS₂.

Figure 4.8. Moiré-like phenomena of AB/AC SBs.

Figure 4.9. The relationship between SB orientation and Burgers vector direction.

Figure 4.10. Topological defects inside AA' stacking orders in WS₂.

Figure 4.11. Strain-mediated AB/AC SB defect.

Figure 4.12. Graphene wrinkles act as vertical barriers to WS₂ epilayer.

Figure 4.13. Distribution of SBs in WS₂/wrinkle rich graphene heterostructure.

Figure 4.14. Density of SBs in epitaxially grown WS₂ grown on (a) flat graphene and (b) wrinkled graphene.

Figure 4.15. Different density of AB/AC SBs from the anisotropic friction of graphene wrinkles.

Figure 4.16. Out-of-plane buckled structures of WS₂ SBs.

Figure 4.17. EEL spectra analysis for investigating electronic property of AB/AC SBs in bilayer WS₂.

Figure 4.18. Effect of in-plane strain on the electronic properties using DFT calculation.

Figure 4.19. Dislocation node, which is intersection of two AB/AC SBs.

[Chapter 5]

Figure 5.1. The growth behavior of WSe₂ grown on the SiO₂/Si and ncG.

Figure 5.2. Raman analysis of WSe₂/ncG heterostructure.

Figure 5.3. AFM height and phase images of WSe₂/ncG heterostructure using tapping mode.

Figure 5.4. Edge rich multilayered WSe₂ cluster grown on the ncG template.

Figure 5.5. Orientation relationship between WSe₂ domain and ncG film with high spatial resolution.

Figure 5.6. Atomic-scale edge configuration of *n*-WSe₂.

Figure 5.7. UPS spectra of WSe₂ on SiO₂ (blue), ncG (red) and *n*-WSe₂ (black) using He I source ($h\nu$ = 21.2 eV) and measured WF.

LIST OF TABLES

Table 3.1. Summarized transport properties of *s*-MoS₂, *m*-MoS₂, and *p*-MoS₂ devices.

Table 4.1. The relative energies of SBs without and with buckling.

Table 5.1. Lattice spacing of ncG before and after WSe₂ growth.

LIST OF ABBREVIATIONS

1D	one-dimensional
2D	two-dimensional
ADF	annular dark-field
AFM	atomic force microscopy
APB	anti-phase boundary
AR-TEM	atomic resolution transmission electron microscopy
AR-STEM	atomic resolution scanning transmission electron microscopy
BF-TEM	bright-field transmission electron microscopy
BSE	backscattered electron
C-AFM	conductive atomic force microscopy
CVD	chemical vapor deposition
DFT	density functional theory
DF-TEM	dark-field transmission electron microscopy
EELS	electron energy loss spectroscopy
FET	field effect transistor
FFT	fast Fourier transform
GB	grain boundary
HAADF	high-angle annular dark-field
MEMS	microelectromechanical systems
NBD	nanobeam diffraction
ncG	nanocrystalline graphene
SAED	selected area electron diffraction
SB	stacking boundary
SE	secondary electron
SEM	scanning electron microscopy
STEM	scanning transmission electron microscopy
TEM	transmission electron microscopy
TMD	transition metal dichalcogenide
UPS	ultraviolet photoelectron spectroscopy
vdW	van der Waals
WF	work function

Chapter 1. Introduction

1.1. Introduction

Chemical vapor deposition (CVD) method is one of the most famous approaches for the scalable production of various two-dimensional (2D) materials with high-crystallinity¹⁻⁵. It is well known that various parameters (*e.g.* precursors, growth temperature, pressure, substrates, *etc.*) greatly influence the nucleation and growth behavior of 2D materials using the CVD method. While catalytic metal substrates (*e.g.* Cu, Ni) are used for graphene growth, catalytic-free inert substrates (*e.g.* SiO₂, sapphire) are introduced for the growth of transition metal dichalcogenides (TMDs)⁶, suggesting that the structural features of the substrate are largely responsible for the nucleation and growth of 2D TMDs; in other words, surface morphology, grain size, orientation, and surface defects have a crucial effect on the growth behavior of 2D TMDs. For example, MoS₂ films are preferentially nucleated at the surface step edge from the catalytic effect of steps⁷. In addition, the large size of single-crystal MoS₂ flakes are mainly grown on Au(100) and Au(110) facets than on the Au(111) facet at a relatively high temperature (> 680 °C) due to the facet-dependent binding energy between MoS₂ and Au substrate⁸.

Atomically thin 2D TMDs could be combined with other 2D material templates to form van der Waals (vdW) heterostructures. Various vdW heterostructures have been extensively researched due to their novel properties beyond the properties of individual 2D materials. For example, for MoS₂/WSe₂ p-n heterostructures, photo-excited free electrons and holes reside in each layer due to their strong charge transfer efficiency⁹. There are two representative methods to fabricate vertical heterostructures: 1) The multiple transfer method^{9,10} and 2) direct synthesis on other 2D materials using the CVD method^{5,11}. The latter makes dramatically released lattice matching conditions due to the vdW interaction between the inactive surface of the template and deposited materials. A weak vdW interaction enables the fabrication of many kinds of vdW heterostructures including metal, semiconductor, and insulating materials. However, the introduction of active sites in a 2D material template (*e.g.* grain boundaries (GBs), wrinkles, ripples, contaminations, intrinsic defects) have a profound effect on the nucleation and growth behavior of TMDs from the strong interlayer interaction beyond the weak vdW interaction. For example, multilayer WSe₂ flakes and some particulates are formed along the line defects of graphene substrate, indicating that line defects have high reactivity¹². In addition, various structural features in the substrate can significantly affect the intrinsic heterostructure properties inducing primary bonding between layers¹³.

1.2. Basic concepts for research

1.2.1. Transition metal dichalcogenides (TMDs)

Following graphene, 2D TMDs with intrinsic band gaps have drawn extensive attention due to their excellent intrinsic properties and potential for a wide range of applications. For example, compared to the thin film of conventional bulk materials, clean 2D TMDs with a reduced surface roughness effect have robust electrical properties with high mobility of $65 \text{ cm}^2 \text{ V}^{-1} \text{ s}^{-1}$ in sub-2 nm thick films and with high on/off ratios of $\sim 10^7$ at room temperature¹⁴⁻¹⁶. Despite the superior inherent properties of 2D TMD-based devices with respect to scaling, contact resistance between 2D TMDs and conventional electrode metals are a significant limitation for further progress^{17,18}. However, recently, M. Tosun *et al.* reported that the generation of an anion vacancy defect *via* a mild plasma treatment in WSe₂ is an effective approach to reduce contact resistance and improve the electrical performance¹⁹. Likewise, proper defect engineering in 2D TMDs could provide opportunities for overcoming the barriers of commercialization and industrialization of 2D devices.

As all defects in 2D TMDs are placed on the surface, defects (*e.g.* vacancy, dopants, and GB), which cause localized heterogeneities, strongly induce novel properties beyond intrinsic ones; these include deterioration (*e.g.* mobility degradation from electron scattering²⁰) and charge redistribution-based novel properties. For example, Mn-doped MoS₂ induce antiferromagnetic coupling with the neighboring S atoms due to the *d-p* orbital hybridization in the nonmagnetic MoS₂ matrix^{21,22}. In this way, joint theoretical and experimental studies for defects on 2D materials have been continuously reported, but they are rather fragmentary. Therefore, the systematic study for profound structural understanding and the connection between defect-mediated lattice irregularity and corresponding properties should be required to further achieve programmable 2D materials.

Herein, among various phases and types of TMDs, semiconducting group 6 TMDs are the main focus, and are denoted as MX₂ (M = Mo, W and X = S, Se). One layer of MX₂ is composed of three atomic layers including two adjacent layers of X atoms covalently bonded by an M layer forming an X-M-X configuration. They have various polytypes according to the relative position of the top and bottom chalcogen atoms^{23,24} (Figure 1.1). Its most common phase is the semiconducting trigonal prismatic phase (noted as 1H phase for a single layer MX₂, Figure 1.1a), which has vertically aligned X layers. The other is the metallic octahedral prismatic phase (noted as 1T phase, Figure 1.1b), which is formed by gliding one X layer. While the 1T phase of MoS₂ was experimentally observed *via* carrier doping²⁵, it is known as a metastable phase due to its intrinsic dynamical instability. Therefore, the 1T phase spontaneously transforms into a distorted 1T phase (denoted as 1T' phase), exhibiting Peierls-like distortions mediated by electron-phonon interactions²⁴. Figure 1.1c shows a (2×1) superstructure²⁶, similar to the *T_d*-W(Mo)Te₂ structure²⁷. In addition, the (2×2) superstructure²⁶ in the *x-y* plane is another typical feature of a distorted structure, similar to group 7 TMDs (*e.g.* rhenium disulfide²⁸). When two

layers of the 1H phase are stacked by van der Waals (vdW) forces, two representative stable stacking configurations appear, namely, the 2H phase (*i.e.* two 1H layers; AbA | BaB) and 3R phase (*i.e.* three 1H layers representing the rhombohedral phase; AbA | CaC | BcB).

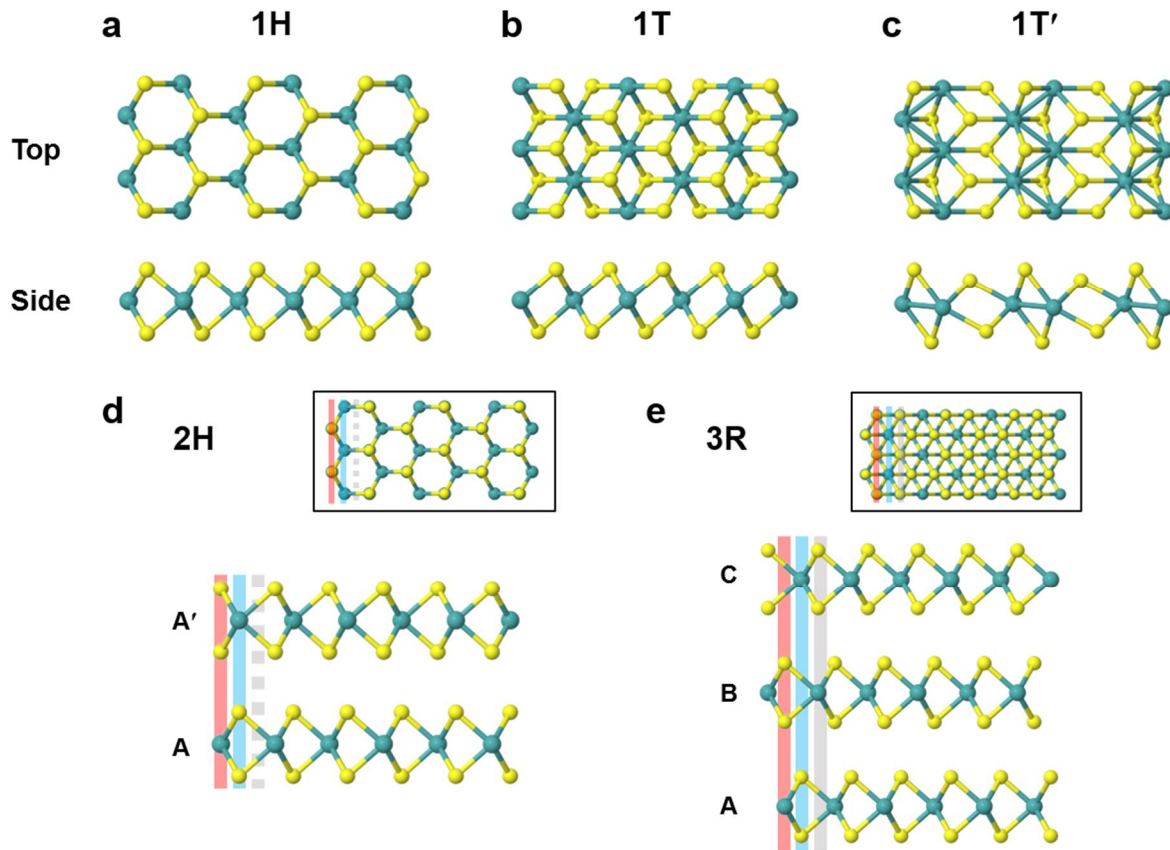


Figure 1.1. Various polytypes of single-layer and stacked TMDs. (a) 1H phase, (b) 1T phase, (c) distorted (2×1) 1T phase (denoted as 1T'), (d) 2H phase, and (e) 3R phase. A' means inverted orientation of TMDs and B(C) means lateral translation relative to another, maintaining initial orientation (called as Bernal stacking).

1.2.2. Line defects in 2D TMDs

Line defects are irregularities in the ideal arrangement of entire rows of lattice points. For example, the agglomeration of chalcogen vacancies in TMDs results in chalcogen line vacancies, which could tune the electronic properties by combining with other filling materials²⁹. These generally form along the zigzag (ZZ) direction, which has lower formation energy²⁹. In addition, as mentioned before (Chapter 1.2.1), various phases of TMDs result in a phase boundary (*i.e.* 1T/2H phase boundary). Recently, the 1T phase transition^{25,30} (*i.e.* metallic phase) from the 1H phase (*i.e.* the semiconducting phase) of TMDs has been extensively researched to expand its commercial use. It accompanies the line defects between the 1H and 1T phases, denominated the phase boundary, acting as a new pathway for strong charge transfer³¹. Likewise, intrinsic and extrinsic line defects greatly modulate the properties of 2D TMDs. CVD-based synthesized polycrystalline TMDs have many line defects, such as inevitable GBs and edges. In addition, advanced CVD methods enable us to fabricate in-plane heterostructure for tuning electronic and optical properties^{5,32,33}, resulting in the formation of in-plane heterostructure boundaries.

Grain boundary | Large-scale polycrystalline 2D TMD films inevitably have GBs between adjacent grains of different orientations. Like other 2D materials, GBs in 2D TMDs could be classified as either a tilt boundary (TB) or an anti-phase boundary (APB). APBs are a special boundary where inverted grains (rotated 60° for hexagonal lattice) are encountered; resulting in greatly distinguished electrical and optical properties. For example, TBs decrease the conductivity and cause a strong photoluminescence enhancement, while APBs slightly enhance in-plane electrical conductivity and strongly quench photoluminescence³⁴, because of the different defect configurations between the two cases. In detail, TBs are composed of dislocation cores^{35,36} (*e.g.* 5|7, 6|8 rings), inducing the localized states that could be dominant electron scattering centers (Figure 1.2a). Inter-domain electron mobilities depend on the misorientation angle, which is closely related to dislocation core density, and tend to be significantly degraded compared to intra-domain devices³⁷. On the other hand, APBs are composed of 4- and 8-membered rings, resulting in a metallic property from the dispersive bands crossing the Fermi level³⁴. W. Zhou *et al.* reported that the two types of APBs³⁵, namely, (1) point-shared at a normal S2 site (4|4P, Figure 1.2b) and (2) edge-shared (4|4E, Figure 1.2c) APBs, act as metallic quantum wires embedded in semiconducting a MoS₂ matrix (as shown in Figure 1.2e). Figure 1.2d shows the kinks of 4|4P APBs with 8-membered configurations, connecting separated 4|4P segments^{34,35,38}. It is well known that GBs are linked by various GB kinks instead of straight features, which could strongly influence the properties of materials. According to the band structure and local density of states (LDOS) for 4|8 (4|4P with extremely high density of kinks) as shown in Figure 1.2e, kinks significantly affect electronic

properties by introducing localized midgap states³⁵, while 4|4P and 4|4E APBs have delocalized states in one dimension.

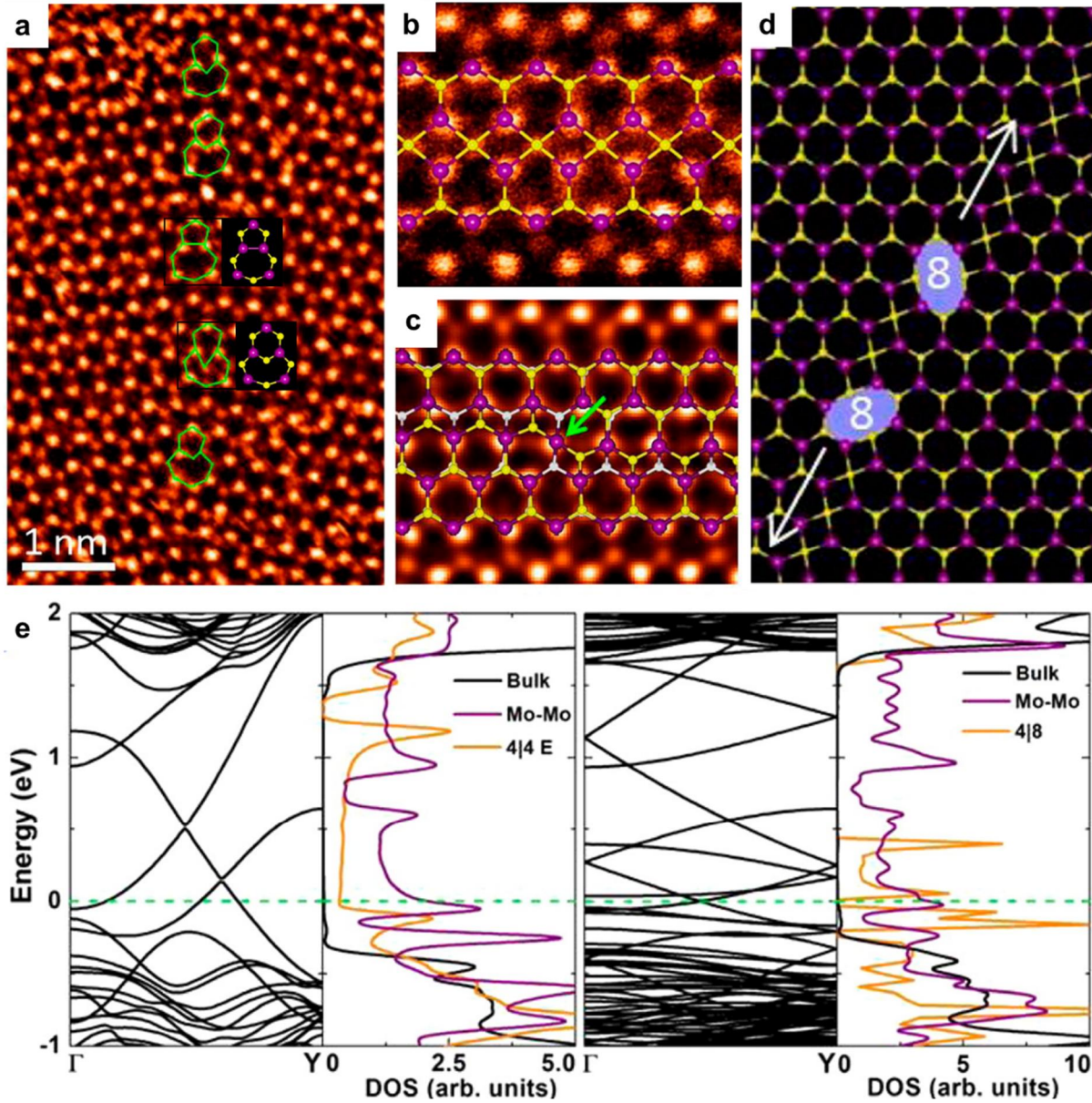


Figure 1.2. Atomic structure of various GBs in 1H-MoS₂. (a) Annular dark-field (ADF) images of an 18.5° TB including 5|7 and 6|8 dislocations. (b,c) ADF images of two types of APBs with overlaid atomic model, (b) 4|4P and (c) 4|4E type of APB. APB steps are linked by four-fold coordinated Mo atom, denoted as green arrow. (d) Schematic structure of the APB and APB kinks denoted as “8”. (e) Band structure (left) and LDOS (right) of 4|4E and 4|4P APB with highest kink density.

(a-e) Reprinted from W. Zhou *et al.* (2013) (Nano Lett. 13, 2615-2622) with original copyright holder's permission. Copyright 2013 American Chemical Society.

Edge | Edges, one of the most prominent line defects, show novel electronic and magnetic properties, especially for nanoribbon with sub-nm width. Single crystal synthetic TMDs that predominantly adopt hexagonal or triangular shapes by Wulff construction have a low energy edge state^{39,40}. For 2D TMDs, the ZZ edge is theoretically more stable than the armchair (AC) edge over the entire range of chemical potential of chalcogen (μ_X), therefore, ZZ edges are more frequently observed. Accordingly, recent work showed that the crack propagation^{41,42} in monolayer MoS₂, another one-dimensional (1D) defect in 2D materials, is along the ZZ direction maintaining both Mo and S terminations on either side. Different electronic and magnetic properties appear according to the edge structure, which has the function of μ_X . For example, the Mo-ZZ edge with an unsaturated Mo atom, has the highest magnetism with a total magnetic moment of $3.33 \mu_B/\text{nm}$ ³⁹. Recently, edge engineering at high temperatures using *in situ* TEM has been reported. Ultralong flat ZZ edges without any atomic corrugations were created at 800 °C in monolayer MoS₂⁴³. Figure 1.3 shows detailed configurations of two types of atomically flat ZZ edges, displaying bare Mo edge (Figure 1.3a) and Mo-replaced S edge (Figure 1.3b), which could be potential for spin logic applications⁴³. In addition, nanowire-terminated ZZ edges are created at 500 °C in monolayer MoS₂ and Mo_xW_{1-x}Se₂, generating novel heterostructures (*e.g.* semiconducting 2D matrix terminated metallic 1D nanowires)^{44,45}.

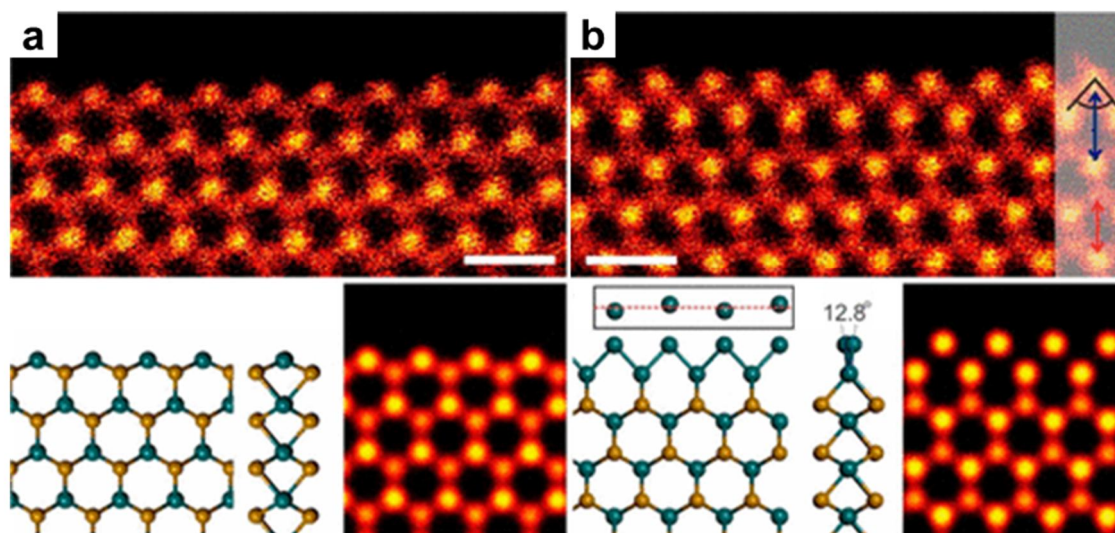


Figure 1.3. Atomic scale edge configurations in monolayer MoS₂ at 800 °C. ADF-STEM images of (a) a bare Mo edge and (b) Mo-replaced S edge, respectively. Bottom panels show top and side view of the DFT-calculated atomic models and simulated STEM images.

(a-b) Reprinted from Q. Chen *et al.* (2017) (Nano Lett. 17, 5502-5507) with original copyright holder's permission. Copyright 2017 American Chemical Society.

In-plane heterostructure boundary | In-plane heterostructure has huge potential for application in high-performance and flexible electro-optical devices by combining various building blocks. In-plane heterostructures have been synthesized *via* single-step^{5,32}, two-step⁴⁶ or multi-step⁴⁷ growth processes, showing a sharp coherent boundary between distinct TMDs. Such coherent superlattices enables us to have targeted functionalities at one atomic thickness by edge-epitaxy-mediated straintronics⁴⁸. Recently, P. K. Sahoo *et al.* reported the one-pot synthesis of lateral heterostructure by switching the carrier gas^{32,33}. Interestingly, the WSe₂ to MoSe₂ interface (Figure 1.3e) has an abruptly sharp boundary, while the MoSe₂ to WSe₂ transition (Figure 1.3d) exhibits some degree of alloy formation with a smooth interface, due to the difference in reducing and oxidation rate between W and Mo compounds³².

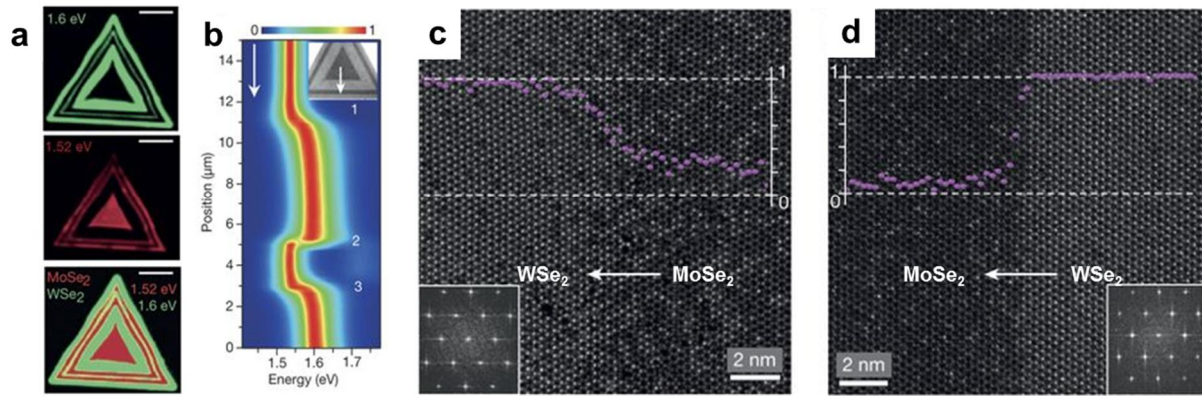


Figure 1.4. Atomic structure of WSe₂/MoSe₂ in-plane heterostructure boundary. (a) Photoluminescence intensity maps for WSe₂ (1.6 eV) and MoSe₂ (1.52 eV). (b) Contour color plots of the normalized photoluminescence intensity of three-junction heterostructures along the arrows in insets. (c,d) High angle ADF images of the (c) smooth (MoSe₂ to WSe₂) and (d) sharp (WSe₂ to MoSe₂) boundary. Insets are corresponding Fourier-transform patterns and composition profiles.

(a-d) Reprinted from P. K. Sahoo *et al.* (2018) (Nature 553, 63-67) with original copyright holder's permission. Copyright 2018 Springer Nature.

1.3. Objective and outline of the dissertation

Atomically isolated thin 2D materials can also be reassembled with other 2D materials in a layer-by-layer precision, forming vdW heterostructures¹⁰. Over the years, these vdW heterostructures have been extensively studied due to the unusual properties and novel physical phenomena, originated from the electron-phonon/electron interaction between adjacent layers. Their properties can be manipulated by adjusting various combinations of their components. The sequential transfer (*e.g.* dry⁴⁹ and wet⁵⁰ transfer) of exfoliated samples for the production of stacked heterostructures is a well-known method, but is time-consuming and is limited by contaminated interfaces. Therefore, CVD-based heterostructure fabrication has been developed capable of mass production. It allows for clean and atomically sharp interfaces, but also the ability to control the stacking configurations *via* vdW epitaxy.

The importance of the interface in a vdW heterostructure has been strongly emphasized because its interlayer coupling affects the electrical and optical properties of heterostructures. When defects (*e.g.* GBs, wrinkles, vacancies) are introduced in the template layer, they are more reactive with high chemical potential than the pristine regions, thus accelerating nucleation and the multilayer growth of heterostructures¹². However, the effects of lattice imperfection in a template layer on the structural configuration and properties of a vdW heterostructure have not been systematically investigated. In this thesis, I have studied the novel defects in TMDs mediated by various features of a graphene template (*i.e.* pristine, wrinkled, and lattice defective) to obtain a profound understanding of the effect of the interface on the heterostructure configuration and its corresponding properties.

Firstly, in Chapter 3, anisotropic structural features of APBs will be discussed using W(Mo)S₂ and a pristine graphene heterostructure. TMDs directly synthesized on the graphene have a confined orientation aligned with graphene *via* vdW epitaxial growth, resulting in the high distribution of APBs rather than TBs. The anisotropic features of APBs (*i.e.* straight and saw-toothed APBs) were discovered according to the transition-metal-facing and chalcogen-facing APBs. Combined experimental and computational results indicate that, despite their anisotropic features, all APBs have a predominantly chalcogen-facing dense structure to retain the most stable atomic configuration, followed by some kinks for connecting adjacent facets. Devices including saw-toothed APB have considerably lower electron mobilities than that of straight APB, indicating that the kinks act as intrinsic scattering centers.

Secondly, in Chapter 4, the formation of AB/AC stacking boundaries (SBs) in bilayer WS₂ will be reported using WS₂ directly grown on large grain and wrinkle-rich graphene as a template. Graphene wrinkles act not only as nucleation sites for multilayer growth but also induce additional friction and leading to Shockley partial dislocation driven AB/AC SBs in the TMD epilayer. AB/AC SBs in TMD have a buckled structure with 1 nm of vertical height to release in-plane strain and behave like monolayer TMD due to reduced interlayer coupling. These results clarify significant substrate morphology effects even in vdW heterostructures.

Finally, in Chapter 5, the crystallinity effect of the graphene template on the growth behavior of WSe₂ is mentioned using nanocrystalline graphene (ncG) as a template, which includes many active sites for multilayer growth. Highly defective ncG facilitates the high density of nucleation sites and multilayer growth and results in edge-rich multilayer WSe₂ flakes. In addition, such a heterostructure shows strong charge transport at the interface due to the formation of primary bonding between ncG substrate and the TMD layers beyond the vdW bonding. Moreover, this heterostructure shows a strong pinning effect, compared to the weak pinning effect of the pristine graphene and TMD heterostructure.

Chapter 2. Investigation of defects using modern transmission electron microscopy (TEM)

2.1. Modern TEM

Atomic scale characterization (*e.g.* bonding, composition, atomic configuration) of all atoms in a specimen has been a long-standing goal of electron microscopy. In addition, following the successful isolation of pristine 2D materials⁵¹, the demand for atomic resolution at low voltage has been intensified for minimizing knock-on damage (less than 90 kV) on the specimen⁵². However, spherical and chromatic aberration are fundamental limitations for improving the information limit in high-resolution TEM⁵³. In the last few decades, the atomic resolution characterization has been enabled with the introduction of aberration corrector^{53,54}, even at low voltage (*e.g.* 30 kV⁵⁵, 60 kV⁵⁶, 80 kV^{57,58}). The capability of modern TEM include 1) aberration correction (spherical and chromatic) for superior resolution far below 1 Å, 2) energy-filtered imaging (EFTEM), X-ray energy dispersive spectroscopy (EDS) and electron energy loss spectroscopy (EELS) for microchemical analysis, 3) convergent beam diffraction (CBED) and annular dark-field imaging (ADF) for microstructure analysis with probe beam.

2.1.1. Aberration corrected TEM

Basically, the resolution limit in TEM is determined by the quality of objective lens, associated with the spherical aberration (C_s), and the wavelength of electrons (λ), related to the accelerating voltage of TEM, and is followed by the given formula⁵⁹, $\sim C_s^{1/4} \lambda^{3/4}$. High-voltage TEM could obtain better resolution by reducing λ ⁶⁰, but it is an expensive and specimen-destructive method (*e.g.* knock-on damage⁶¹, radiolysis⁶², electron-stimulated desorption⁶³). The other strategy improving microscope performance is reducing or eliminating C_s by producing negative C_s . For conventional TEM with symmetric lens design, positive aberrations are unavoidable⁵⁹. Since the breakthrough of non-round multipole lenses⁶⁴ (Figure 2.1), they cancel the positive C_s by generating negative C_s . There are two basic approaches of corrector, 1) octupole/quadrupole assembly⁶⁵, and 2) hexapole assembly^{66,67}. Double-hexapole system has been applied successfully in conventional TEM and scanning TEM (STEM) system with various advantages. The TEM correctors lies below the objective lens and the STEM corrector above⁵⁹ (Figure 2.2). Spherical aberration corrected TEM at 60 kV primary voltage allows imaging of individual atoms and atomic defects in nanomaterials, including light-element atoms⁶⁸ (*e.g.* C, B, and N). The chromatic aberration (C_c), which arise from the electron-energy dependent refraction properties, is another principal aberration, has a notable effect at low accelerating voltages⁵⁹. The C_c could be almost zero by introducing a monochromator, which disperse the incident beam and select a narrow energy range by inserting small slit⁶⁹.

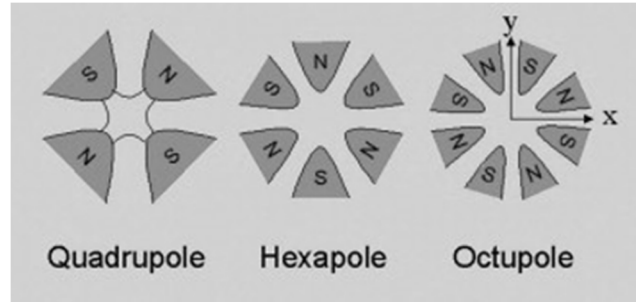


Figure 2.1. Multipole lenses. Electron travel path is into the page. This figure⁶⁴ is reprinted from A. Bleloch and A. Lupini (2004) (Materials Today 7, 42-48) with original copyright holder's permission. Copyright 2004 Elsevier Ltd.

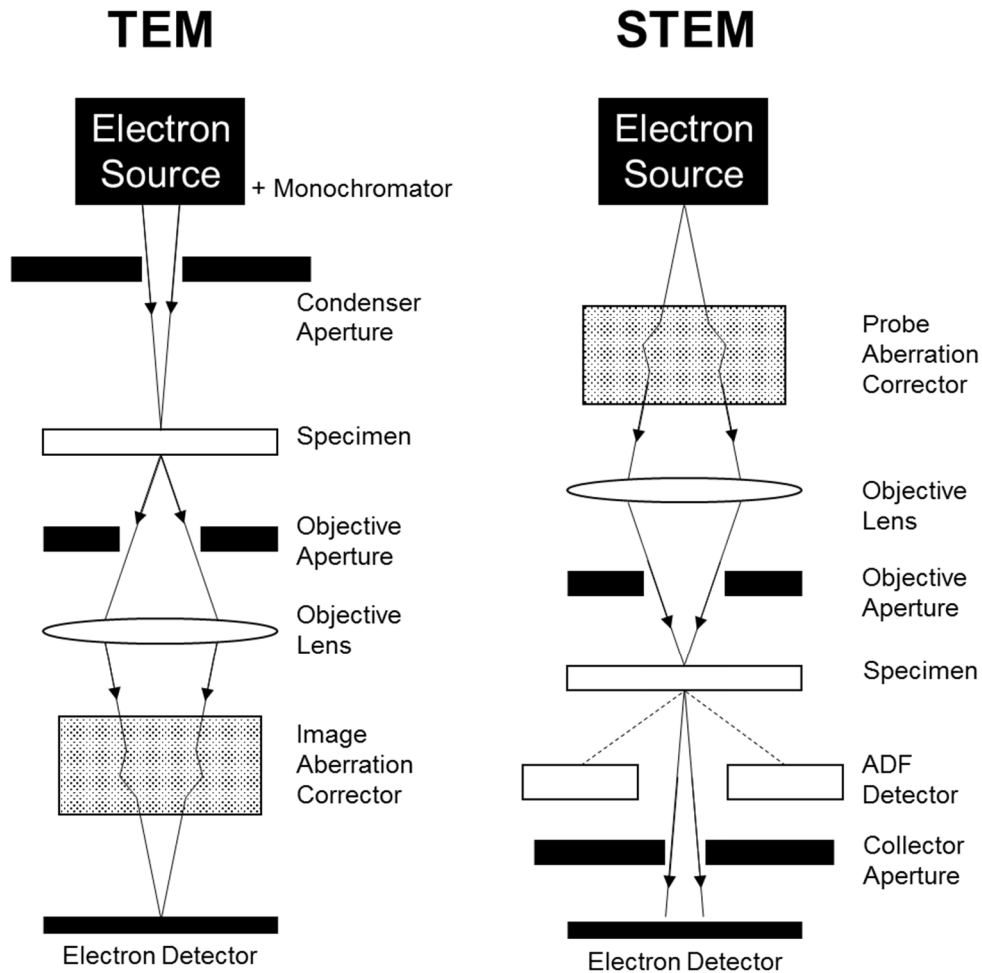


Figure 2.2. Ray diagrams for TEM and STEM with image and probe aberration corrector, respectively.

2.1.2. Electron energy loss spectroscopy with enhanced energy resolution

EELS based on the inelastic scattering of high energy electrons in TEM allows to obtain the chemical information beyond the atomic configuration. EELS data could be distinguished into two regions, 1) low-loss region, dominated by valence electron excitation, and 2) high-loss region by inner shell electron excitation. Low-loss EELS, called as valence EELS, offers local electronic and optical information (*e.g.* plasmon excitation⁷⁰⁻⁷², bandgap^{73,74}), while high-loss EELS, called as core-loss EELS, produces the chemical composition and local structure information (*e.g.* atomic coordination, local crystal field)⁷⁵. The introduction of aberration corrected TEM allows the atomic precision analysis and atomic scale mapping of chemical and electronic structure using spatially-resolved EELS^{54,76}. For example, different types of single Si atom dopant configuration in graphene matrix show different Si $L_{2,3}$ EELS edges as shown in Figure 2.3⁷⁷. A combination of atomic-scale STEM, EELS and *ab initio* calculations confirms the exact defect geometries.

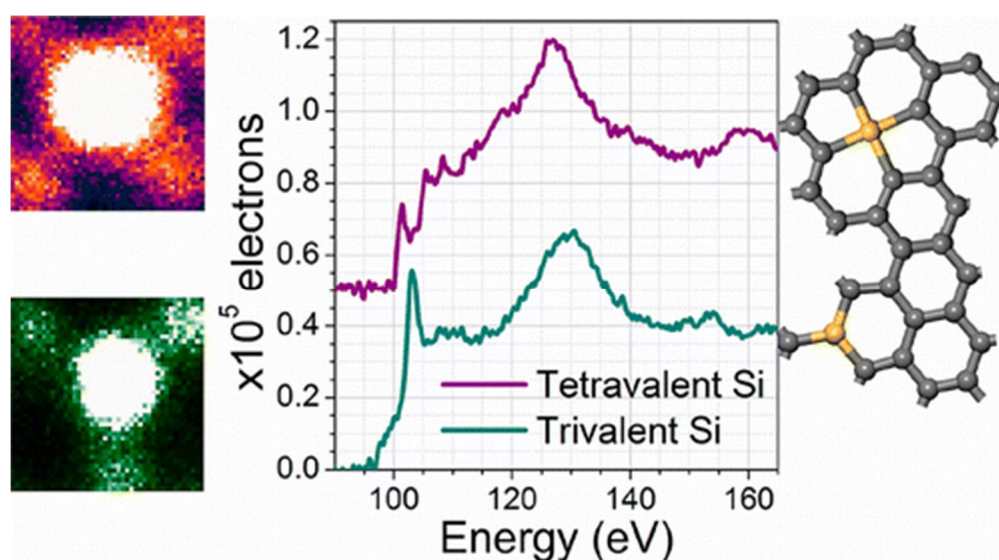


Figure 2.3. ADF STEM images and EEL spectra of 4-fold (purple) and 3-fold (green) coordination of the Si atom in graphene matrix. This figure⁷⁷ is reprinted from Q. M. Ramasse *et al.* (2013) (Nano Lett. 13, 4989-4995) with original copyright holder's permission. Copyright 2012 American Chemical Society.

2.2. *in situ* TEM

Modern TEMs produce extraordinary sub-angstrom spatially resolved structural and electronic information of materials, but they are performed under high vacuum pressure and static sample environments. To overcome these limitations of TEM, various *in situ* holders have been developed along with the improvement of microelectromechanical systems (MEMS) technologies⁷⁸. *In situ* TEM techniques are attractive in that the observation of dynamic process of interaction between materials and applied external stimulus (e.g. mechanical, thermal/cryogenic, electrical and liquid/gas environment) with ultrahigh spatial, time, and energy resolution in real time.

2.2.1. Temperature (cryo / heating holder)

Temperature is one of key parameter in the thermodynamics and kinetics in materials science. Therefore, *in situ* thermal TEM equipped with MEMS-based heating holder is commonly used to study the phase transition⁷⁹, novel edge engineering⁴⁴, and *in situ* synthesis of 2D materials^{80,81}. *In situ* cryo TEM can be reached at -185 °C using liquid nitrogen and is commonly used for observing phase transitions at low temperature⁸² and reducing electron beam damage. Charge density wave (CDW) is physical phenomenon especially exhibiting at low temperature and the superlattice is very sensitive to the temperature, because it occurs when half-filled electrons interact each other to reduce energy⁸³. As shown in Figure 2.4a-d, superlattice diffraction peaks are transformed according to the temperature (denoted as red triangle for Bragg peak and others for CDW-related peak) from commensurate CDW at 88 K to incommensurate CDW (298K, 363 K). When the temperature is reached over 1200 K, thick 1T-TaS₂ flake is etched by forming triangular pits and atomically sharp ZZ edge as shown in Figure 2.4e. In addition, diffraction pattern shown in inset of Figure 2.4e shows ring pattern of superlattice by the external heat source.

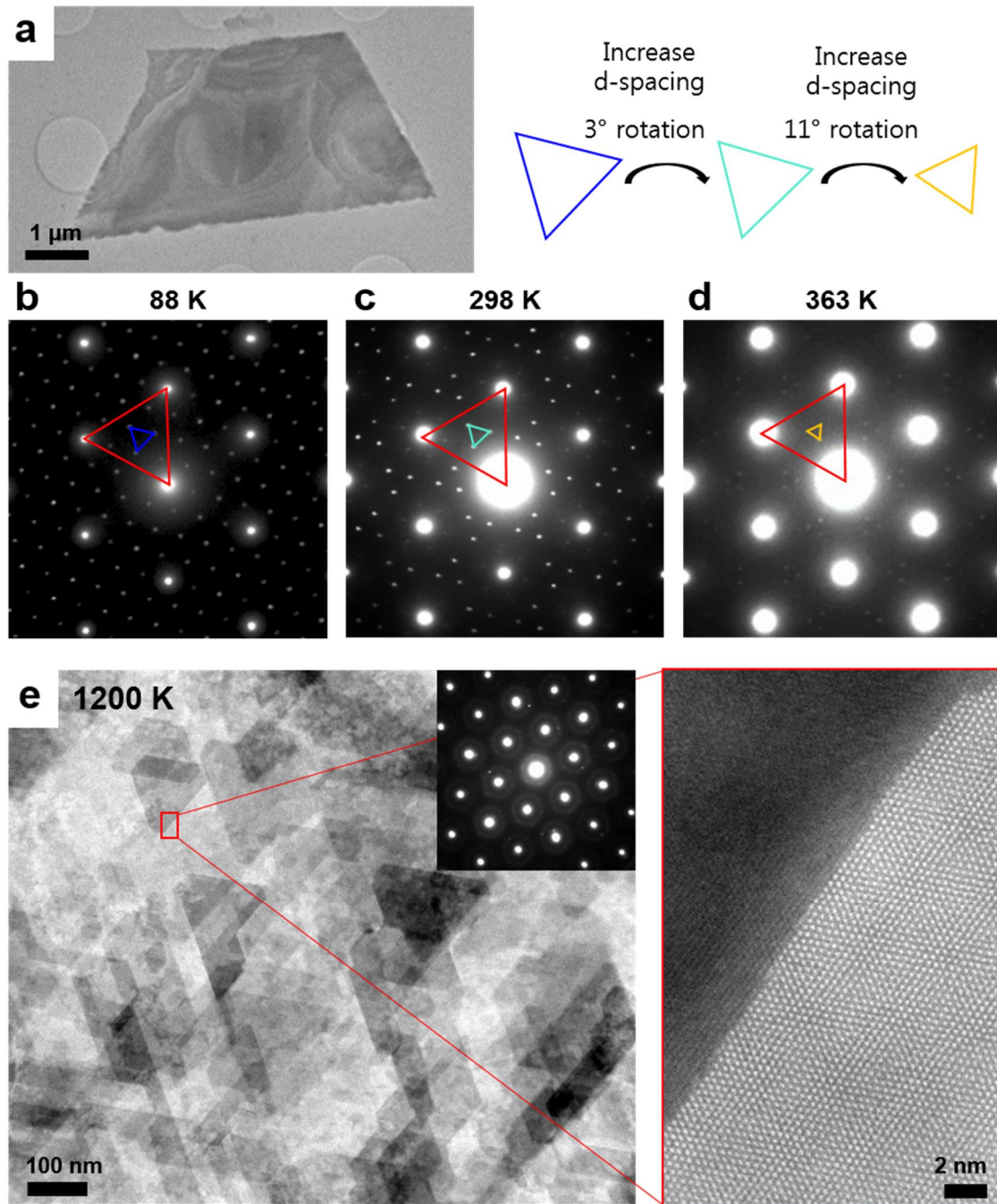


Figure 2.4. Phase transition of 1T-TaS₂ according to the temperature using *in situ* cryo / thermal TEM. (a-d) Superlattice diffraction peak transition of 1T-TaS₂ according to the temperature using *in situ* cryo holder with liquid nitrogen. (e) Thermal etching phenomena at 1200 K using MEMS-based *in situ* heating holder.

2.2.2. Stress (mechanical holder)

An *in situ* tensile testing platform using push-to-pull (PTP) MEMS device has been developed and it allows to understand the relationship between atomic-scale structural characterization and mechanical properties with uniform uniaxial loading of a freestanding 2D materials in TEM⁸⁴. It reveals brittle fracture of various 2D materials (*e.g.* graphene, MoS₂) with crack propagation along the ZZ and AC direction, which are theoretically stable edges. Figure 2.5 shows that the torn graphene after *in situ* tensile testing, and it represents that the crack is propagated along the AC and ZZ direction of graphene by comparing diffraction pattern (inset) to torn edge. In the meantime, stress–strain plot and fracture strength could be measured using *in situ* tensile testing. With the electromechanical testing holder equipped with electrical PTP MEMS device, the simultaneous *in situ* mechanical and electrical measurements could be enabled, which is advantageous for piezoelectric materials⁸⁵.

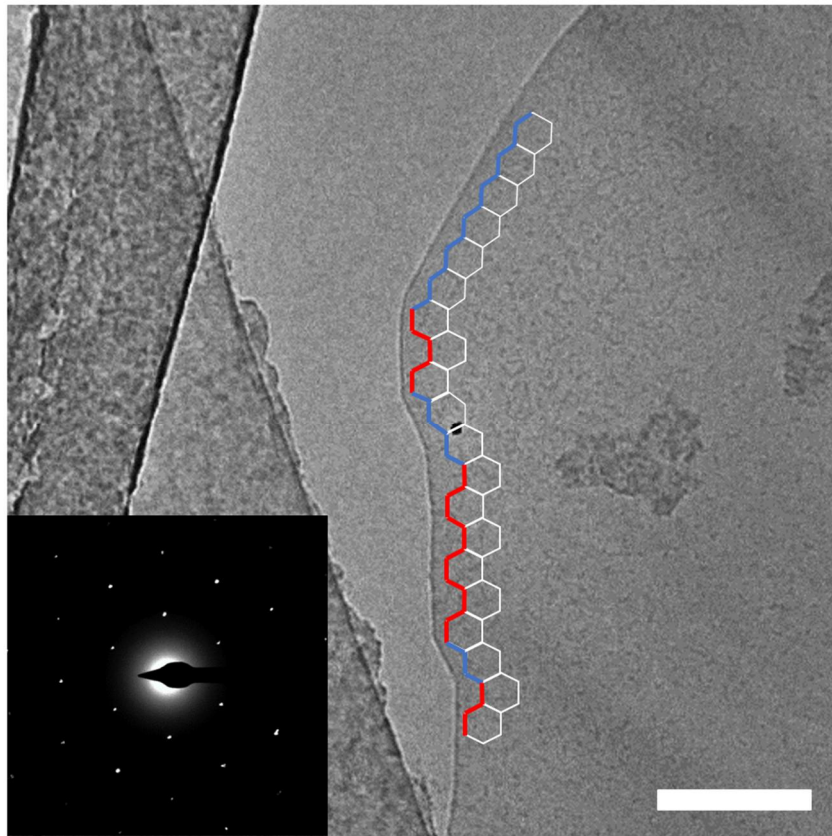


Figure 2.5. Torn graphene with AC and ZZ edges after *in situ* tensile testing. Inset is diffraction pattern, indicating the orientation of graphene. Scale bar, 200 nm. This figure⁸⁴ is reprinted from K. Kim *et al.* (2019) (Appl. Microsc. 49: 3) with original copyright holder's permission. Copyright 2019 Springer Singapore.

2.3. Defect study using modern TEM

TEM has strong capability not only to probe atomic-scale defect configurations and their electronic structures, but also to deliberately manipulate them using high energy electron beam and to investigate their dynamics by applying external stimulus.

2.3.1. Stacking order and dislocation analysis using dark-field TEM

For bi- or multi-layer 2D materials, dark-field TEM (DF-TEM) images are useful for estimating stacking order (obtained using 1st-order diffraction spots, $\Phi 1$) and layer number^{86,87} (obtained using 2nd-order diffraction spots, $\Phi 2$). The reason is that their intensities depend on the interference of electron waves diffracted from the specific lattice periodicity of the specimen, where the relative phase θ between two diffracted electron waves is determined by the lateral shift (Δx) of the lattice lines in top and bottom layer⁸⁶. For example, for 2H (AA') stacking (Figure 1.1d), electron waves from each layer interfere constructively for $\Phi 1$ and $\Phi 2$, because all lattice lines both bottom and top layers are vertically aligned without lateral translation, resulting in increased intensity of DF-TEM from with increased layer number. On the other hands, for 3R (AB/AC) stacking, called as Bernal stacking, one layer is laterally translated by $\Delta x = 2/3a_1$ (a_1 is lattice periodicity corresponding to $\Phi 1$) relative to another, resulting in phase shift. For $\Phi 1$ families ($\{1\bar{1}00\}$) with lattice spacing of a_1 , electron waves from top and bottom layer interfere destructively, resulting in reduced DF-TEM intensity, while $\Phi 2$ families ($\{\bar{2}110\}$) reflections have a large structure factor with constructive interference of all atoms due to the vertically aligned corresponding lattice lines (Figure 2.6).

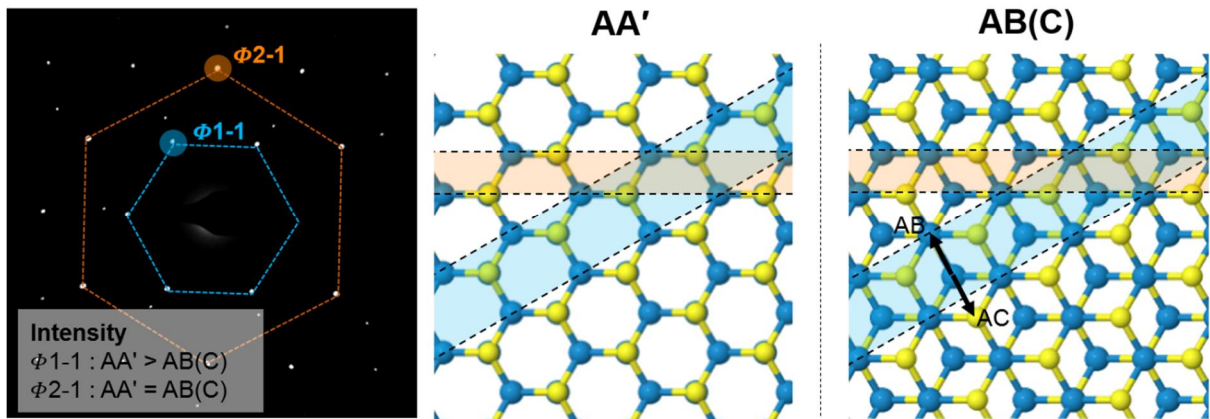


Figure 2.6. AA' and AB(C) stacking structures of TMDs. The lattice lines corresponding to $\Phi 1$ and $\Phi 2$ diffraction spots in SAED (left panel) are highlighted in blue and orange in atomic models of AA' and AB(C) stacking orders, respectively. Transition metal and chalcogen atoms are shown as blue and yellow, respectively.

For 2D materials with three-fold symmetry (*e.g.* MoS₂, WSe₂), six $[1\bar{1}00]$ diffraction peaks ($\Phi 1$) in selected area electron diffraction (SAED) pattern are divided into two families, transition metal- and chalcogen-sublattice-based spots, and the former have higher intensities due to the higher atomic scattering factor³⁴. Therefore, DF-TEM is useful for determining APB between inverted grains, which have same one set of hexagonal diffraction spots but asymmetric intensities. Likewise, compared to the graphene, AB and AC stacking orders in TMDs show asymmetric intensity of $\Phi 1$. Below figures show the various stacking orders of bilayer WS₂ and corresponding binding energy (Figure 2.7) and Bloch-wave simulation results using Mac-TempasX and intensity profiles according to the stacking configurations (Figure 2.8).

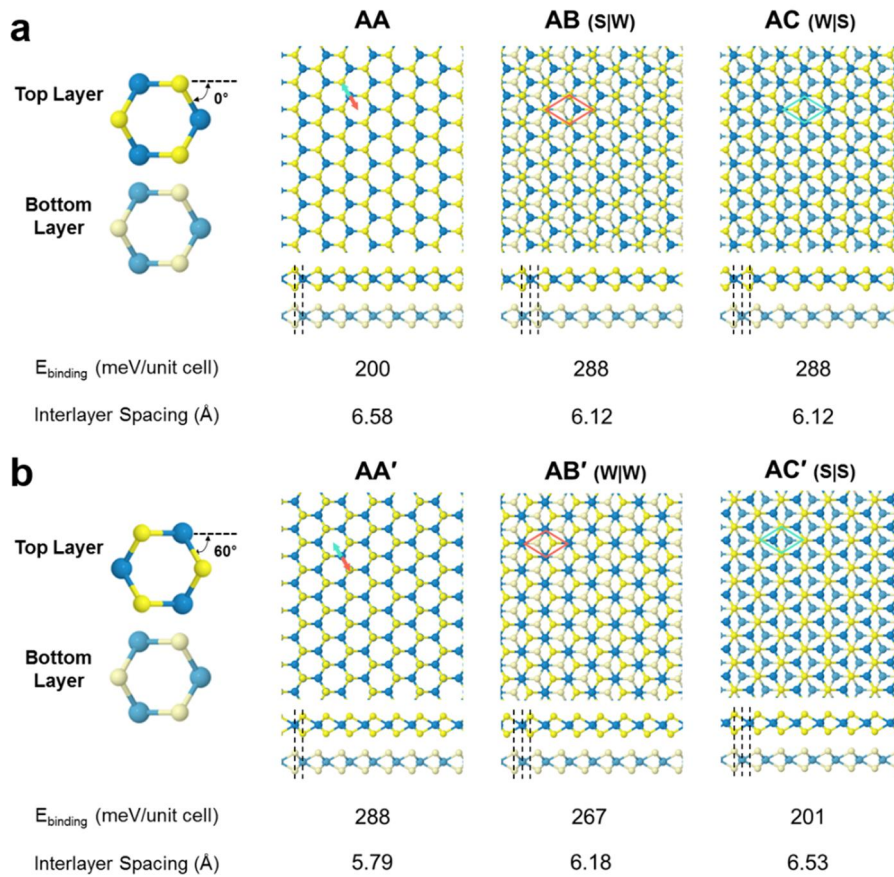


Figure 2.7. Various stacking geometries of WS₂ bilayers and calculated formation energies and interlayer spacing. WS₂ bilayer stacking configurations could be categorized according to their interlayer rotation angle, (a) $\theta = 60^\circ$ and (b) $\theta = 0^\circ$, and their interlayer translation is denoted as red and green arrows in AA' and AA stacking. Here, prime (') indicates a 60° interlayer rotation angle. B(C) represents Bernal stacking with tungsten(sulfur) atom in the bottom layer of an overlaid atomic column. For example, AB indicates a sulfur atom on a tungsten atom at an overlaid atomic column. Despite their mirror symmetry between AB and AC stacking orders, we distinguished them for convenience of explanation in here.

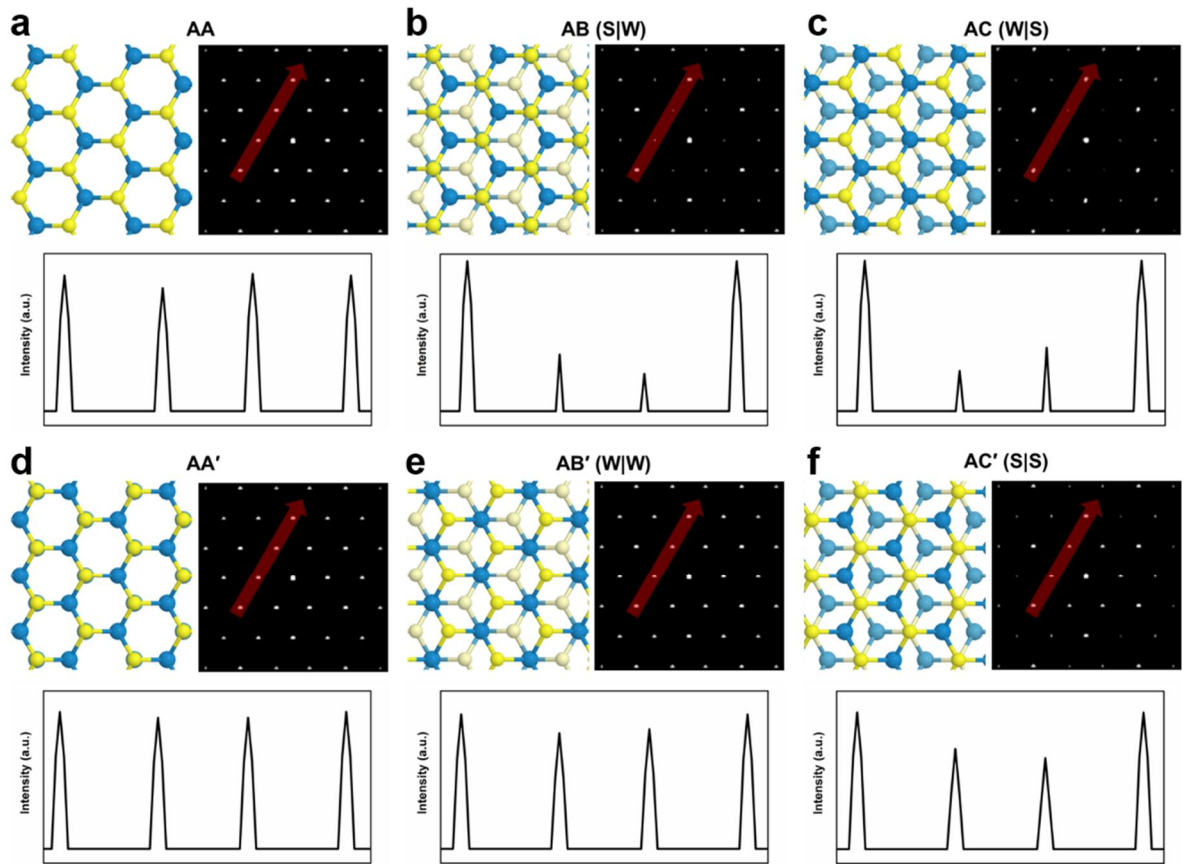


Figure 2.8. Bloch-wave simulation for various stacking configurations of WS_2 . Bottom panels are intensity profiles along the red arrows in simulated diffraction patterns. Due to the symmetry reduction from six-fold to three-fold symmetry from the bi-element nature of W and S, six first-order diffraction spots are divided into two families, W- and S-related diffraction spots. Thus, the intensities of two adjacent first-order diffraction spots are reversed for AA, AB, AC and AC' stacking geometries.

*Figure 2.7 and 2.8 was mostly reproduced from reference⁸⁸.

As mentioned above, DF-TEM intensity is sensitive to the phase shift. The $\{\bar{2}110\}$ DF-TEM image is useful for the Burgers vector analysis of Shockley partial dislocations, with Burgers vector $b = (1/3)\langle 01\bar{1}0 \rangle$, causing transition region between ground stacking configurations. In $\{\bar{2}110\}$ DF-TEM results, AB/AC SBs are shown as dark lines on bright bilayer region because the relative shifts at SB region reduces the local diffracted intensity. By applying the invisibility criterion, the transition line is pale when the direction of diffraction vector is perpendicular to the direction of Burgers vector⁸⁹ (Figure 2.9).

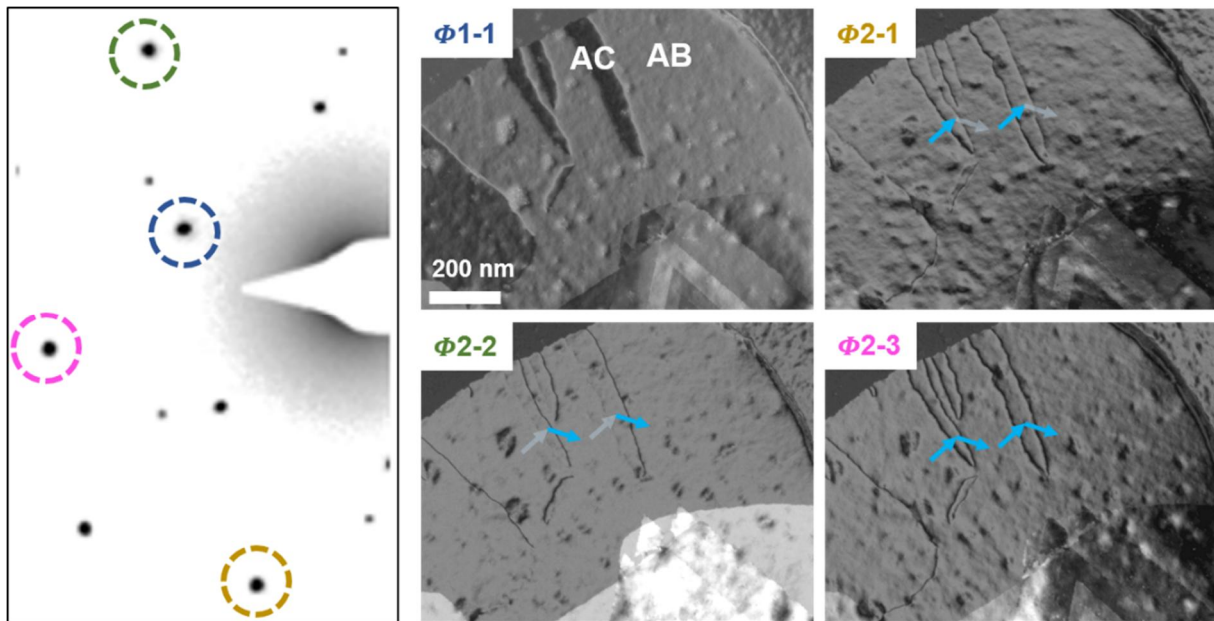


Figure 2.9. Determination of Burgers vector using series of $\{\bar{2}110\}$ DF-TEM analysis. Blue arrows indicate the burgers vector direction using second-order DF-TEM images.

2.3.2. Identification of low angle GB using artificial moiré pattern

This chapter was mostly copied from reference⁹⁰.

Developing a facile identification method of GBs is a crucial for systematical study of polycrystalline materials, because GBs affect the various properties of materials⁹¹⁻⁹⁴ (*e.g.* mechanical and electrical properties). SAED pattern⁹⁵ and fast Fourier transform (FFT) from atomic resolution images^{96,97} are useful to identify GBs by marking the transition peaks of diffraction peaks, but they have strong difficulties for identifying low-angle GBs, because adjacent diffraction spots are overlaid by the finite volume of diffraction spots. Moiré patterns are generated by the superposition of equi-spaced straight lines⁹⁸ and could amplify tiny imperfections (*e.g.* distortions, displacements) in lattice images⁹⁹. Because the moiré pattern shows a distinct shape and different periodicity depending on the interlayer rotation angle^{100,101}, two types of moiré patterns are produced when one layer including a GB is overlaid on the other single-orientation layer.

Although intralayer misorientation angle (θ^{1-2} , 1(2) means grain 1(2) in one layer with GB between grain 1 and 2) is low (*i.e.* low-angle GB), the difference of interlayer rotation angle (θ_3^1 or θ_3^2 , 3 means grain 3 of pristine bottom layer) makes different superlattice domains (shown as moiré patterns) across the GB as shown in Figure 2.10. It means that the degree of GBs identification could be controlled by the θ_{Bot}^{Up} , although the θ^{1-2} is the same. In detail, the superlattice periodicity, called moiré fringe spacing, in a bilayer homo-structure (*e.g.* graphene bilayer, MoS₂ bilayer) depends only on θ_{Bot}^{Up} , because of the same lattice parameters in each layer. Therefore, we call that as rotational moiré fringe spacing (d_{rm}) and its expression for d_{rm} is

$$\text{Rotational moiré fringe spacing: } d_{rm} = \frac{d}{2 \sin \beta/2}, \beta = \begin{cases} \frac{\pi}{180} \theta & , \theta \leq 30^\circ \\ \frac{\pi}{180} (60 - \theta) & , \theta > 30^\circ \end{cases} \quad (1)$$

where d is the $\{1\bar{1}00\}$ plane spacing of graphene, which is 2.13 Å and β is the interlayer rotation angle in radian. θ is rotation angle in degree, which has different condition at 30°. It follows negative exponential function shape from 0° to 30° as shown in Figure 2.11a (*i.e.* drastically decreasing at low rotation angle below 5°). It results in that the difference in moiré fringe spacing becomes larger (*i.e.* easily distinguishable) as rotation angle is decreasing, even in low misorientation angle (Figure 2.11b).

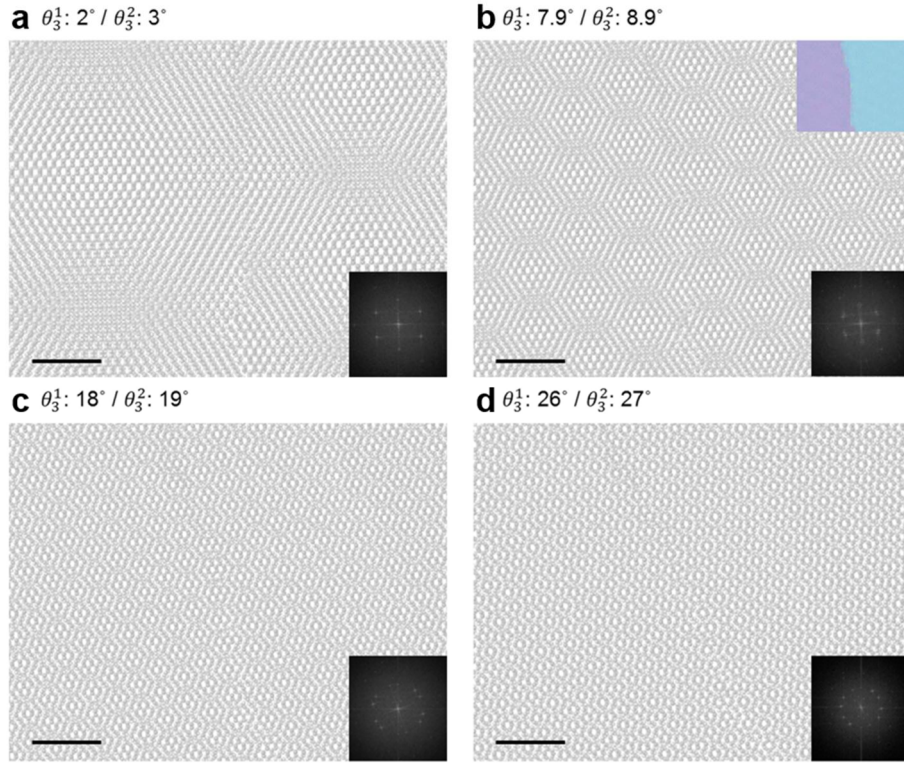


Figure 2.10. Moiré pattern according to the rotation angle including low-angle GB. (a-d) Bilayer graphene atomic models showing various θ_3^1 / θ_3^2 values with identical θ^{1-2} . Reference rotation angles θ_3^2 are (a) 3°, (b) 8.9°, (c) 19° and (d) 27°, respectively. Insets of (a)-(d) are FFTs of atomic models. Scale bar, 2 nm.

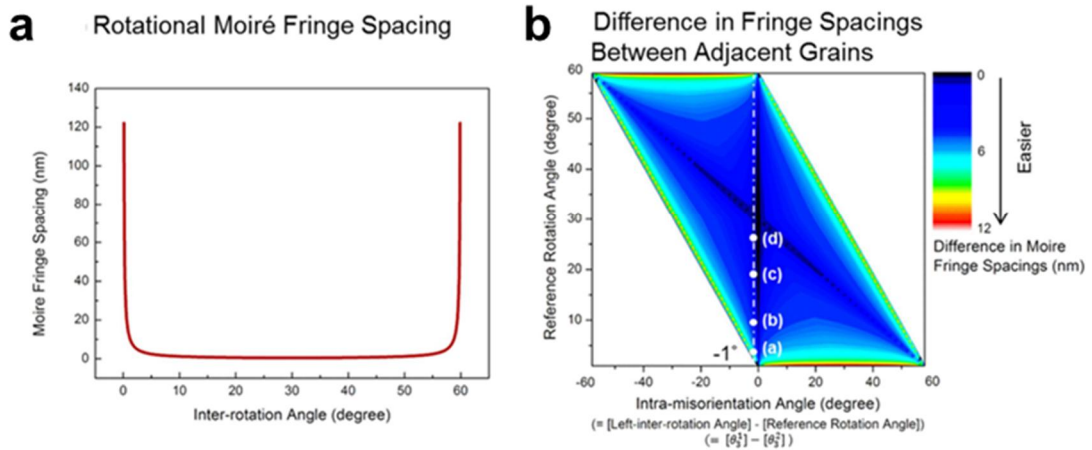


Figure 2.11. Rotational Moiré fringe spacing and difference in spacing across the GB. (a) The dependence of θ_{Bot}^{Up} on rotational moiré fringe spacings in rotated graphene bilayers. (b) Moiré fringe spacing differences as a function of intra-misorientation angle and reference rotation angle. The GB distinguishability is shown in color. Red color represents the easier identification of GBs. Marked (a-d) corresponds to Figure 2.10 (a-d).

The above results could be applied to an artificial moiré pattern by adding an artificial reference layer, mentioned by Hetherington and Dahmen⁹⁹. Moiré patterns are generated by the stacked artificial layer on the experimental TEM image. The difference in moiré fringe spacings varied from minimum to maximum, which means GB can be identified obviously by rotating the artificial reference layer. A bigger difference in moiré fringe spacings makes the detection of GB much easier. For example, there is a TEM image with a small angle GB, which is not shown evidently, as shown in Figure 2.12a. In contrast, the overlaid image in Figure 2.12b demonstrates the GB can be observable by adjusting the rotation angle of the artificial overlay to make the proper difference of moiré fringe spacings. This method could be applicable for all of materials by overlaying corresponding atomic model and rotating.

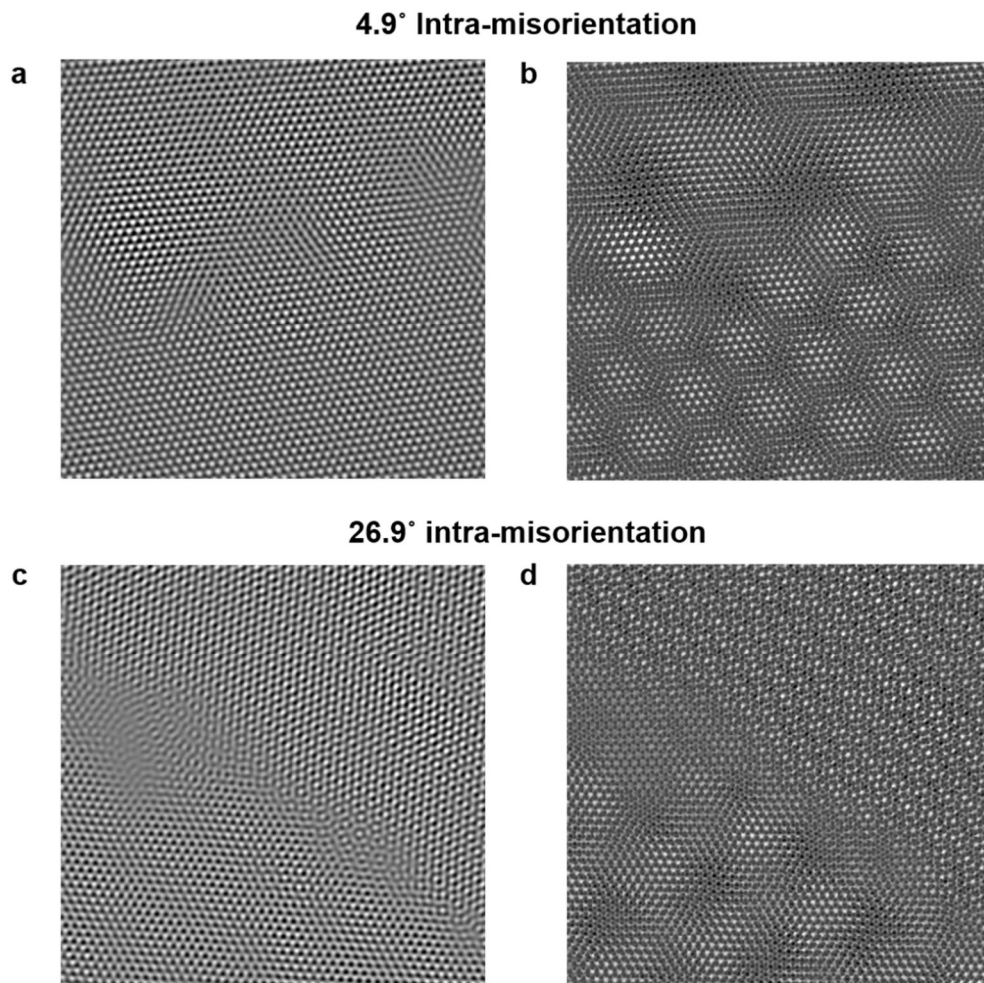


Figure 2.12. Identification of GB by overlaying artificial layer. (a,c) The processed TEM images of graphene with two tilt grains. The images are obtained with inverse FFT of bilayer graphene. (b,d) The TEM images overlaid with reference layer. (a,b) have small θ^{1-2} and (c,d) have relative big θ^{1-2} . Insets are color overlay images to show the grains more clearly.

2.3.3. Electron beam irradiated defect generation

High-energy electron beam in TEM is strongly applied to generate structural defects deliberately. Threshold energy to create chalcogen vacancies in TMDs is in the order of tens to hundreds of keV accessible in modern TEM. Therefore, sulfur vacancies in TMD layers are easily generated under the energetic electron beams due to the lower knock-on threshold voltage, resulting in smallest hole¹⁰². When the TMDs are exposed to the continuous electron beam, the mobile sulfur vacancies are migrated and agglomerated into vacancy lines²⁹ or nanopores¹⁰³. The MoS₂ nanopores are applicable as a DNA detecting sensors with superior performance for transverse detection without interaction between DNA and the surface¹⁰⁴. Chalcogen-deficient environment by electron-beam (e-beam) irradiation induces (1) APB inducing metallic wires in semiconducting matrix¹⁰⁵ and (2) phase transition by gliding massive one side of chalcogen atoms⁷⁹.

Recently, e-beam combining external stimulus (*e.g.* heat), additional energy source, manipulate novel defects. For example, a single W atom vacancy in WS₂ at 500 °C, which is a balance between thermally activated S vacancy diffusion and initiating local atomic reconstruction, transforms into the self-limiting nanopores with sub-nanometer diameter¹⁰⁶.

Chapter 3. Metallic anti-phase boundary of TMDs grown on the pristine graphene

3.1. APBs in TMDs

Point defects in TMDs (*e.g.* vacancy, adatom, dopants, *etc.*) make additional discrete gap states, leading to non-zero electronic states within the band gap^{35,107}. Likewise, GB, one of line defects in MoS₂, generates defect state from the Mo 4d orbital at the 5–7 dislocation cores^{37,108}, and tunes the band gap locally at the boundary¹⁰⁹. Meanwhile, APB, a special GB between two crystals which have the same crystallographic orientation but have 180° phase shift each other, has dispersive mid-gap states across the Fermi level, forming as 1D metallic nanowires embedded in the 2D semiconductor matrix^{34,110}, and it might be applicable to fully 2D-integrated circuit. Recently, Barja *et al.* reported that the APB in MoSe₂ monolayer exhibits CDW through Peierls distortion at low temperature, which also indicates the 1D metallicity of the APB¹¹¹. In the case of the 2H phase of TMDs, the conductive 1D APBs could be manipulated in several ways. First, e-beam irradiation in TEM manipulates the dense networks of APBs from the chalcogen-deficient environment^{105,112} due to the low knock-on threshold voltage of chalcogen atoms in TMDs¹⁰². Second, the epitaxial growth of TMDs on a particular substrate (*e.g.* sapphire^{38,113}, graphene¹¹⁴, h-BN¹¹⁵) is facile method for manipulation of high probability of APBs, because of the confined nucleation orientation. Various energetically stable APB structures were represented depending on which elements face to face (*i.e.* transition-metal-facing and chalcogen-facing)¹¹⁰, but in all previous experimental reports^{34,38,116}, a dense network of chalcogen-facing APB (denoted as S_{rhomb} in Chapter 3.3) was mainly observed, followed by kinks (denoted as W-S-W in Chapter 3.3).

In a 2D system, APBs form nanometer scale facets of ±20° relative to the ZZ direction due to the AC edge effect, another stable edge state^{34,117}. In this section, we studied anisotropic features of APB depending on what elements are encountered in the single-layer WS₂ using the multimode of TEM. WS₂ flakes are directly grown on the pristine graphene substrate for having a high probability of APBs using vdW epitaxy. Interestingly, although S-facing and W-facing APBs exhibit different overall features (*i.e.* straight for S-facing APB, saw-toothed for W-facing APB), both types of APBs have the same atomic configurations, consisting over- or under-coordinated of S atoms. These experimental results are reinforced by the DFT calculations to investigate the energetically stable atomic configurations of APBs. Conductive atomic force microscopy (C-AFM) results show that both types of APBs exhibit metallic wires due to the same 4- and 8-membered atomic configurations^{34,110}, but the two-probe field effect (FET) transistor device results show reduced electron mobility in saw-toothed transition metal-facing APBs, indicating that the connection between each facet (called as kinks) could act as dominant electron scattering center. This result suggests that global structures have a significant effect on transport behavior as well as atomic-precision configurations.

3.2. Experimental methods

Synthesis of WS₂ flakes on graphene. Graphene for underlying template was grown on 25- μ m-thick Cu foils (Alfa Aesar, 99.8 % purity) using a hot-walled CVD system. The strips of Cu foil were electrochemically polished in phosphoric acid for 15 min to clean the bare Cu surface and were subsequently rinsed with distilled water followed by isopropyl alcohol. Then the Cu strips were loaded into a 4-inch quartz tube followed by evacuating the chamber to \sim 3 mTorr; the temperature was then increased to 1,000 \sim 1,050 $^{\circ}$ C under an H₂ environment (H₂ flow rate of 5 sccm). After annealing of the Cu strips for 10 min, the graphene was synthesized by introducing methane gas (CH₄ flow rate of 10 sccm) and then cooling under the same conditions. Following the growth, graphene layers were transferred onto SiO₂/Si for further investigation using a conventional wet transfer method assisted by poly(methyl methacrylate) supporting layer and an aqueous solution of 1 M ammonium persulfate. Afterwards, the growth of WS₂ was carried out on using a two-zone furnace system with a tungsten trioxide (WO₃) thin film as the W source and S powder (99.998 %, Sigma-Aldrich) as the S source. For the uniform source, 1 nm of WO₃ thin film was evenly deposited onto SiO₂/Si using an e-beam evaporator (WO₃ pellets, Tae Won, 99.99%). The obtained graphene substrate was placed face-to-face on top of WO₃ film. This WO₃/Gr assembly was loaded at the center of the heat zone of the furnace, with S powder containing boat at the upstream of the furnace. Before heating, the whole furnace system was purged with 500 sccm Ar gas (99.999 %). Then, 30 sccm Ar was introduced into the system as a carrier gas and the system was gradually heated up to 950 $^{\circ}$ C. After reaching 950 $^{\circ}$ C, S powder was started to melt (heated to 200 $^{\circ}$ C) using the equipped heating jacket and kept constant for whole growth process (40 min).

Fabrication of MoS₂ FETs with Ti/Au contacts. To synthesize MoS₂ FETs, MoS₂ flakes were synthesized on silicon chip with 285 nm SiO₂ using powder-based CVD with a NaCl as a growth promoter. Prior to growth, 25 mg NaCl was dissolved in 10 mL distilled water for the 0.1 M NaCl promoter solution. A small droplet of 10 μ L of promoter solution was pipetted on the corners of an additional SiO₂ substrate. Afterward, baked out at 90 $^{\circ}$ C in order to remove the water completely. Two substrates, one for growth and the other with promoter, were loaded with the sputtered 5-nm-thick MoO₃ film face-to-face at the center of the quartz furnace, and 15 mg sulfur powder in alumina boats was placed in the upstream of the CVD system. After purging with 1000 sccm Ar flow, the CVD growth was then performed at atmospheric pressure with a continuous flow of 100 sccm Ar gas. The temperature of the furnace was gradually raised to 750 $^{\circ}$ C. When the temperature of the furnace approached \sim 715 $^{\circ}$ C, S powder was started to melt (heated to 230 $^{\circ}$ C) using equipped heating jacket and remained for 10 min of the whole growth process. Then, the MoS₂ channel regions were defined by using e-beam lithography (NBL, NB3) and Ar plasma etching. Next, the Ti/Au (10/80 nm) electrodes were contacted using the e-beam lithography and e-beam evaporator (Temescal FC-2000). Thermally

grown 300-nm-thick SiO₂ layer on heavily p-doped Si was used as the back-gate insulator. Any heat treatment after the fabrication was not conducted to avoid thermal budget effect. Electrical characterization was performed in a probe station (Lakeshore CRX-4K) equipped with a Keithley 4200-SCS detector at room temperature.

Structural Characterization. To investigate the synthesized W(Mo)S₂, scanning electron microscopy (SEM) measurements were performed in secondary electron (SE) and backscattered electron (BSE) modes using a cold field emission SEM (Hitachi SU-8220) operated at an accelerating voltage of 1 kV. C-AFM experiments were operated at a DC bias of 300 mV, while biasing through conductive Pt-Ir coated tips with a normal resonance frequency of ~13 kHz and a spring constant of ~0.2 N/m. TEM observations were performed using a FEI Titan cube G2 60-300 TEM equipped with image- and probe-aberration correctors. Dark-field mode was used for analyzing exact orientation of W(Mo)S₂ and confirming the global features of APB. Atomic resolution TEM (AR-TEM) and atomic resolution STEM (AR-STEM) modes were used for investigating atomic configurations of each type of APB. Before TEM experiment, the WS₂/graphene heterostructures grown on SiO₂/Si substrates were directly transferred to TEM grids using the conventional wet-transfer method without supporting polymer coating. All TEM experiments were operated at an acceleration voltage of 80 kV.

DFT calculations. WS₂ APB models were constructed as ZZ nanoribbons for DFT calculation. Note that the optimized monolayer WS₂ model was well agreed with experimentally reported lattice parameters (*i.e.* $a = b = 3.16 \text{ \AA}$). The width of optimized WS₂ nanoribbon was ~ 4.7 nm where APBs were in the center of the nanoribbon. Note that vacuum regions were introduced about 30 Å in parallel and perpendicular direction to the WS₂ nanoribbon (*i.e.* $80.0 \times 3.2 \times 29.5 \text{ \AA}^3$) to avoid the self-interactions. All spin-polarized DFT calculations were performed using DMol³ code^{118,119} under generalized gradient approximation with Perdew-Burke-Ernzerhof functional¹²⁰. All electron core treatment including relativistic effect was adopted with DNP 4.4 level and real-space cutoff of 4.9 Å. The smearing value was set to 0.005 Ha. The Monkhorst-Pack scheme¹²¹ was used to sample the Brillouin-zone as follows: $5 \times 5 \times 1$ for monolayer WS₂ unit cell, and $1 \times 5 \times 1$ k-points for WS₂ zigzag nanoribbon models, respectively. The convergence criteria for geometry optimizations of all considered model systems were set to 1.0×10^{-5} Ha, 0.002 Ha/Å, and 0.005 Å, for energy, maximum force, and maximum displacement, respectively. The reaction paths for structural transitions between S-facing and W-facing APBs were examined by transition state search calculation using linear and quadratic synchronous transit method with the conjugated gradient refinement¹²², where the RMS convergence criteria was set as 0.01 Ha/Å.

3.3. Structural analysis of two types of APBs

3.3.1. Characterization of orientation and overall structure of APB in synthesized WS₂

Single-layer WS₂ flakes were synthesized on a pristine graphene substrate using CVD method¹¹. Figure 3.1a and 3.1b show the DF-TEM and SAED results of single-crystal WS₂ flake grown on the graphene, respectively. As mentioned in chapter 2.3.1, six $[1\bar{1}00]$ diffraction spots (white-shaded) are divided alternately by k_W and k_S , and they indicate tungsten- and sulfur-related plane, respectively, due to the 3-fold symmetry of WS₂. Therefore, the intensity profile in the Figure 3.1b shows different intensities at k_W and k_S , due to the different atomic form factor of tungsten and sulfur³⁴. Through the DF-TEM and SAED analysis, we can estimate that the WS₂ flakes are terminated with W-edge in our growth condition (Figure 3.1 and Figure 3.2). In addition, WS₂ diffraction spots ($a = 0.272$ nm, white-shaded circle) are well-aligned with graphene diffraction spots ($a = 0.213$ nm, green-shaded circle), indicating that the WS₂ flakes are epitaxially grown with the most energetically preferred orientation^{11,114}. In the large field-of-view, SEM result in Figure 3.3a shows various ribbon-shaped WS₂ flakes formed by merging two inversion domains due to the confined nucleation orientation *via* vdW epitaxy. Combined flakes involve inevitable GB and especially called as APB for this 180° phase shift case. The height analysis using the AFM (Figure 3.3b) shows that the merged flakes have a uniform single-layer thickness of ~ 0.7 nm across the APB.

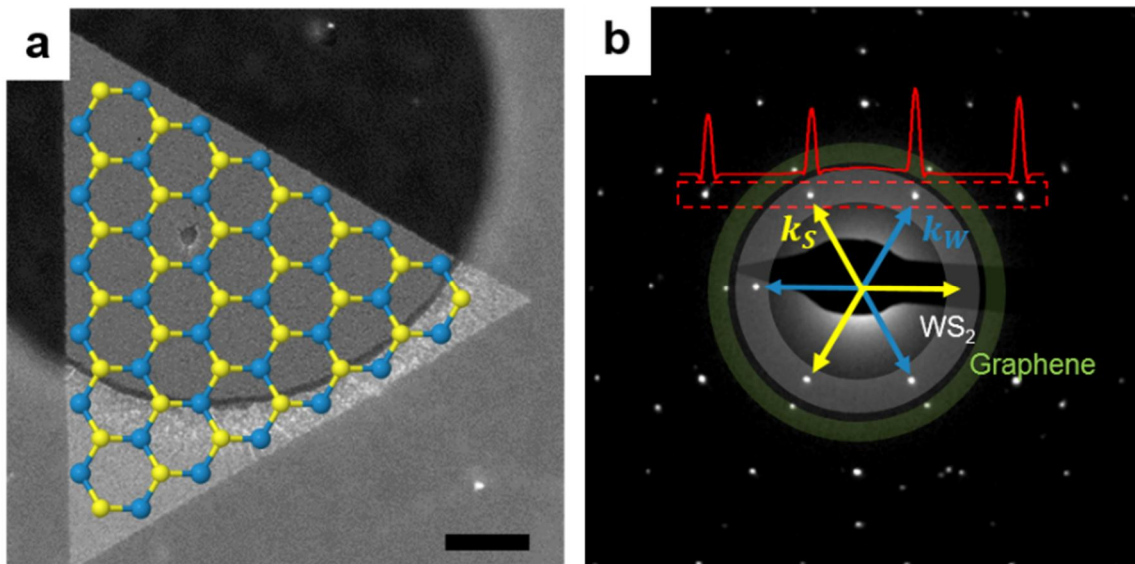


Figure 3.1. Epitaxial growth of WS₂ on graphene substrate. (a) DF-TEM image and (b) SAED pattern of WS₂ flake directly grown on the graphene substrate. S and W sublattices induce two different intensity of $[1\bar{1}00]$ diffraction spots (inset), represented by k_S and k_W . Scale bar for (a), 200 nm.

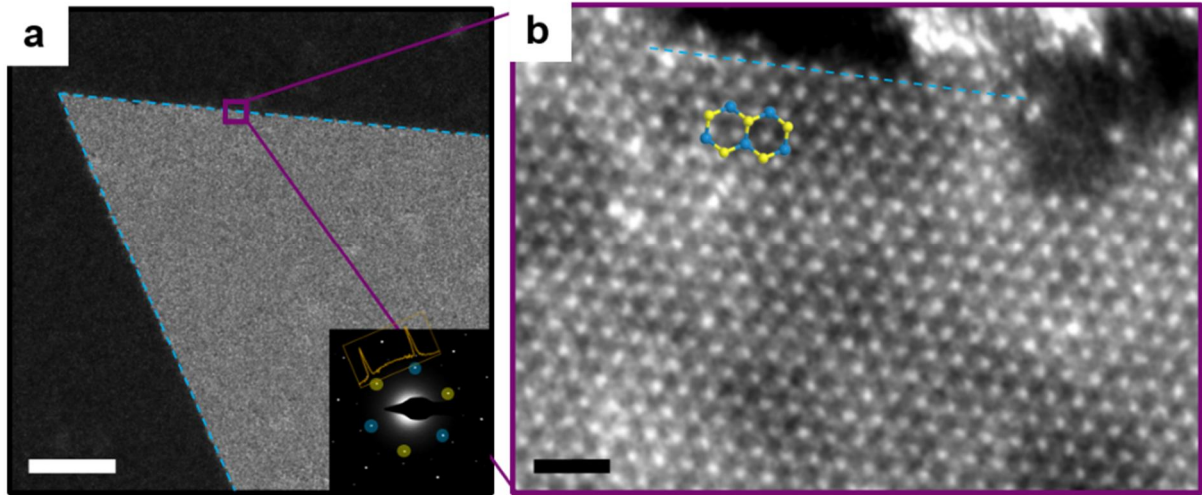


Figure 3.2. Tungsten terminated growth of WS₂. (a) DF-TEM image and SAED pattern (inset) of WS₂/graphene heterostructure. (b) AR-STEM image of the WS₂ edge region. Blue dotted lines in (a,b) represent W-ZZ line. Scale bars for (a) and (b), 100 nm and 1 nm, respectively.

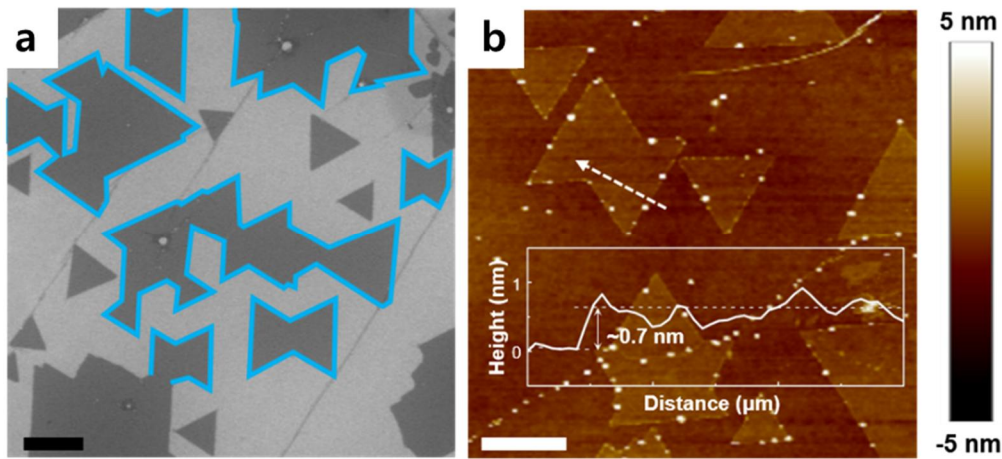


Figure 3.3. High probability of APBs in WS₂ grown on the pristine graphene. (a) SEM image of WS₂/graphene heterostructure. WS₂ flakes have a specific orientation due to the vdW epitaxial growth of WS₂ on the graphene substrate, resulting in ribbon-shaped flakes with APBs. (b) AFM height image of merged WS₂ flake and its line profile across the APB. Scale bars for (a,b), 500 nm.

To investigate the systematic study of two types of APBs, DF-TEM and high-angle ADF (HAADF) STEM analysis were used to examine global and local structures of two types of APBs as shown in Figure 3.4. DF-TEM results in Figure 3.4a and b are obtained using adjacent $[\bar{1}100]$ diffraction spots (given in the insets in $\Phi 1$ in Figure 3.4a,b), representing red-square regions in bright-field TEM (BF-TEM) images (insets in $\Phi 2$ in Figure 3.4a,b). Although there is only one set of hexagonal diffraction spots in SAED pattern, DF-TEM results represent the existence of two grains merged with an inevitable APB. The possibility of layer boundary could be excluded, due to the uniform intensity in BF-TEM images. Using the different intensities at k_W and k_S in SAED pattern (Figure 3.1b), we can determine the exact orientation of each grain. Strikingly, W-facing APB in Figure 3.4a has the saw-toothed shape with discrete facets, while S-facing APB in Figure 3.4b has the globally straight shape. For MoS_2 films grown on the sapphire using physical vapor deposition (PVD) method (Figure 3.5), transition-metal-facing APBs have overall saw-toothed shape, while chalcogen-facing APBs have straight shape. Regardless of the substrate (which enables epitaxial growth), growth method, and TMDs type, APBs in all TMDs have anisotropic features, depending on which elements are encountered in front.

Figure 3.6a and b show the local directionality of the W-facing and S-facing APB using the HAADF-STEM, obtained from the black-dotted rectangular regions in Figure 3.4a and b, respectively. In the local view of S-facing APB, direction of APB (Figure 3.6b) is rotated approximately 17° from the S-ZZ line, which coincides with the results from the previous reports^{34,38}. Likewise, for W-facing APB, each facet is rotated around 20° from the S-ZZ line. Both two types of APBs are inclined from the S-ZZ line and compose identical atomic configurations of 4- and 8-membered rings. (Detailed configurations are described in next section) The inclined APB from the ZZ edge direction is related to the effects of AC edge¹¹⁷ (Figure 3.7). Facets in W-facing APB have the $\langle \bar{2}\bar{3}10 \rangle$ and $\langle \bar{2}3\bar{1}0 \rangle$ directions, which are the closest to the WS_2 AC edge direction. Insets in Figure 3.6a,b are inversed Fourier-filtered images by removing WS_2 lattice information, and they represent peculiar contrast at APB, showing untypical charge redistribution¹²³. From these results, we can deduce that APBs have different electronic characteristics compared to the semiconducting WS_2 matrix.

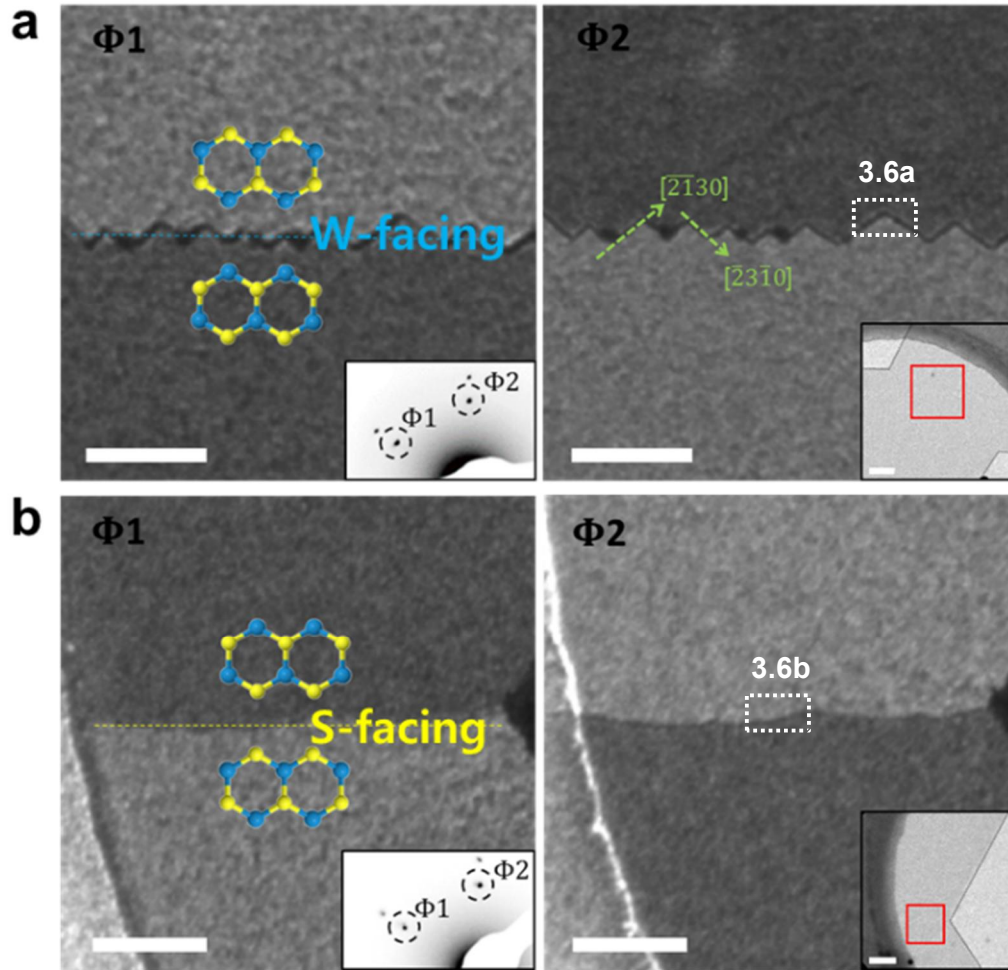


Figure 3.4. Anisotropic features of APBs in single-layer WS₂ according to the W-facing and S-facing. (a,b) DF-TEM images of W-facing and S-facing APB, respectively. Reverse contrast between $\Phi 1$ and $\Phi 2$ images represents existence of anti-phase between two grains. Insets in $\Phi 1$ and $\Phi 2$ are cropped SAED pattern and BF images, respectively. Blue (a) and yellow (b) dotted line indicate W and S ZZ direction, respectively. Scale bar, (a,b), 50 nm.

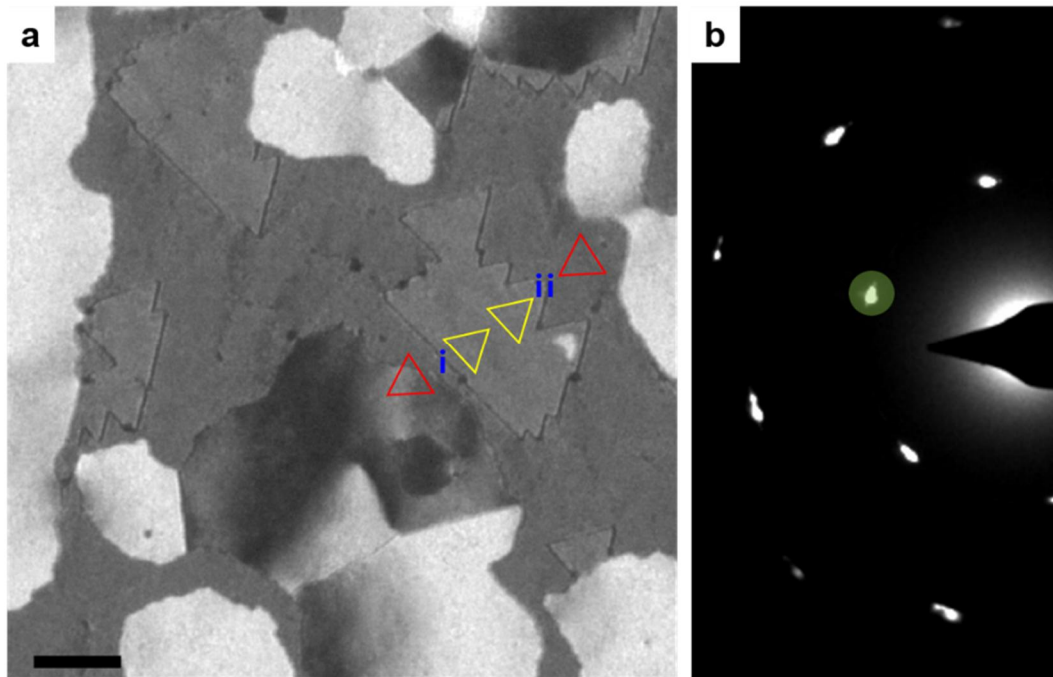


Figure 3.5. APBs in MoS₂ grown on the sapphire substrate. (a) DF-TEM image and (b) corresponding diffraction pattern. DF-TEM image is acquired by selecting yellow-shaded diffraction peak as shown in (b). Triangles in (a) indicate Mo sublattice. When the two triangles meet *via* S-facing (i case), it has straight APB. For the case of Mo-facing (ii case) APB has saw-toothed feature. Scale bar, 50 nm.

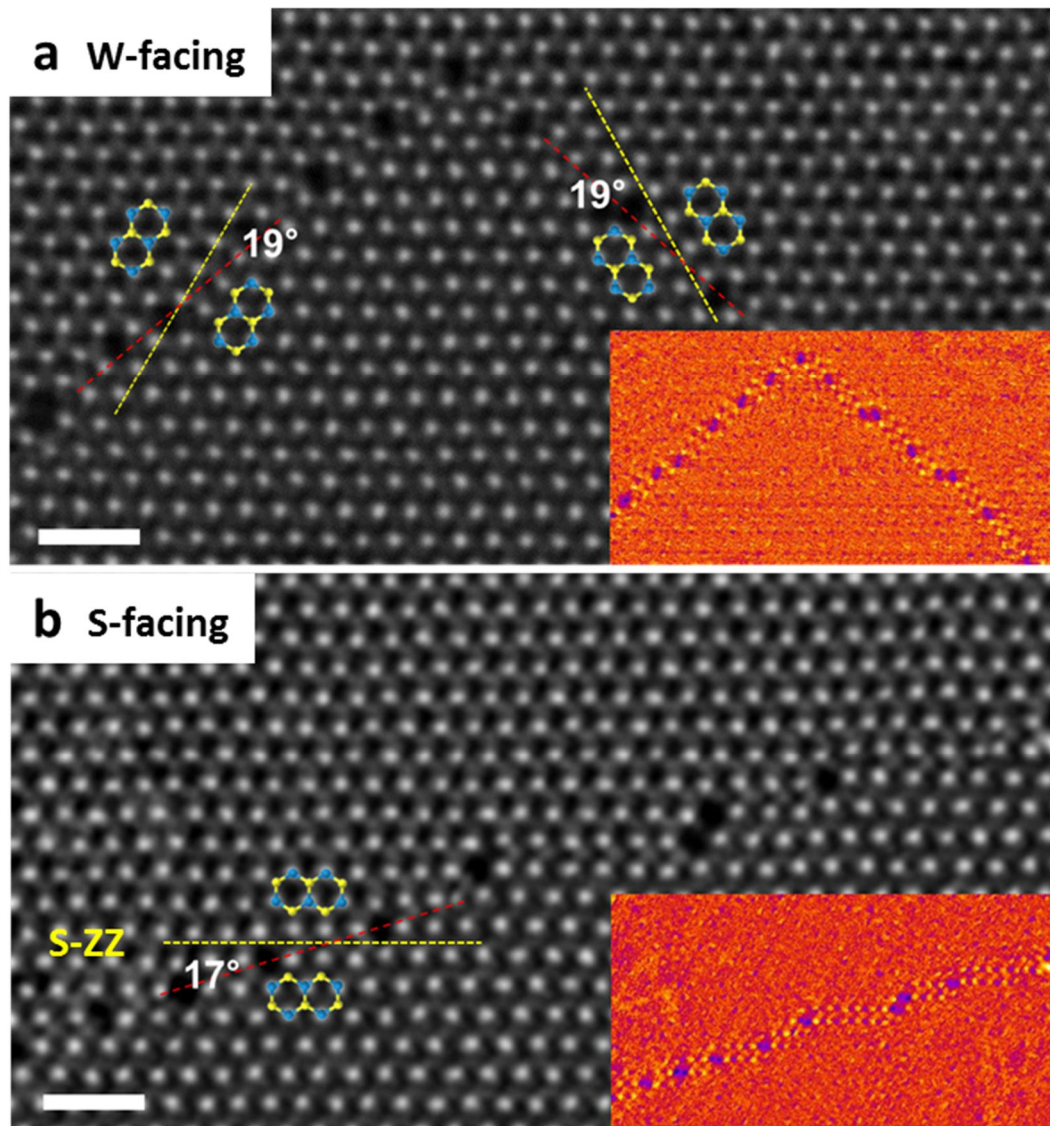


Figure 3.6. Atomic structures of two types of APBs. (a,b) AR-STEM images of saw-toothed (W-facing) and straight (S-facing) APBs, respectively. Each segment is rotated around 20° from the S-ZZ direction. Red lines show each segment direction of APB. Scale bar, 1 nm.

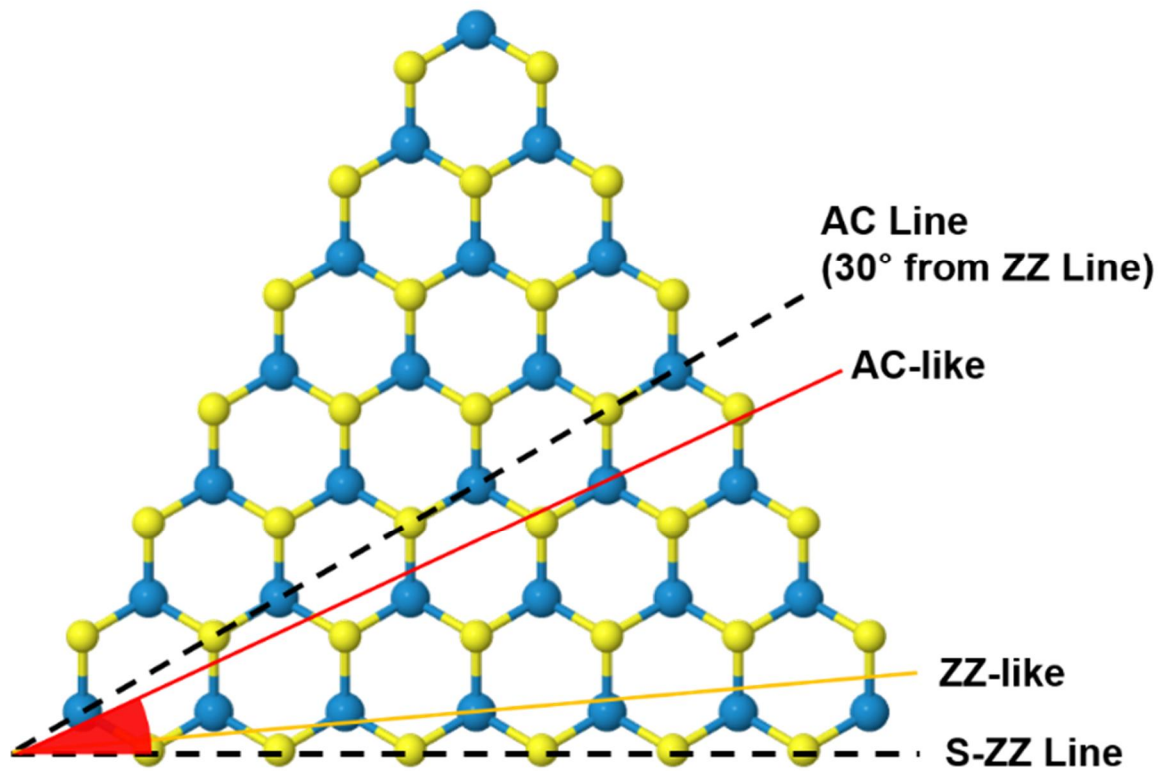


Figure 3.7. Inclined APB segments compared to the S-ZZ direction. AC edge influences the APB angle by controlling kink density.

3.3.2. Atomic configurations of WS₂ APBs

As mentioned before, APBs can be categorized into two groups according to the front-facing elements (*i.e.* S- and W-facing). Depending on how the unit cells of each grain meet, each group is divided into two representative cases (*i.e.* composing 4-membered or 8-membered configurations at the APB). Therefore, we consider the four possible APB structures, denoted as W-44, W-88, S-44, and S-88 (Figure 3.8a-d). The character W(S) means a W-(S-) facing APBs, and 44(88) denotes the number of atoms configuring one unit of APBs. While the considered atomic models for our calculation have mirror plane at the APB (Figure 3.8a-d), experimental results (Figure 3.6 and 3.8e) have atypical and segmental structures. Therefore, unit of APBs is introduced, and each unit of W-44, W-88, S-44, and S-88 is denoted as W_{rhomb} , W-S-W, S_{rhomb} , S-W-S, respectively. Figure 3.8e shows the atomic-scale structure of W-facing saw-toothed APB using AR-TEM analysis. The exact orientation of each WS₂ grain is determined using the S vacancy (denoted as yellow arrow in Figure 3.8e), which is easily formed under the e-beam irradiation¹⁰². Each facet is rotated around 22° from the S-ZZ line and consists of S_{rhomb} and W-S-W (Figure 3.8e and Figure 3.9), identical to the atomic configuration of S-facing APB in Figure 3.6a. Relaxed calculated structures are shown in Figure 3.10.

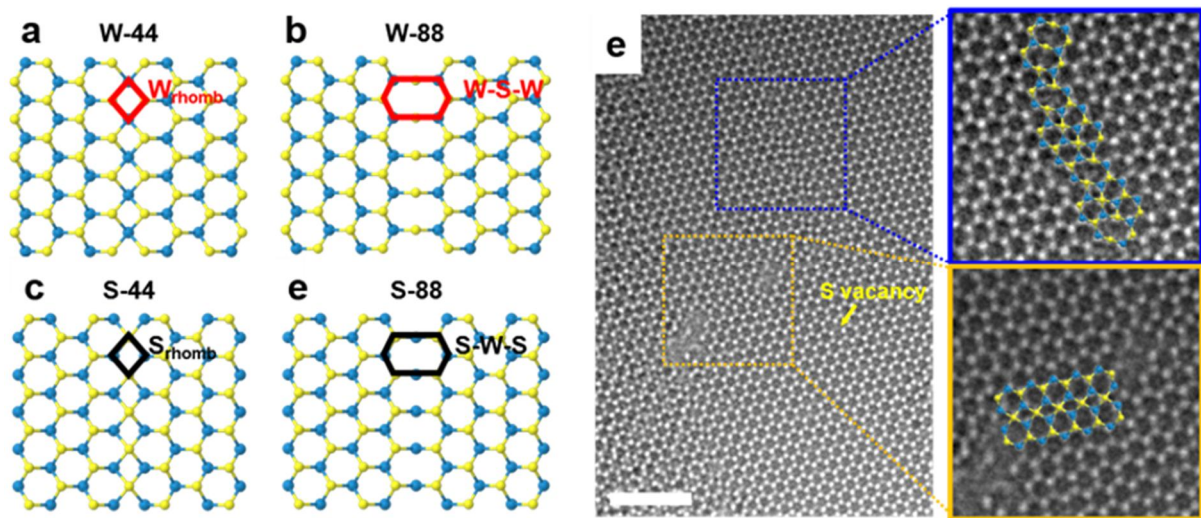


Figure 3.8. Possible atomic configurations of APBs. (a-d) Atomistic configurations of plausible WS₂ APB models, which involve (a) W-44, (b) W-88, (c) S-44, and (d) S-88, respectively. Units of each APBs are denoted as (a) ' W_{rhomb} ', (b) 'W-S-W', (c) ' S_{rhomb} ', and (d) 'S-W-S', respectively. (e) AR-TEM image of W-facing APB including mainly S_{rhomb} and some of W-S-W. Scale bar for (e), 2 nm.

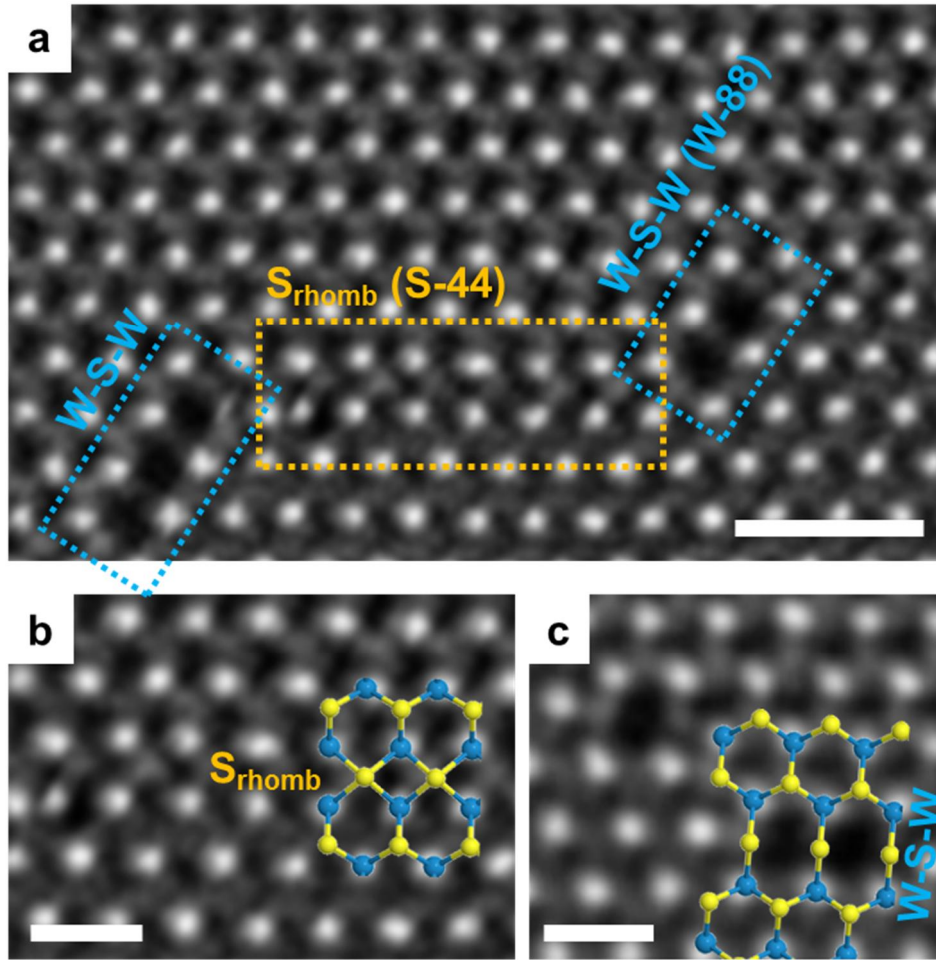


Figure 3.9. Experimental atomic configurations of W-facing APBs. (a-c) Experimental AR-STEM images of WS₂ APB. Each facet of APB includes only S_{rhomb} and W-S-W, rather than S-W-S and W_{rhomb} unit. Blue and yellow balls in overlaid atomic models represent W and S atoms, respectively. Scale bar, (a) and (b,c), 1 nm and 0.5 nm, respectively.

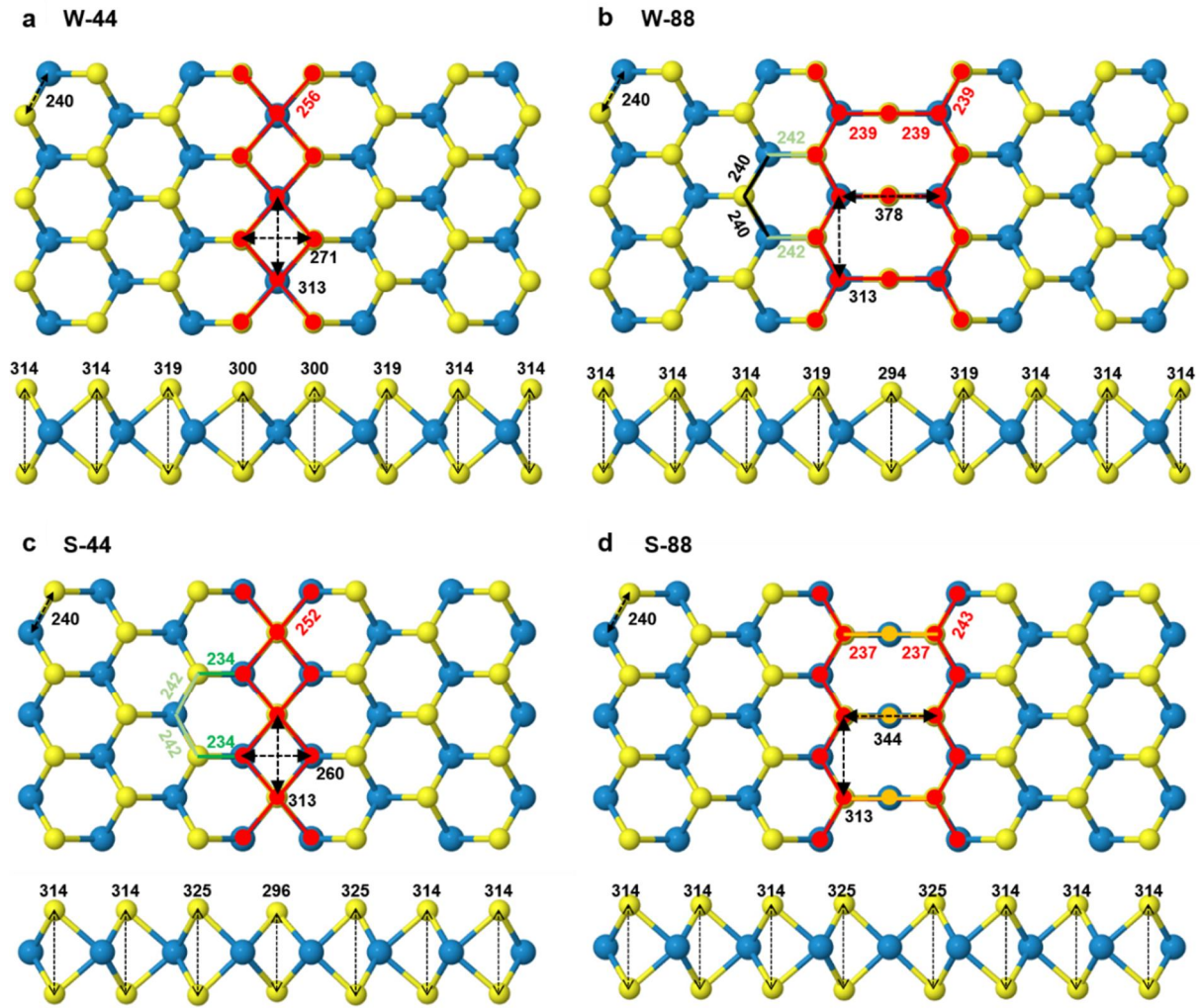


Figure 3.10. Relaxed atomic configurations of (a) W-44, (b) W-88, (c) S-44, and (d) S-88 APBs.
The marked numbers represent the bond length and the unit is picometer (pm).

3.3.3. Structural stability of APB configurations

To figure out the structural stability of APB configurations, DFT calculations were performed. Note that the edges for all APB models are constrained as 50% and 100% coverage of S atoms, which were calculated to be the most stable configurations for W- and S-edges by edge formation energy calculations (Figure 3.11). The edge formation energy (γ_{edge}) was evaluated using triangular WS_2 flakes by following equations,

$$3(\gamma_{edge} + \gamma_{vertex}) = E_{flake} - n_W E_{WS_2} + (2n_W - n_S)\mu_S \quad (1)$$

where γ_{edge} , γ_{vertex} , E_{flake} , n_W , E_{WS_2} , n_S , and μ_S mean the edge formation energy, formation energy of the vertex of the triangular WS_2 flake, total energy of the triangular WS_2 flake, number of atoms of tungsten, total energy of monolayer WS_2 unit cell, number of atoms of sulfur, and chemical potential of sulfur, respectively. Further details on the Equation (1) can be referenced in the earlier work by Schweiger *et al*¹²⁴. For γ_{edge} calculations, the boundary of $\Delta\mu_S$ was set between -1.22 and 0 eV, where the formation of bulk WS_2 became thermodynamically spontaneous. Computational result shows that the W-edges are the most stable for a whole range of $\Delta\mu_S$, corresponding to the experimental result (Figure 3.1 and Figure 3.2).

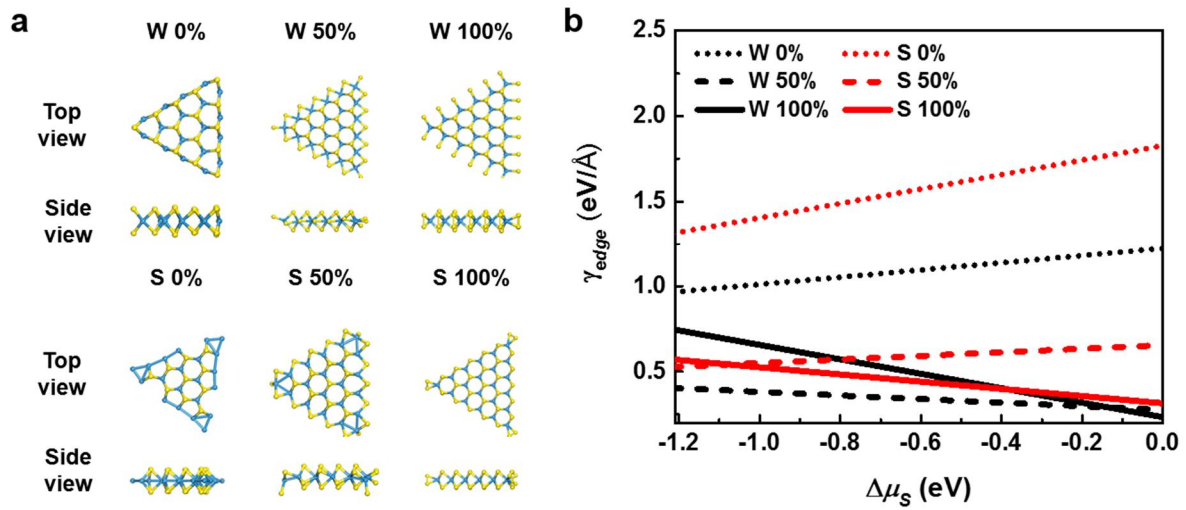


Figure 3.11. Edge formation energy calculation of WS_2 . (a) Optimized triangular WS_2 consisted of 18 and 21 W atoms of W-edge (top) and S-edge (bottom) models, respectively. (b) Edge formation energy normalized by length of the surface unit as a function of chemical potential of S. WS_2 becomes stable within the range of $-1.22 \text{ eV} < \Delta\mu_S < 0 \text{ eV}$ where the upper and lower limits correspond to S-rich and S-poor conditions, respectively.

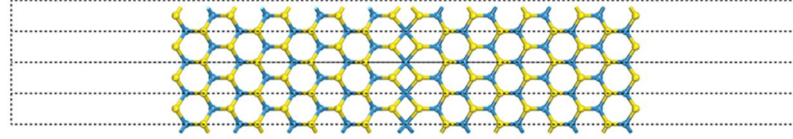
To obtain the stable configuration of APBs, the formation energy of APBs (γ_{APB}) was calculated by the following equation^{110,125} (Figure 3.12),

$$\gamma_{APB} + 2\gamma_{edge} = E_{slab} - n_W E_{WS_2} + (2n_W - n_S)\mu_S \quad (3)$$

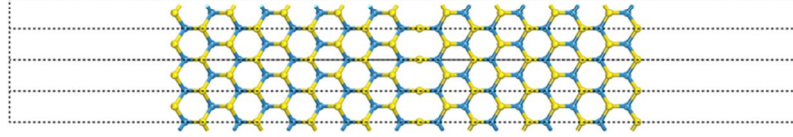
where E_{slab} referred to the total energy of WS_2 zigzag nanoribbon models. Like the edge formation energy calculation, the boundary of $\Delta\mu_S$ was set between -1.22 and 0 eV. The APB formation energy results show that S-44 and W-88 APBs were more stable than S-88 and W-44 APBs over the whole range of $\Delta\mu_S$ (Figure 3.13). Structurally more stable S-44 and W-88 APBs consisted of over- or under-coordinated of S atoms, respectively, while less stable S-88 and W-44 APBs involved the over- or under-coordination of W atoms, respectively, compared to the bulk WS_2 (Figure 3.14). Therefore, the rearrangements of W-coordinations of APBs are expected to cause higher endothermicity than those of S-coordinations of APBs.

a W-facing APBs

W-44

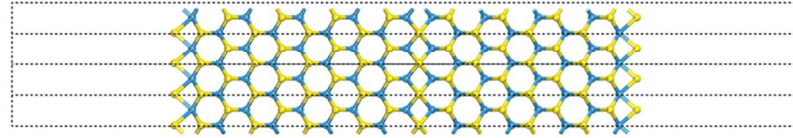


W-88



b S-facing APBs

S-44



S-88

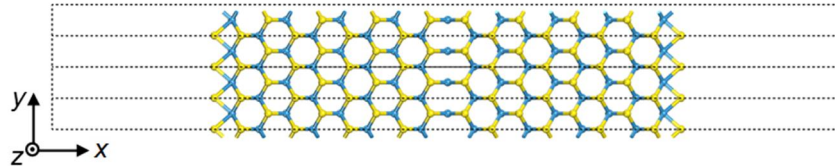


Figure 3.12. Atomic models for the formation energy calculation of APBs. (a) W-facing (W-44 and W-88) and (b) S-facing APBs (S-44 and S-88), where the S-edge and W-edge were terminated with 100% and 50% S coverage, respectively, which are based on the results of edge formation energy calculation in Figure 3.11.

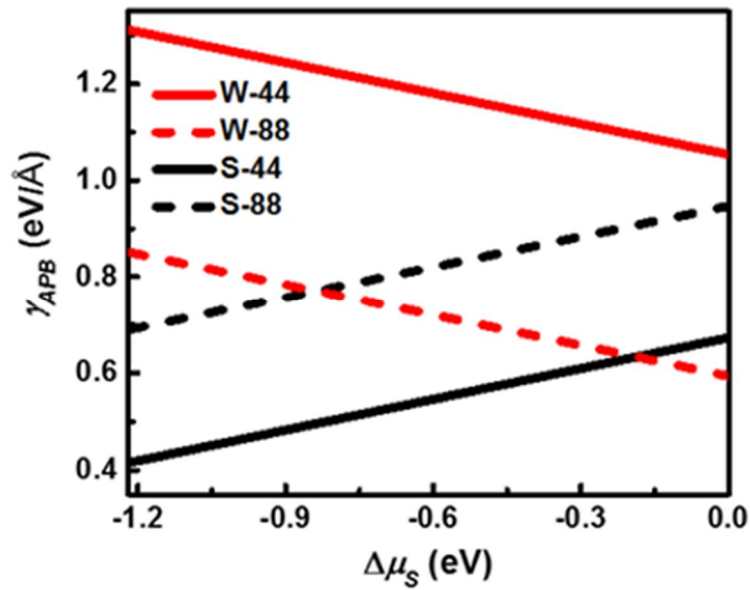


Figure 3.13. APB formation energy of S-facing and W-facing APBs as a function of chemical potential of sulfur. WS_2 becomes stable within the range of $-1.22 \text{ eV} < \Delta\mu_S < 0 \text{ eV}$ where the upper and lower limits correspond to S-rich and S-poor conditions, respectively.

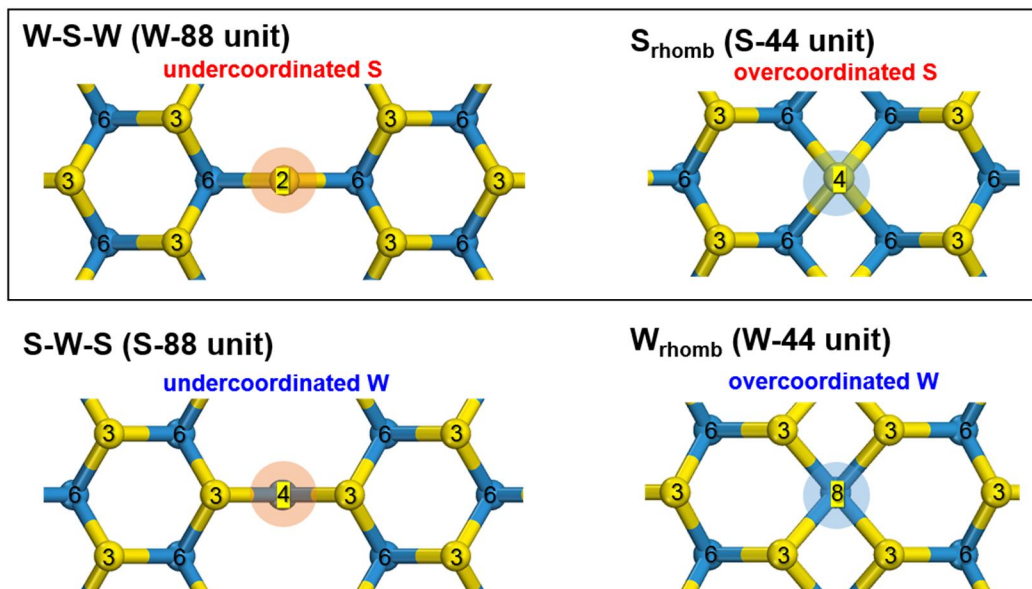


Figure 3.14. Coordination numbers of S and W atoms consisting of W-S-W, S_{rhomb} , S-W-S, and W_{rhomb} configurations. Red or blue circles indicate under-coordinated or over-coordinated S and atoms compared to the bulk ones, respectively. Black rectangle (top) shows the energetically more favorable configurations.

Next, we studied the structural transition between WS₂ APBs, which might be caused by sliding of one grain along the APB line (Figure 3.15). From checking the endothermicity of the reverse reactions, we expect that the transition might occur in only one direction for both S-facing APBs (*i.e.* from S-88 to S-44) and W-facing APBs (*i.e.* from W-44 to W-88) with slight or negligible energy barriers, respectively. Finally, S-44 and W-88 APBs are energetically more favorable than S-88 and W-44 APBs, respectively. Considering that the S-44 is energetically more stable than W-88 for a wide range of $\Delta\mu_S$, APBs have S_{rhomb} predominantly, followed by W-S-W, which is in reasonable agreement with experimental results (Figure 3.16). For both cases (*i.e.* W- and S-facing), although the ratio is different, S_{rhomb} configurations are dominant and followed by W-S-W. Previous researches reported that the W-S-W configurations act as kinks connecting adjacent segments by turning the direction of APBs^{34,38} and it is well consistent with our experimental results depicted in Figure 3.6, 3.8e and 3.9.

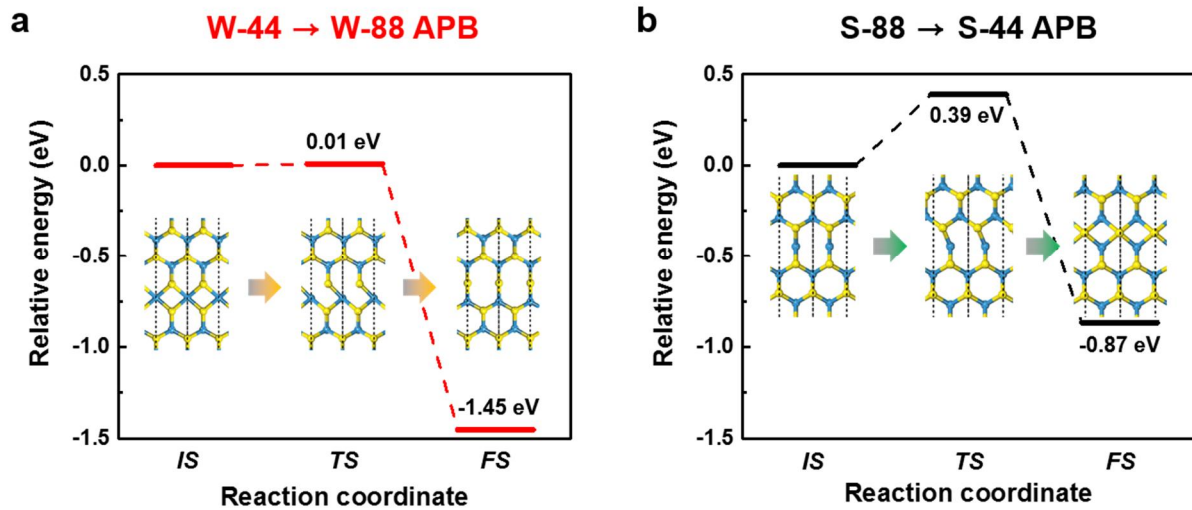


Figure 3.15. Energy diagrams of structural transition between (a) W-facing and (b) S-facing APBs. Insets indicate the corresponding atomic configurations for the initial state (*IS*) (*i.e.* W-44 for W-facing and S-88 for S-facing), transition state (*TS*), and final state (*FS*) (*i.e.* W-88 for W-facing and S-44 for S-facing) of the reaction mechanism.

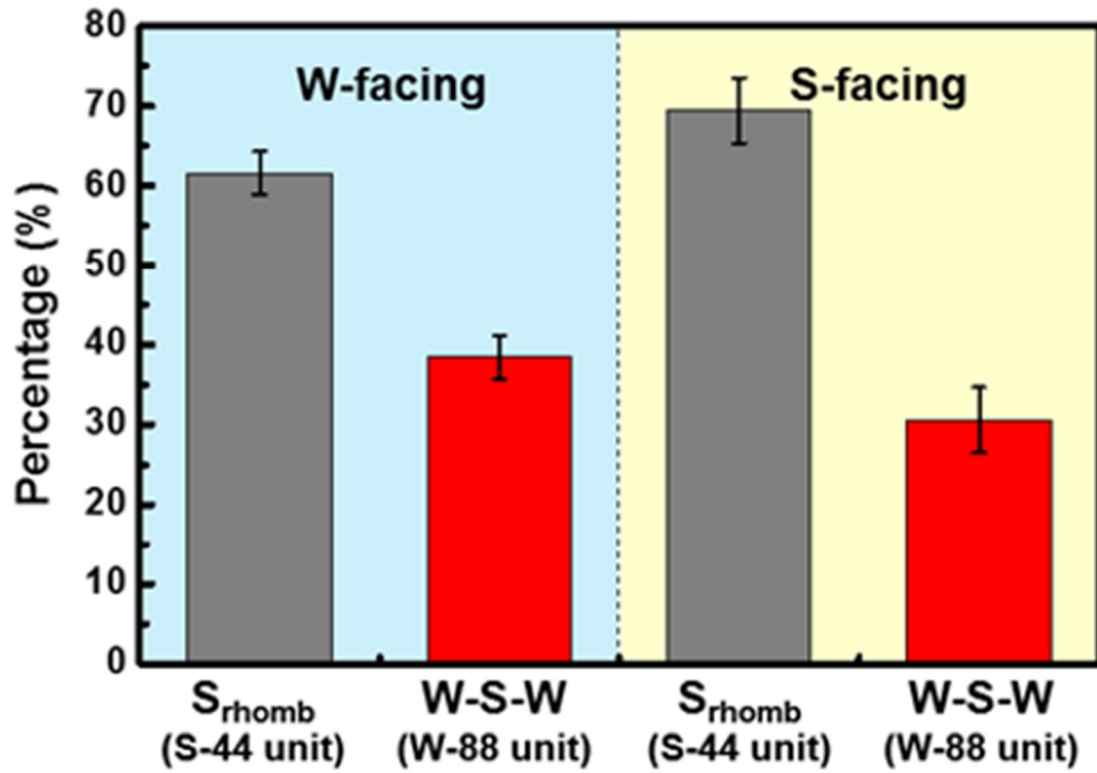


Figure 3.16. Distribution of S_{rhomb} and W-S-W units in W-facing and S-facing APBs. S_{rhomb} units exist predominantly, followed by W-S-W units, corresponding to the result of APB formation energy.

Previous studies showed that the TMDs have strikingly low-energy barrier for GB migration³⁶, which implies that the APBs in TMDs have a possibility to easily migrate and easily reconstruct to the lower energy state (*e.g.* faceting¹²⁶). Therefore, we annealed the WS₂ flakes at 150 °C and 200 °C for 1 hour to apply additional energy to overcome the migration barrier. We limited the annealing temperature to 200 °C due to the aging phenomena of TMDs starting from GBs and intrinsic surface defects¹²⁷. As depicted in Figure 3.17c-e, there is no APB migration or reconfiguration, representing a high migration barrier for APBs. To explain the discrepancy between the previous studies of GB migration³⁶ and our experimental results for APB migration, we performed the DFT calculation for S_{rhomb} APB migration (Figure 3.18). APB migration consisting S_{rhomb} configurations accompanies massive movement of tungsten atoms as much as *a* (distance between neighboring W and S), while GB movement takes place through the movement of few atoms³⁶. The calculated energy profile shows that the transition states have high energy state, indicating a high energy barrier to migrate APB. From the above all results, we can conclude that the anisotropy APBs are originally synthesized into a thermodynamically stable structure and does not migrate or faceting to the lower energy state.

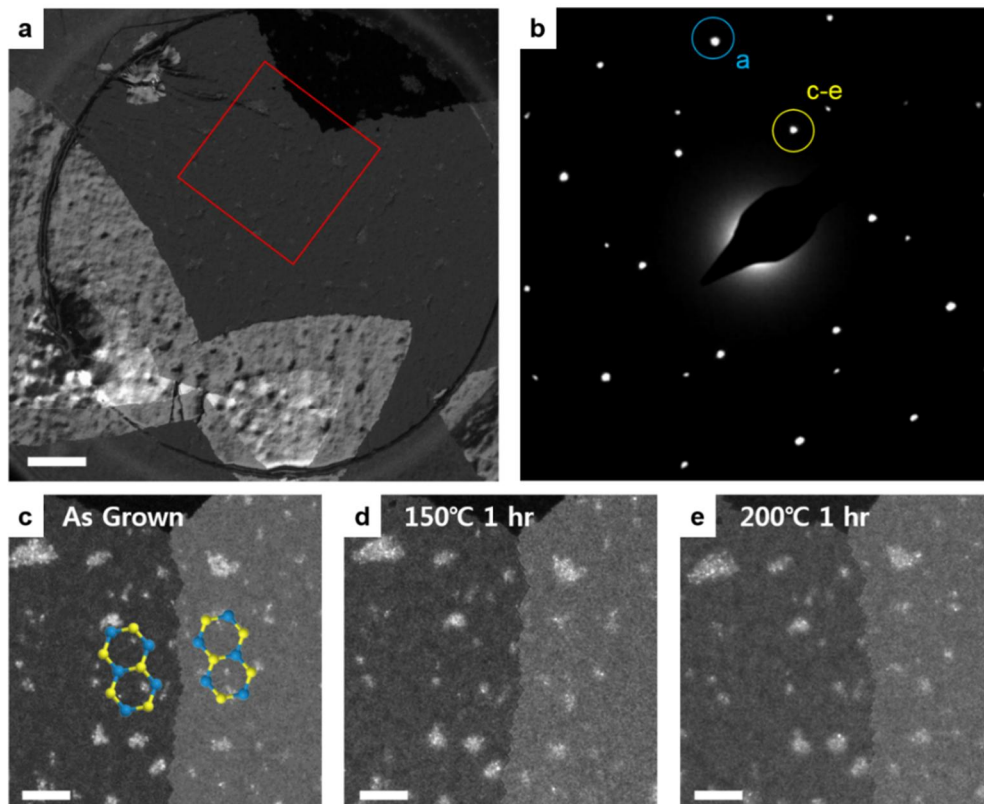


Figure 3.17. No migration of APBs under additional heat source. (a) 2nd order DF-TEM image, representing layer number of WS₂. (b) Corresponding SAED pattern of WS₂ and graphene heterostructure. (c-e), 1st order DF-TEM images displaying WS₂ APB with (c) as grown, (d) annealed at 150 °C for 1 hr and (e) annealed at 200 °C for 1 hr. Scale bar, (a) and (c-e), 200 nm and 100 nm, respectively.

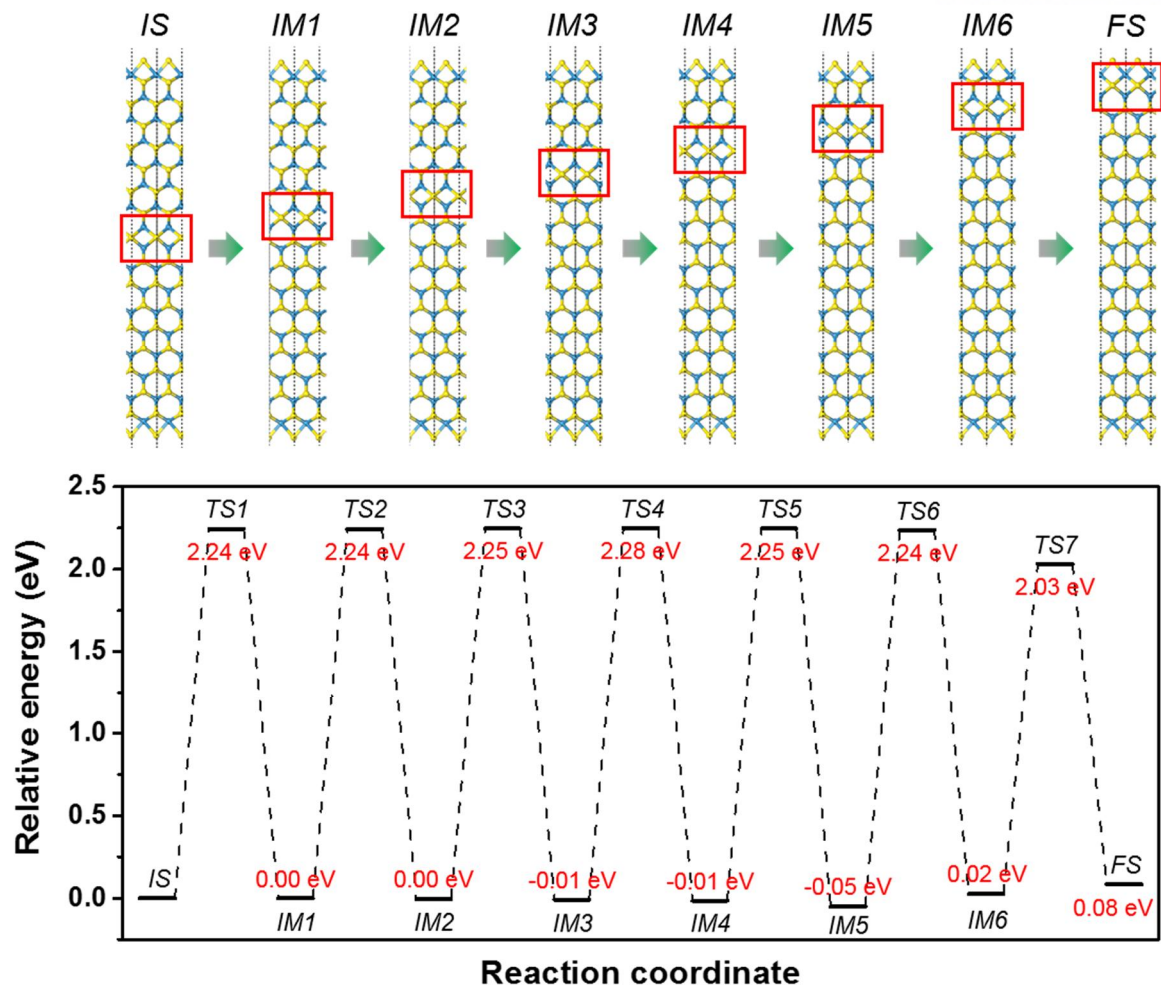


Figure 3.18. Optimized structures of S_{rhomb} APB and energy profiles of initial state (*IS*), transition state (*TS*), intermediate state (*IM*), and final state (*FS*) for migrating S_{rhomb} APB in WS₂ ZZ nanoribbon.

3.4. Electronic properties of X- and M-facing APBs

Metallic properties of all APB configurations are well known, because they have dispersive mid-gap states¹¹⁰. Metallicity at APB is commonly observed using scanning tunneling microscopy^{111,128,129}, due to the confined dimension of APB (around a few nanometer width). To evaluate out-of-plane charge transport at the APB, we performed C-AFM measurement using WS₂/graphene heterostructure. Graphene serves as a back electrode and a Pt-Ir-coated conductive tip was used to measure current as a function of *x-y* position in contact mode¹³. The height image of single-layer WS₂ including S- and W-facing APBs on graphene (Figure 3.19a) shows no contrast at APB, showing no height variation at APB (similar to the result of Figure 3.3b). Meanwhile, the simultaneously obtained current image shows different contrast at APB compared to the WS₂ basal plane as shown in Figure 3.19b. WS₂ flakes have lower current than the surrounding graphene, while enhanced electrical conductance is observed along the APB, indicating 1D metallicity at both S- and W-facing APBs with S_{thomb} and W-S-W atomic configurations.

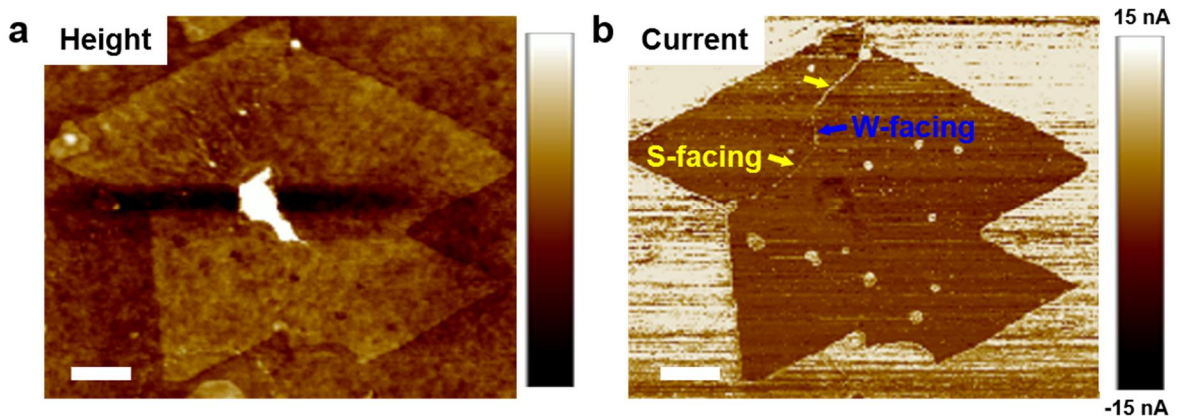


Figure 3.19. Local variation of electronic properties at APBs. (a,b) Height and current AFM images of APBs using WS₂ and graphene heterostructure, showing enhanced currents along the APBs compared to the basal plane region of WS₂. Scale bar for (a,b), 200 nm.

To study the collective effect of saw-toothed APB on the electrical performance, we fabricated large number (> 30) of FET devices of pristine MoS_2 flakes (denoted as $p\text{-MoS}_2$) and MoS_2 with S-facing APBs ($s\text{-MoS}_2$) and with Mo-facing APBs ($m\text{-MoS}_2$). To fabricate FET devices and measure the transport, we used large-area MoS_2 , another representative TMD materials, grown on SiO_2 , a typical dielectric layer. All types of devices were patterned into ribbons with $5\ \mu\text{m}$ channel length and $20\ \mu\text{m}$ channel width. Fabricated devices are illustrated in Figure 3.20.

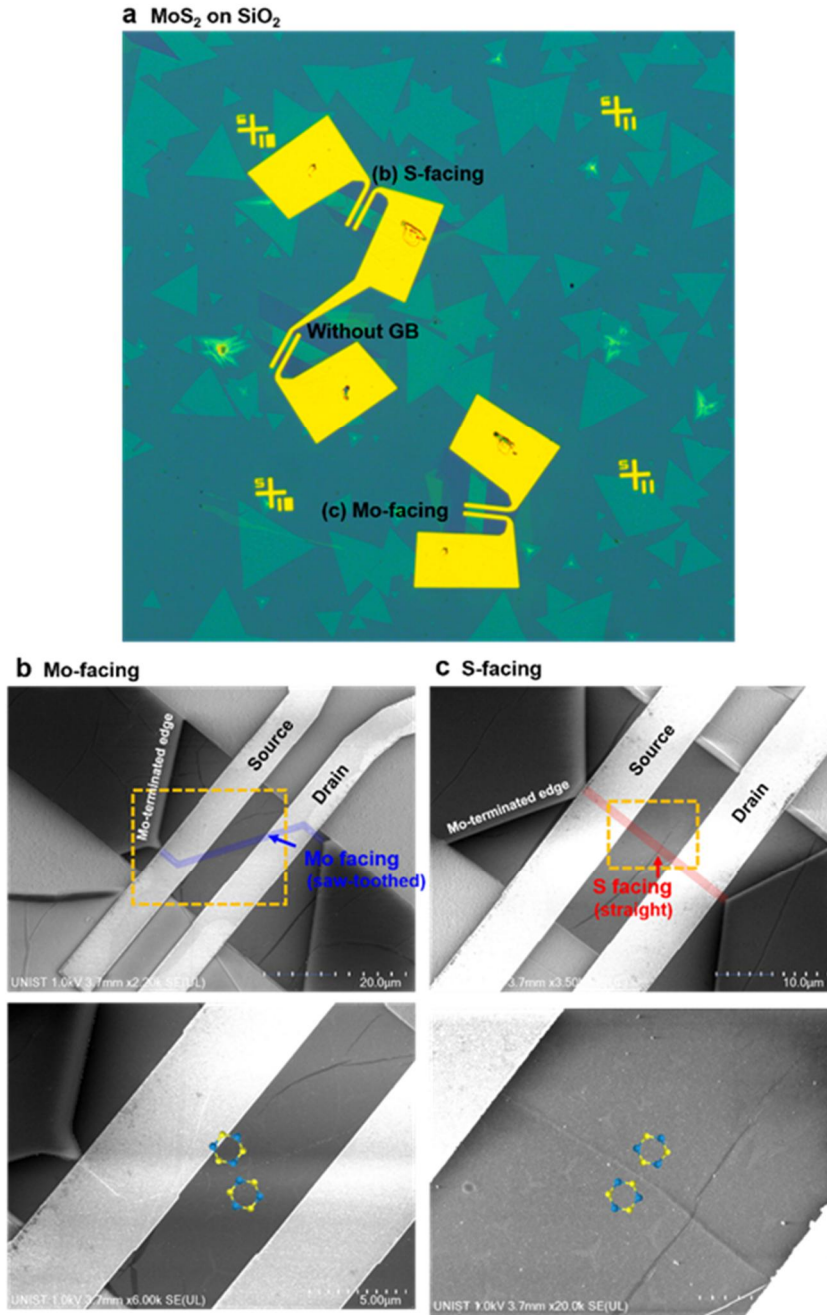


Figure 3.20. MoS_2 FET devices for investigating effect of facet in TMDs' APBs. (a) Optical microscopy image of FET with channel width and length normalization. (b,c) SEM images of FET devices with Mo-facing and S-facing APBs, respectively. SEM SE mode images display APBs faintly.

Figure 3.21a shows the logarithmic (solid lines) and linear (open circles) scale transfer curves of *p*-MoS₂, *s*-MoS₂, and *m*-MoS₂ devices measured at room temperature. The averaged on-state current (I_{on}) of *s*-MoS₂ devices at $V_{ds} = 1$ V is $\approx 3.4 \mu\text{A}/\mu\text{m}$, almost three times higher than that of *m*-MoS₂ device ($\approx 1.27 \mu\text{A}/\mu\text{m}$), although both APBs exhibit metallicity with identical atomic configurations. In addition, field effect mobility (μ_{FET}) was evaluated, according to the following equation (4)¹³⁰:

$$\mu_{FET} = \left(\frac{dI_{ds}}{dV_g} \right) \left[\frac{L}{WC_i V_{ds}} \right] \quad (4)$$

where L and W are the channel length and width, respectively, and C_i is the capacitance of the SiO₂ dielectric layer (11.5 nF·cm⁻² for 300 nm-thick SiO₂). The obtained μ_{FET} and threshold voltage (V_{th}) are summarized in Table 3.1. The averaged charge carrier μ_{FET} are $9.7 \pm 2.6 \text{ cm}^2/(\text{V}\cdot\text{s})$ and $3.7 \pm 2.5 \text{ cm}^2/(\text{V}\cdot\text{s})$ for transport along *s*-MoS₂ and *m*-MoS₂ devices, respectively (Figure 3.18b). To explain the difference in transport behaviors, we firstly checked the V_{th} , which is useful parameter for the estimation of Fermi level shift by the doping effects depending on the APBs (*e.g.* carrier density, $n \propto \Delta V_{th}$)²⁰. The obtained averaged V_{th} for *s*-MoS₂, *m*-MoS₂, and *p*-MoS₂ devices are similar, indicating that the doping effects by APBs were negligible. On the other hand, one could mention that the line defect density (*e.g.* the length of APB) is proportionally related to the degradation of electronic properties including μ_{FET} ²⁰. For our cases, the degrading ratios for the I_{on} (2.68) and μ_{FET} (2.62) of *m*-MoS₂ compared to *s*-MoS₂ were larger than the APB length ratio between *m*-MoS₂ and *s*-MoS₂ (1.88), indicating that another parameter influencing on the electron transport degradation exists rather than the defect density. In addition, *s*-MoS₂ devices show no adverse effect on the transport behavior compared to *p*-MoS₂ device²⁰, indicating that the atomic defects consisting APB do not highly degrade on the electrical transport.

As I mentioned above, previous researches reported that the W-S-W acts as kink³⁷ between facets and it leads to disordered random potential wells in S_{rhomb}-based periodic potential wells for APB. According to the localization theory¹³¹, as the density and depth of potential well is increasing, electronic wave function in the material becomes localized, which results in reduced electron transport with trapped free electrons. With the combination of increased kink density at W(Mo)-facing APB, we suggest that the reduced I_{on} and μ_{FET} of *m*-MoS₂ is due to the localized electron at the random disordered potential between facets acting as intrinsic scattering centers, whereas *s*-MoS₂ sustained its electronic transport behavior along the channel with an atomically faceted 1D metallic wire.

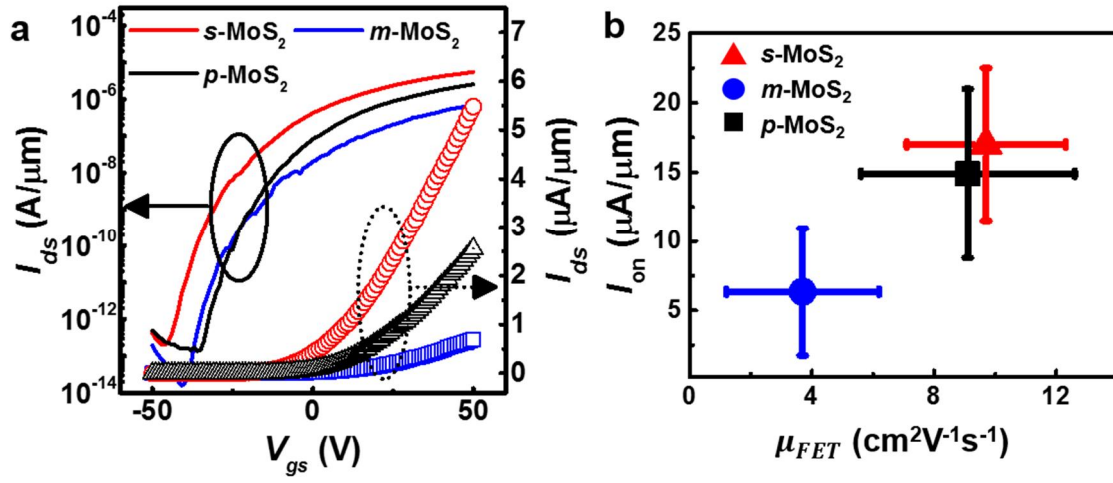


Figure 3.21. The effects of APBs on electron transport properties. (a) The logarithmic and linear scale transfer (I_{ds} - V_{gs}) curves at $V_{ds} = 1.0$ V and (b) On-current (I_{on}) vs. mobility (μ_{FET}) plots of p -MoS₂, s -MoS₂, and m -MoS₂ devices.

	s -MoS ₂	m -MoS ₂	p -MoS ₂
I_{on} [μA]	17.01 ± 5.5	6.35 ± 4.6	14.9 ± 6.1
μ_{FET} [$\text{cm}^2\text{V}^{-1}\text{s}^{-1}$]	9.7 ± 2.6	3.7 ± 2.5	9.1 ± 3.5
V_{th} [V]	12.4 ± 3.3	14.6 ± 5.3	15.2 ± 4.1

Table 3.1. Summarized transport properties of s -MoS₂, m -MoS₂, and p -MoS₂ devices.

3.5. Conclusion and outlook

Following the efforts of application to fully 2D-integrated circuit, several approaches have been progressed to achieve the electrode components with conducting properties of semiconducting TMDs. One possible scheme is the transformation into metallic 1T phase *via* intercalation-driven chemical exfoliation¹³² and electron radiation⁷⁹. Metallic edges¹³³ could also be fabricated by cutting into nanoribbons using a focused electron beam, and recently metallic nanowires could also be manipulated to form heterostructures with 2D TMD and 1D metallic wires. The advantages are strong due to their conducting properties, but metastable 1T phase and uneasy process for fabrication of metallic edges and nanowires (*e.g.* introduction of non-essential defect) lead to intrinsic limitations in realization and commercialization of the applications. In this regard, APBs could be the most effective method to overcome this limitation due to their facile manufacturing process and metallic properties.

In summary of this chapter, we represent that the anisotropic features of APB and different transport behavior using representative TMDs, WS₂ and MoS₂. We compared two types of APBs, transition-metal-facing APB and chalcogen-facing APB, having saw-toothed and straight overall structures, respectively. Using experimental and computational results, the anisotropic features of APB is for preserving the most energetically favorable configuration, called as S_{rhomb}. In addition, using the two-probe FET measurements, saw-toothed APB has lower electron mobility than the straight APB, because connection between each facet (kink; composed by W-S-W configuration) could be dominant scattering center. Our results reveal that the understanding of anisotropy of 1D APB defect depending on the facing-elements, which could not be imagined using theoretical expectation, and the influence of anisotropic structural features on the electronic transport behavior. It could provide the valuable insight in the microstructure-related electronic transport property study and could extend the applications of 2D materials with desirable properties *via* defect engineering.

Further research should study APBs in other TMDs (*e.g.* distorted 1T structure of WTe₂, triclinic ReS₂) other than the 2H phase, including atomic configurations of APBs and their electronic properties. In these materials, APBs and TBs have not been extensively studied due to their complex structures, but may have novel properties by charge redistribution at the defect site. To realize the programmable 2D materials using intentionally manipulated and engineered defects, a systematic understanding of the various defects and the establishment of structure-property relationships in the various types of TMD should be highly required.

Furthermore, TMDs have been considered as long-term air-stable semiconductors, which is strongly important for applications. Recently, however, initiating from non-stoichiometric defect sites¹²⁷ (*e.g.* chalcogen vacancy, GB), severe surface degradation of TMDs has been observed at ambient conditions,. Therefore, researches to enhance the air stability of TMDs have been widely noted. For example, the TMD/graphene heterostructure significantly enhances air stability by the charge-transfer-mediated doping effect¹¹. At this point, we focused on the large amount of edges due to aging. Similar to the APB configuration, which has an energetically stable atomic configuration despite the different overall structure, two types of edges (*i.e.* saw-toothed and straight) are observed in TMD, which are predicted to have energetically favorable edge configurations. Confined edge configurations are very useful for manipulating desirable properties (*e.g.* magnetic moment¹³⁴, spin order¹³⁵), so further study on atomic-scale aging mechanism, detailed atomic edge configurations, and edge engineering (*e.g.* edge decoration¹³⁵) is needed. It will make a big contribution to the field of material science.

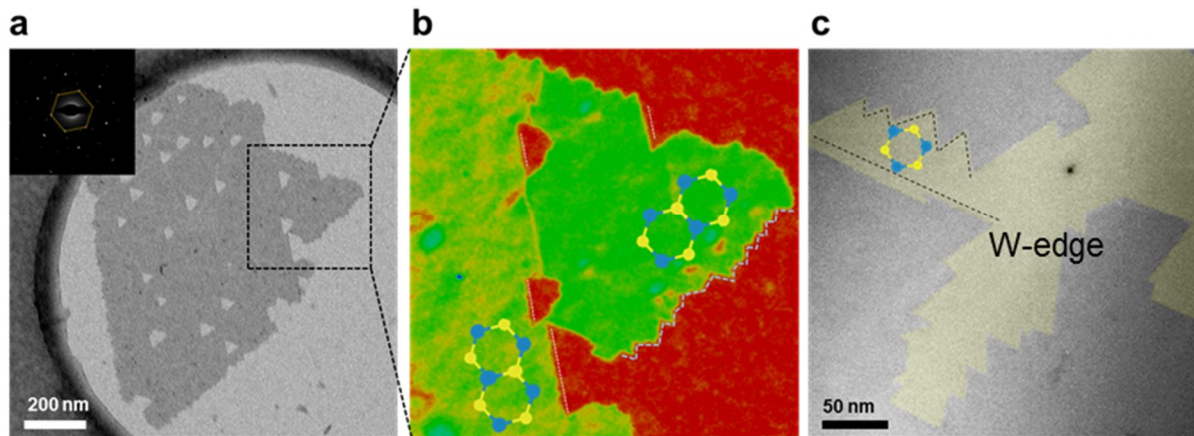


Figure 3.22. Two types of edge in degraded MoS₂. Edges have different overall structures to have energetically favorable edge configurations at atomic scale, similar to the case of APB. Blue and yellow balls in overlaid atomic model represent Mo and S atoms, respectively. Scale bar for (a) and (c), 200 nm and 50 nm, respectively.

Chapter 4. AB/AC stacking boundaries of TMDs grown on the wrinkled graphene

This chapter was mostly copied from reference⁸⁸.

4.1. AB/AC SBs in 2D materials

Dislocations in 2D materials are fundamental and important concepts in nanoscience^{57,89,136} and have received extensive interests due to their strong influence on local optical^{34,137}, electronic^{37,138-142} and mechanical properties^{89,143}. Edge dislocation is mainly composed of pentagon–heptagon (5–7) or square–octagon (4–8) pair in a monolayer hexagonal system (*e.g.* graphene⁵⁷ h-BN^{140,143} and 2H polymorph TMDs^{36,108}). Edge dislocation is moved in the basal plane of 2D material, in particular step by step along the ZZ lattice orientation through bond rotation or atom loss⁵⁷. In contrast, in a multi-layer or even a bilayer system, a dislocation is confined in the crystal in the form of a Shockley partial dislocation, which is dissociated from the perfect basal dislocation⁸⁹. This partial dislocation leads to strain soliton-mediated incommensurate state such as SB, acting as domain wall^{144,145}.

SBs, line defects between ground-state stacking domains induced by partial dislocations, have been hugely studied, particularly in the bilayer graphene system^{89,141,144-146}, because they impart graphene with novel properties, such as topological valley transport channels along the SB lines¹⁴¹ and reversible switching between metal and insulator¹⁴⁶. In h-BN flakes, two cases of SBs have been demonstrated due to various stacking configurations from the 3-fold symmetry⁸⁷. Similar to h-BN, TMD formulated by MX₂ (M=Mo, W, X=S, Se) has a variety of ground state stacking geometries^{147,148}, because of its low symmetry compared to graphene. On the other hand, few SB has been reported for bilayer TMD because GB predominates in TMD with limited flake size and random nucleation orientations grown on the inert substrates (*e.g.* SiO₂, mica)^{34,113}.

In this chapter, we demonstrate SBs in bilayer WS₂, which is a novel type of topological defect in TMD. Bilayer WS₂ flakes including AB/AC (also called as BA stacking) SBs were directly synthesized on graphene with large-size grain and lots of wrinkles for investigating the effect of wrinkle on WS₂ growth behavior rather than the GB effect. Wrinkles have been well known as strong nucleation sites with high reactivity and adsorption energy^{114,149}. Meanwhile, we demonstrate that the graphene wrinkles with a vertical height result in additional stress in epilayer WS₂. This study was performed using various surface analysis tools including SEM, DF-TEM, and AFM analysis. Because of the same formation energy between AB and AC stacking order, stacking fault energy between them is negligible; therefore, the balance between the SB energy¹⁴⁵ (*i.e.* misalignment and strain energy) and additional stress accumulated by the wrinkles in graphene substrate determine the spacing between Shockley partial dislocations (*i.e.* density of AB/AC SB). Moreover, we observed experimental result of out-of-plane buckling at AB/AC SBs for releasing in-plane strain energy using AFM tapping mode. The relaxation

of in-plane strain *via* out-of-plane buckling at an AB/AC SB makes re-expansion of the band gap to monolayer WS₂ in the bilayer matrix, reinforced by DFT calculations and EELS. Our results clarify the effect of template morphology on the nanostructure of epilayer using vdW epitaxy heterostructures. 1D AB/AC SBs with distinct optical and electronic properties could be engineered by controlling the morphology of template.

4.2. Experimental section

Fabrication of WS₂/Graphene Heterostructure including AB/AC SBs. Graphene with large-grain was grown on electrochemically polished Cu foils to remove surface oxide and surface impurities. The electropolished Cu films were intentionally oxidized at 200 °C for 30 min in ambient air to reduce the nucleation sites for large grain. After oxidation, the Cu films were inserted into a low-pressure CVD chamber and heated to 1,000 °C with flowing H₂ at 50 sccm; then, the temperature was maintained for 30 min. And then, CH₄ gas at 0.5 sccm was introduced into the CVD chamber for 2 hr as a carbon precursor to synthesize graphene. The as-grown large-grain graphene films were transferred to the central area of a bare SiO₂/Si substrate *via* conventional wet transfer method, which was utilized as a template for WS₂. WS₂ flakes were synthesized from 5-nm-thick WO₃ thin film (using an e-beam evaporator) and sulfur powder ($\geq 99.5\%$, Sigma Aldrich) as precursors. The transferred large-grain graphene substrate was placed face-to-face with a WO₃ film and detailed description could be found in Chapter 3.2 and reference⁸⁸.

Characterization. EELS data was acquired using Gatan Quantum 965 dual EELS system with energy resolution of 1.0 eV. A detailed description of SEM, AFM, C-AFM, and TEM analysis is mentioned in Chapter 3.2.

DFT Calculations. First-principles DFT calculations were performed to determine the atomic structure and properties of SBs in TMDs⁸⁸. We employed the Perdew–Burke–Ernzerhof functional¹²⁰ implemented in the Vienna ab initio simulation package¹⁵⁰. The supercell comprised ~400 atoms. The basis set contained plane waves whose kinetic energy was less than 300 eV. Grimme’s D3 correction was applied to correct for the dispersion interaction¹⁵¹. The atomic structures were relaxed until the residual forces were less than 0.02 eV/Å. The number of sampled k-points was increased until the density of states (DOS) converged. For sliding calculations, the cut-off energy was increased to 400 eV and the climbing-image nudged elastic band method¹⁵² was used to specify the sliding path.

4.3. Structural analysis of AB/AC SBs

4.3.1. AB/AC SBs in WS₂

SEM image illustrated in Figure 4.1a shows WS₂ directly grown on wrinkled graphene. The graphene wrinkles are produced due to the different thermal expansion coefficient (TEC) between Cu substrate and graphene and during transfer to the SiO₂ substrate before WS₂ growth. We used large-grain graphene to investigate the wrinkle effect rather than GB effect on growth behavior of WS₂. The darkest gray regions indicate bilayer and even multi-layer WS₂ flakes (indicated by blue arrows), and they are distributed along the graphene wrinkles (yellow arrows). The reason is that wrinkles, GBs, and other intrinsic defects in graphene act as nucleation centers for multi-layer TMDs with high chemical reactivity^{114,149}. WS₂ has 3-fold symmetry with alternating W and S elements, resulting in various stacking geometries based on interlayer rotation ($\theta = 60^\circ$ and 0°) and translation, as displayed in Figure 2.7. Because vertically heterogeneous pairs have favorable interaction¹⁴⁸, AA' (2H), AB and AC (3R) stacking arrangements are ground states with heterogeneous pairs and AB' and AC' stacking configurations are metastable and unstable with W–W and S–S homogeneous vertical pairs, respectively. Although AB and AC stackings show same configurations with mirror symmetry, we distinguish them for convenient explanation in this chapter and we focused on the AB/AC transition regions, called as SBs.

A low-magnification STEM image of multi-layer WS₂ flakes grown on wrinkle-rich graphene is shown in Figure 4.1b; the figure includes graphene wrinkles, denoted by a black-dotted line. Figure 4.1c and 4.1d represent DF-TEM images of the white square region in Figure 4.1b, acquired from the (01 $\bar{1}$ 0) and (2 $\bar{1}$ 10) diffraction spots, labeled $\Phi 1$ and $\Phi 2$ in the SAED pattern in inset of Figure 4.1d, respectively. DF-TEM image intensities for {01 $\bar{1}$ 0} (called as 1st order) and {2 $\bar{1}$ 10} (called as 2nd order) are known to roughly reflect stacking features and local numbers of layers, respectively, as mentioned in Chapter 2.3.1⁸⁷. Figure 4.1c shows different intensities in the WS₂ bilayer region, as shown in Figure 4.1d, indicating that there are different stacking geometries in bilayer region. The dark lines in Figure 4.1d exactly correspond to changes in stacking orders in Figure 4.1c, suggesting that there is a phase shift on these defect lines. For a detailed analysis of stacking orders, STEM simulation and Bloch-wave simulations are performed using Mac-TempasX software, as shown in Figure 4.2 and Figure 2.8, respectively. The experimental AR-STEM images in Figure 4.2a and 4.2b are obtained in the adjacent regions of bilayer WS₂ with different stacking configurations in Figure 4.1d, respectively, representing a Bernal-stacked structure with three different intensities. The carbon atoms in graphene are not displayed in the AR-STEM image due to the low atomic number of carbon (6) compared to the tungsten (74) and sulfur (16). The simulated AB/AC stacking image shows three different intensities for W+S, W, and S columns, which is consistent with experimental result, but AB and AC stacking orders could

not be exactly distinguished because Z-contrast image have same intensity between W+S and S+W atomic columns.

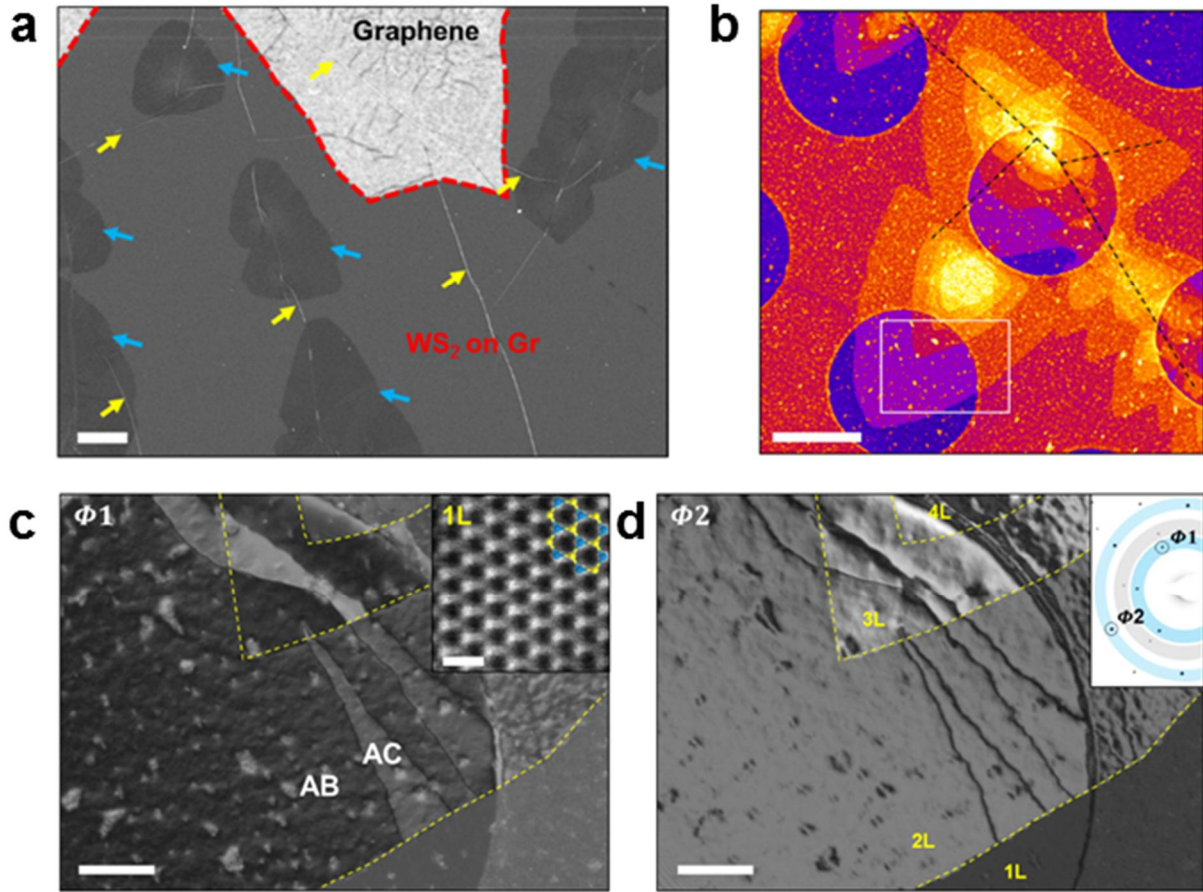
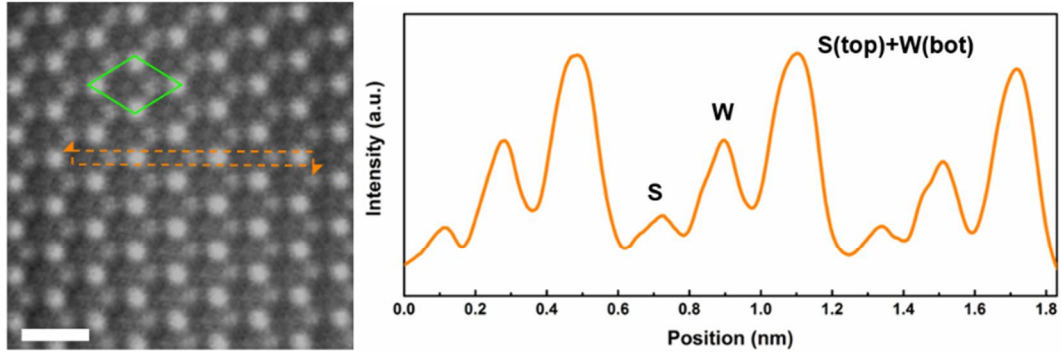
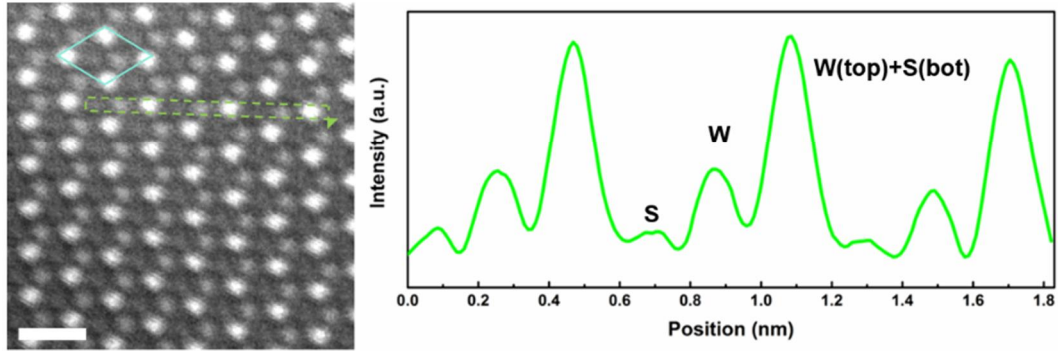


Figure 4.1. AB and AC stacking geometries in bilayer WS₂ grown on large grain and wrinkled graphene. (a) SE-SEM image of WS₂ directly synthesized on a graphene substrate. The bright white and dark gray (below the red dotted line) contrast regions are graphene only and WS₂/graphene heterostructure, respectively. Multi-layer WS₂ flakes (blue arrows) are grown along the graphene wrinkles (yellow arrows). (b) Low-magnification STEM image of multi-layer WS₂/graphene heterostructure. The black dashed lines represent graphene wrinkles. (c,d) DF-TEM images of white box region in (b) obtained from $(0\bar{1}10)$ and $(\bar{2}110)$ diffraction spots of WS₂, respectively, as indicated by circles in the inset in (d) showing the corresponding diffraction pattern. The scale bars in (a,b), (c,d) and inset of (c), 1 μ m, 200 nm, and 0.5 nm, respectively.

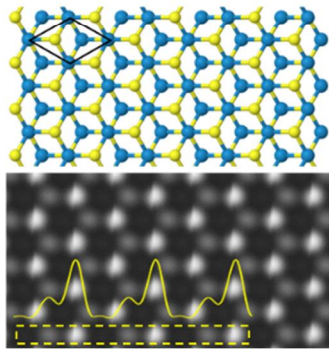
a AB stacking



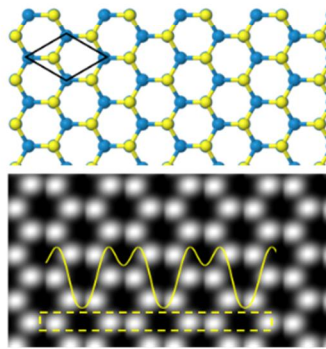
b AC stacking



c AB/AC Stacking



d AA' Stacking



e AC' Stacking

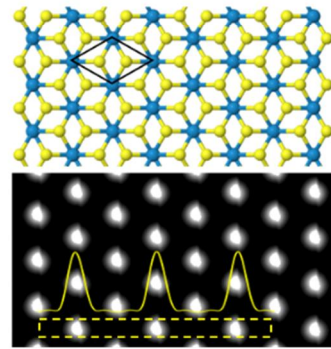


Figure 4.2. Experimental and simulated AR-STEM images of various stacking configurations in WS₂ bilayer. (a,b) Left panel: AR-STEM HAADF image of AB and AC stacked bilayer WS₂ on graphene, respectively. Right panel: Intensity profile with three different contrasts indicating S+W, W only, and S only columns in bilayer WS₂. (c-e) STEM image simulation of AB/AC, AA', and AB' stackings are performed to confirm the exact stacking orders. Only AB/AC stacking has three different contrasts, consistent with experimental results. Scale bar for (a,b), 0.5 nm.

To identify the exact AB or AC stacking geometry, we compared experimental DF-TEM images (Figure 4.1d) with the calculated relative intensity of diffraction pattern (depicted in Figure 2.8). The DF-TEM asymmetric intensity is reflected by asymmetric intensity of the diffraction spot³⁴ as I mentioned in Chapter 3.3.1. From this result, bright and dark regions in the bilayer WS₂ in Figure 4.1c labeled $\Phi 1$ is well matched with AC and AB configurations, respectively. Figure 4.3 exhibits the inversed contrast in the bilayer region in DF-TEM images obtained using adjacent $\{01\bar{1}0\}$ diffraction spots, and it is well correspond to the inversed diffraction intensity in Figure 2.8b and 2.8c for adjacent $\{01\bar{1}0\}$ peaks. In addition, the reflection intensities are drastic changes depending on the tilt angle (Figure 4.4), which is closely related with scattering condition and excitation error.

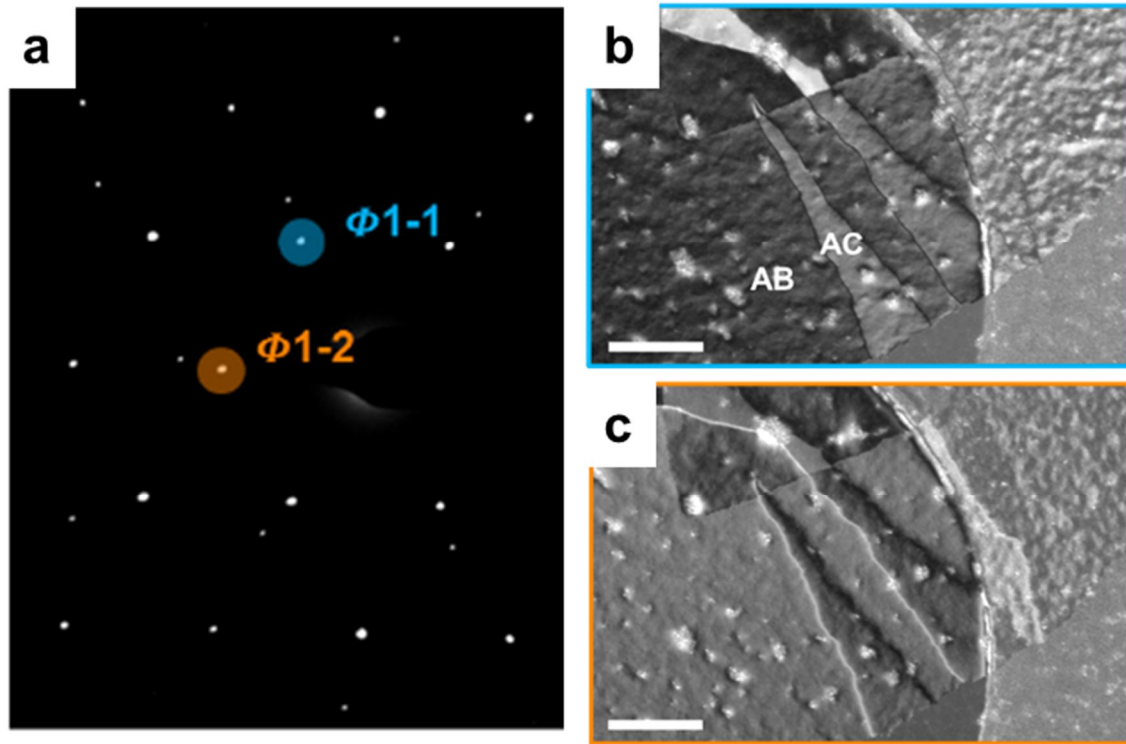


Figure 4.3. DF-TEM images obtained by adjacent diffraction spots, indicating stacking orders. (a) A SAED pattern obtained from epitaxially grown multi-layer WS₂ on graphene substrate. (b,c) DF-TEM images of WS₂/graphene heterostructure, acquired from adjacent 1st order diffraction spots $\Phi 1-1$ and $\Phi 1-2$, respectively, as shown by blue and orange circles in (a). DF-TEM contrast, which is determined from the interference of the atomic plane, is inverted between (b) and (c), suggesting a change in the stacking order with domain boundaries. According to Figure 2.8b and 2.8c, AC stacking is brighter at $\Phi 1-1$ than $\Phi 1-2$, whereas AB stacking is brighter at $\Phi 1-2$. Scale bar for (b,c), 200 nm.

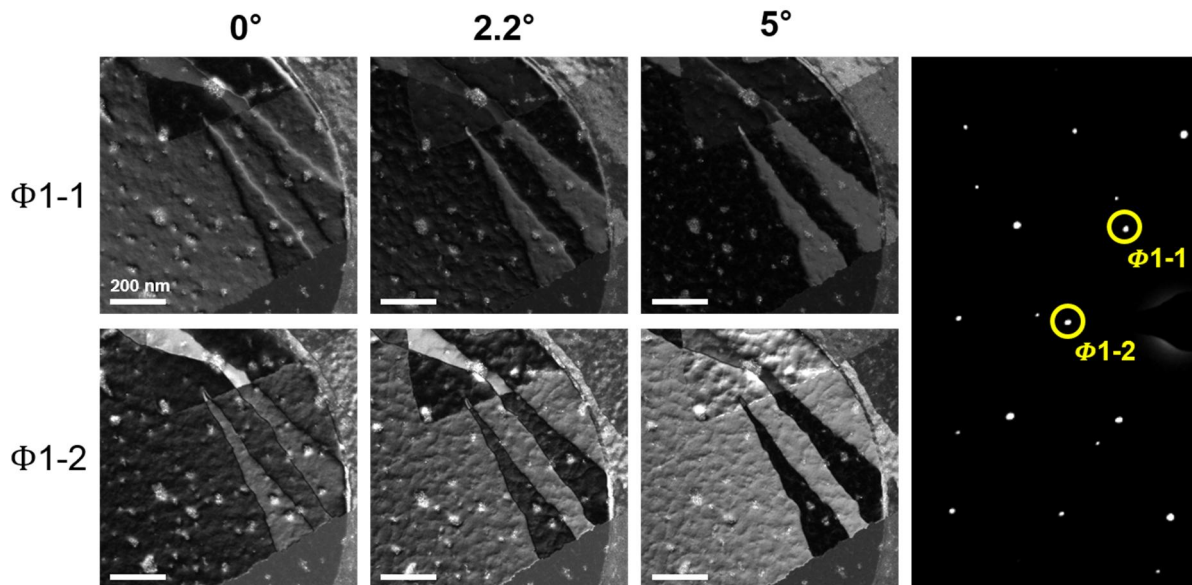


Figure 4.4. Experimental DF-TEM image series by specimen tilting. Contrast is inverted according to the tilt angle in $\Phi 1-1$ and $\Phi 1-2$.

Previous reports have suggested that interlayer sliding in bilayer graphene^{144,145} and bilayer h-BN⁸⁷ occurs easily with a small energy barrier, resulting in AB/AC SBs. The interlayer sliding energy profiles along the AC direction for bilayer WS₂ with $\theta = 0^\circ$ and 60° , are illustrated in Figure 4.5a. AB/AC and AA'/AB' has small sliding barriers of 21 and 27 meV/unit cell respectively, indicating that the sliding is energetically feasible. Therefore, it means a strong potential for forming SBs in bilayer WS₂ between ground stacking configurations.

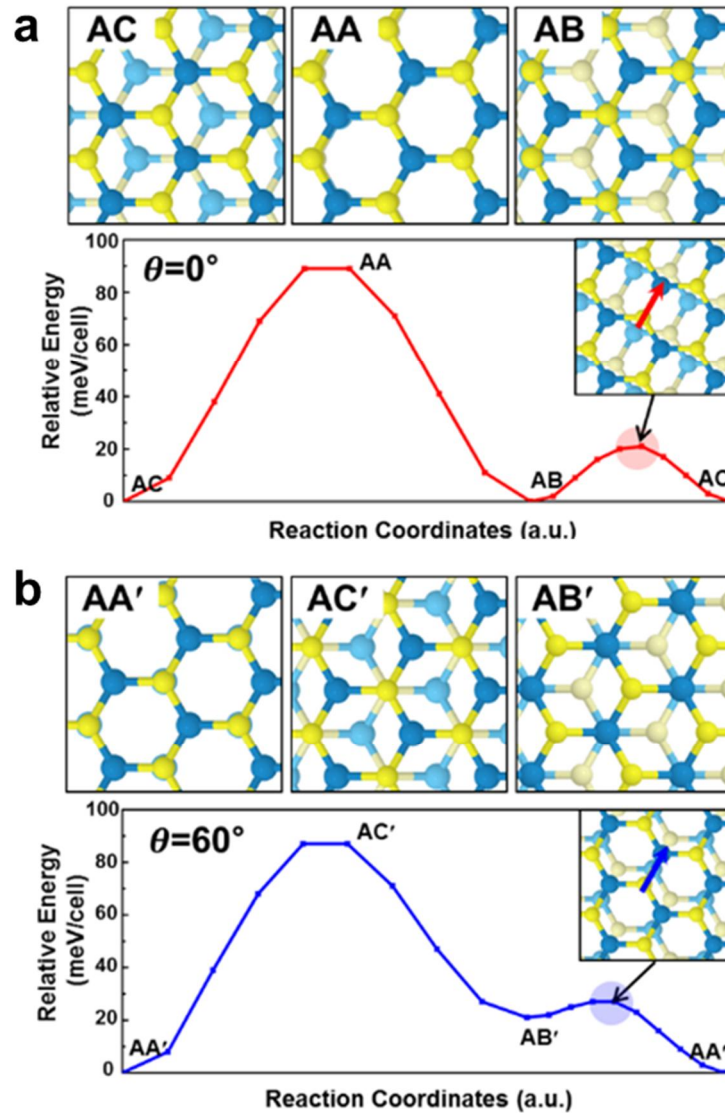


Figure 4.5. Energy profile along an AC direction for bilayer WS₂ with (a) $\theta = 0^\circ$ and (b) $\theta = 60^\circ$. The saddle point between AB and AC stackings has an energy barrier of ~ 21 meV/unit cell.

4.3.2. Burgers vector analysis and atomic structure in AB/AC SBs in WS₂

The DF-TEM images using $\{2\bar{1}10\}$ diffraction spots could be useful for the Burgers vector analysis of partial dislocations as displayed in Figure 4.6a and 4.6b. When we select the diffraction spot which is perpendicular to the the Burgers vector direction, the defect line is faint, due to no phase shift in the corresponding atomic plane⁸⁹. AB/AC SBs are induced by Shockley partial dislocations with Burgers vectors $b = (1/3) \langle 01\bar{1}0 \rangle$. A pair of Shockley partial dislocations forms a perfect basal dislocation along $\langle 2\bar{1}10 \rangle$ direction. Figure 4.6c and 4.6d show low-magnification and atomic resolution STEM images with dark contrast at SBs, because of the continuous relative shift caused by strain in one of the two layers¹⁴⁵. The AR-STEM image as shown in Figure 4.6d shows a diagonal line at the SB region (left and right corner) on the atomic scale. The SB directions are well matched with those in the atomic model in bottom panel of Figure 4.6d, which is modeled using DF-TEM based Burgers vector analysis.

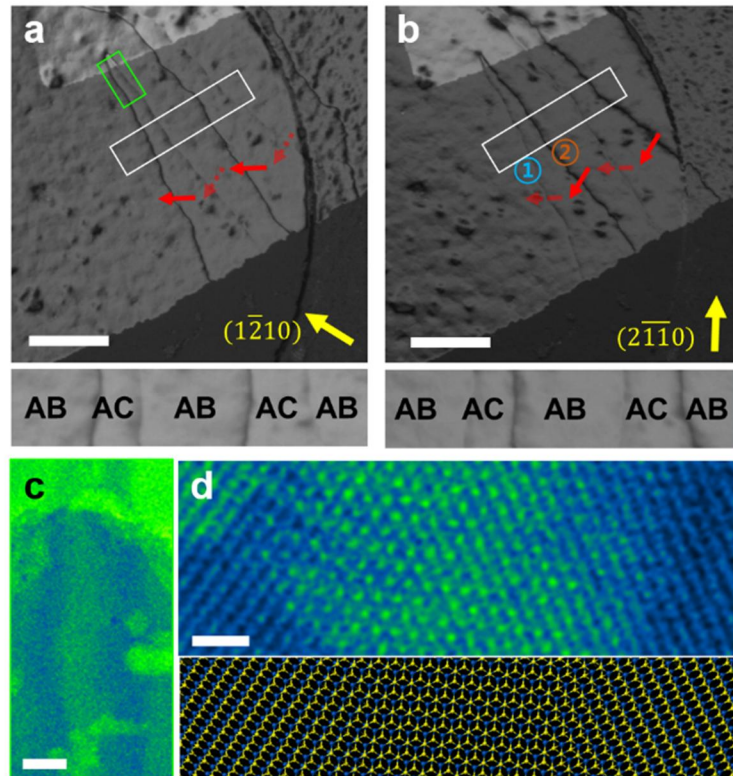


Figure 4.6. Analysis of Burgers vector using DF-TEM and corresponding atomic resolution images. (a,b) DF-TEM images obtained from $(1\bar{2}10)$ and $(2\bar{1}10)$ diffraction spots, respectively. The bottom panels (magnified images of white rectangular regions) indicate stacking orders based on the 1st order DF-TEM image. (c) Low-magnification STEM image with dark contrast at the stacking order transition region. (d) AR-STEM image of the green box region of (a) with corresponding atomic model (bottom panel). Scale bar for (a,b), (c), and (d), 200 nm, 10 nm, and 1 nm.

Figure 4.7a and 4.7b show the AR-TEM images of SBs denoted as ① and ② in Figure 4.6b, respectively, and insets are corresponding atomic models based on the Burgers vector analysis. AB and AC, collectively called as Bernal stacking, display regular 3-fold symmetric patterns (left insets), whereas the SB region shows a square-like irregular moiré pattern, as depicted in Figure 4.8. The direction of the square-like moiré pattern is closely related with the Burgers vector direction. Moreover, the AB/AC SB is non-continuous with several segments, as shown in Figure 4.7b at the nanoscale, which is perpendicular to the Burgers vector direction, indicating a tensile-soliton-related SB¹⁴⁵.

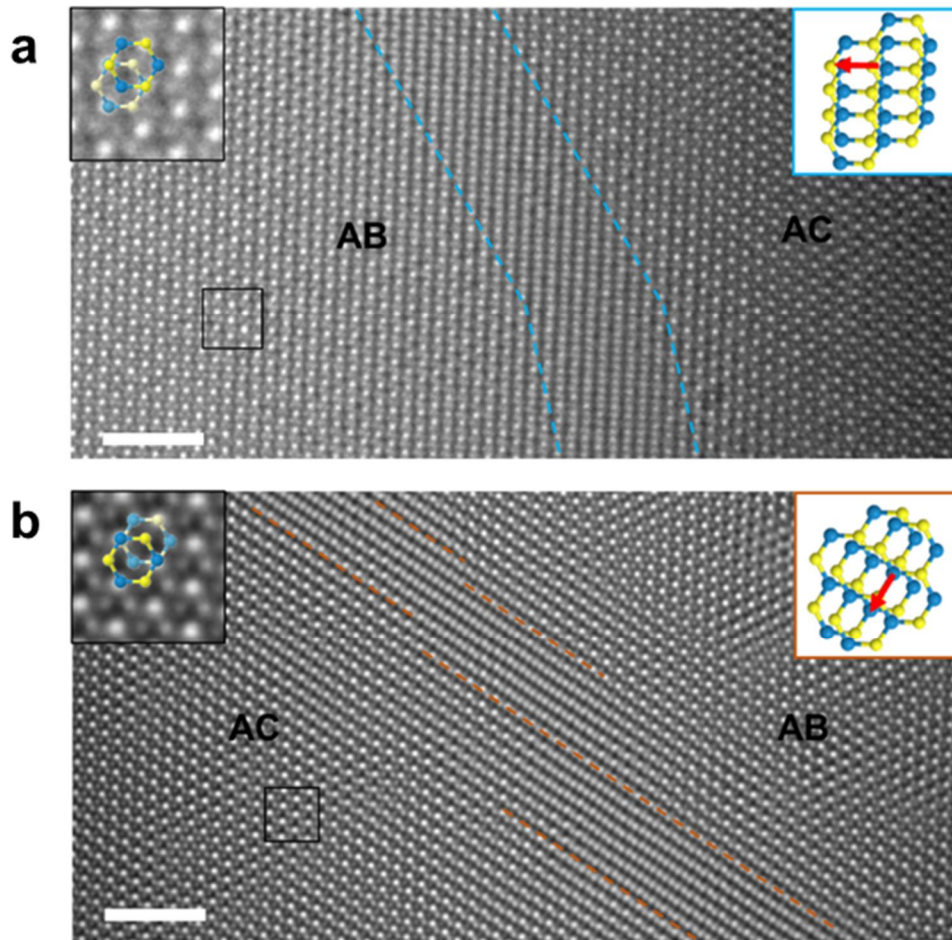
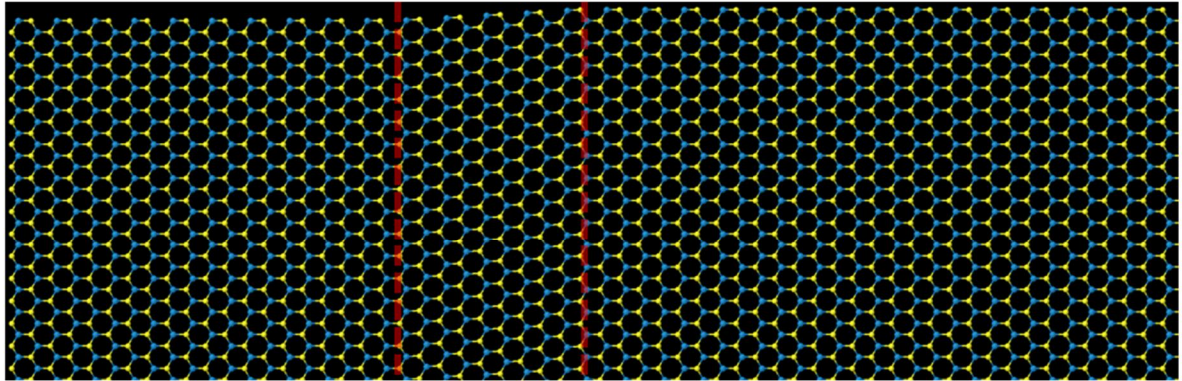


Figure 4.7. AR-TEM images of AB/AC SBs in bilayer WS₂. (a,b) AR-TEM images of SB ① and ②, respectively, denoted in Figure 4.6b. The AB/AC SB region shows square-like shape and have a different orientation according to the direction of Burgers vector. The experimentally observed configuration of the SB is well matched with the suggested atomic model (insets in right side). Red arrows mean Burgers vectors. Left insets show a Bernal-stacked bilayer WS₂. Scale bar, 2 nm.

a 1L (with partial dislocation)



b 2L (dislocation + pristine)

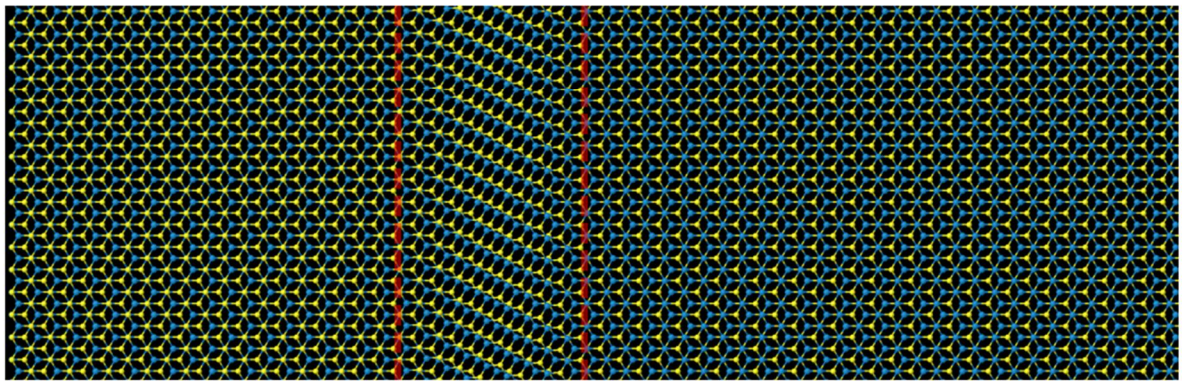


Figure 4.8. Moiré-like phenomena of AB/AC SBs. (a) Monolayer WS_2 including a partial dislocation, which can easily move along the basal plane. We could not identify the transition region clearly. (b) Bilayer WS_2 containing one layer with partial dislocation and a pristine layer. Based on moiré theory, the square-like SB region is clearly determined due to the phase shift relative to one another.

The relationship between the direction of Burgers vector and AB/AC SB direction is useful to identify the applied strain to the transition region of stacking orders (Figure 4.9). A SB induced by one Shockley partial dislocation indicated by red line is nearly perpendicular to the direction of Burgers vector, indicating a tensile-strain-related SB resulting in a tensile soliton¹⁴⁵. A SB from the other Shockley partial dislocation, denoted as blue line, is inclined obliquely to the direction of Burgers vector, indicating that it is related with a mixed tensile and shear strain. The averaged intensity profiles for tensile and mixed solitons are well matched with the results of previous research¹⁴⁵. Similar to earlier studies, which were researched using bilayer graphene^{144,145}, both tensile and shear strain are closely related with AB/AC SBs in WS₂. Of these, tensile strain related AB/AC SB is dominant because we predominantly observed the faceted tensile-soliton-related SBs as illustrated in Figure 4.7b.

In the meantime, the topological defects inside AA' stacking, shown in Figure 4.10, are mainly related to shear strain along the ZZ direction⁸⁷. These are induced by a faceted APB (mentioned in Chapter 3) in bottom layer of WS₂. The DF-TEM image in Figure 4.10c shows a double line in each topological defect represented by a red circle. Double line indicates a greater magnitude of dislocation with Burgers vector $b = 2 \cdot \langle \bar{2}110 \rangle$; this is longer than a , which represents the distance between adjacent W and S atoms in a WS₂ crystal. The transition region induced by partial dislocation is a strain-mediated defect without charge redistribution¹²³ (Figure 4.11), compared to the distinguishable contrast in APB defect region (insets in Figure 3.6).

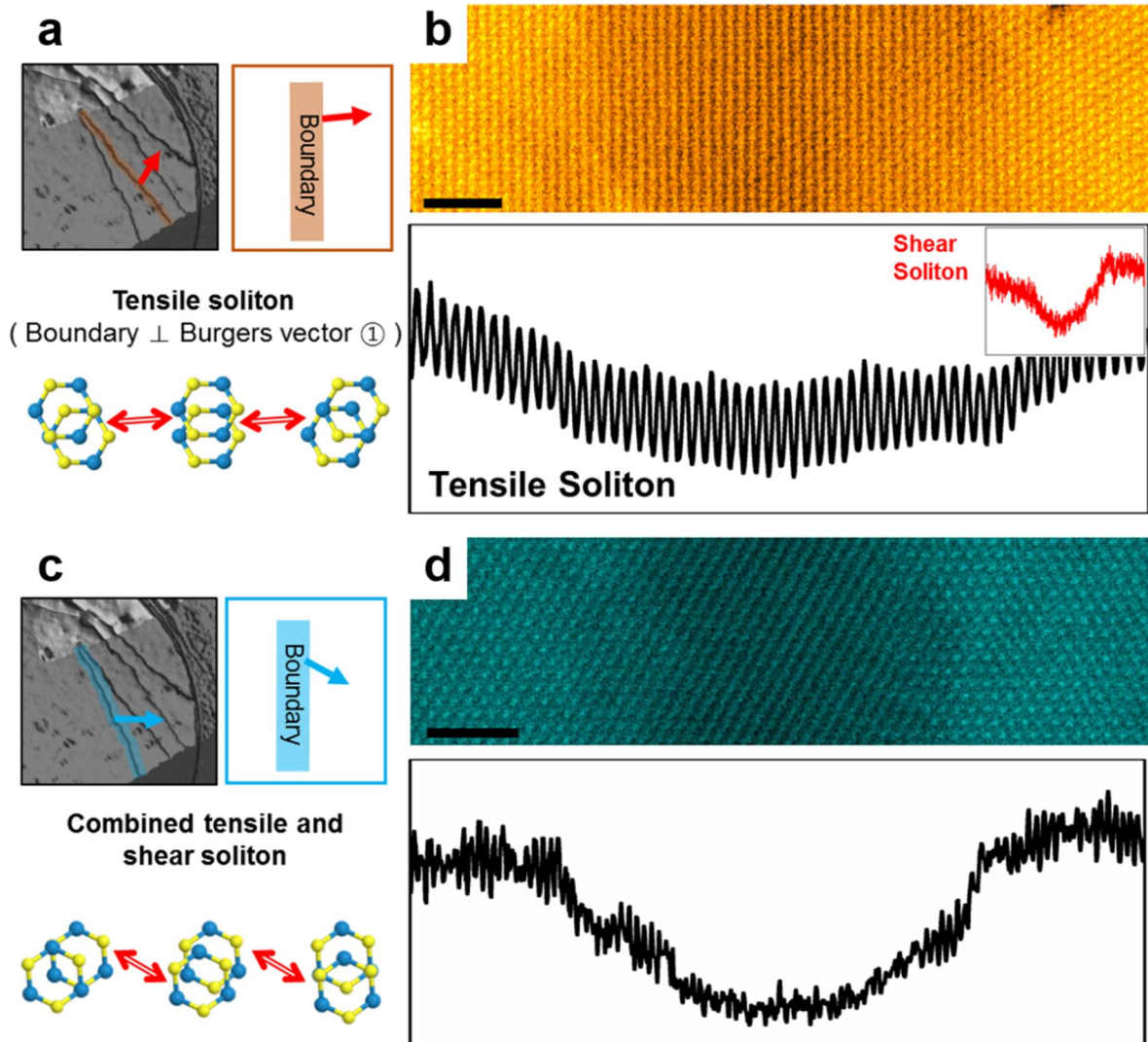


Figure 4.9. The relationship between SB orientation and Burgers vector direction. (a,b) Burgers vector direction is almost perpendicular to the boundary orientation, suggesting tensile-soliton-related defect. (b) AR-STEM image of a tensile-soliton-related AB/AC SB (upper panel) and an average intensity profile along the horizontal line (bottom panel). Our results correspond to the results of Ref⁴⁵. (c,d) The Burgers vector direction shows an inclined angle from the SB orientation, suggesting mixed tensile and shear-soliton-related defect. (d) AR-STEM image of the combined soliton (upper panel) and average line profile (bottom panel).

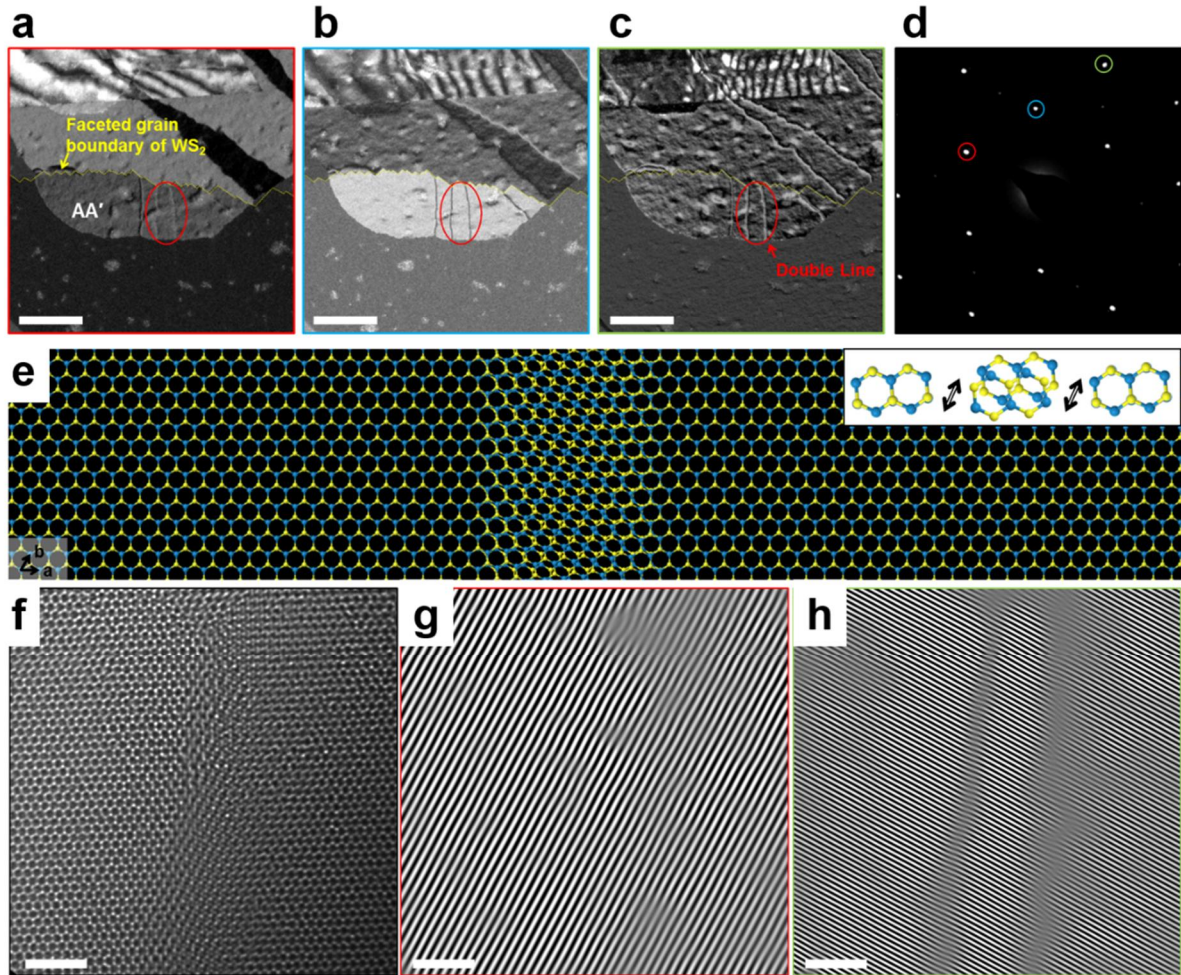


Figure 4.10. Topological defects inside AA' stacking orders in WS₂. (a-c) DF-TEM images obtained by selecting (a,b) 1st order and (c) 2nd order diffraction spots. The boundaries indicated by the red circles in (a-c) are analyzed using DF-TEM and AR-TEM images. The boundary is observed as a faint line in (a), a dark line in (b), and a double line in (c). Faint lines in (a) indicate that the displacement vector is perpendicular to the diffraction vectors. (d) SAED pattern of WS₂ and graphene heterostructures. (e) Suggested atomic model using the DF-TEM results. (f) AR-TEM image of topological defects inside AA' stacking order, indicated by the red circled region in (a-c). (g,h) Inverse FFT obtained by selecting the spots in FFT image corresponding to the red and green circled spots in SAED pattern, respectively. These AR-TEM images correspond to the DF-TEM images with a faint line in (a) and a double line in (c). Scale bar for (a-c) and (f-h) are 200 nm and 2 nm, respectively.

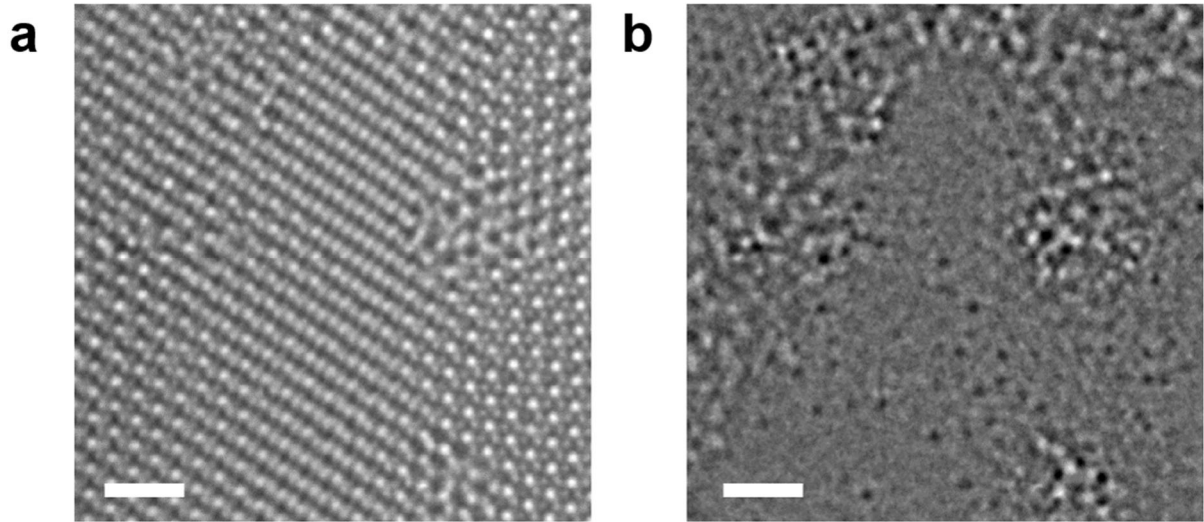


Figure 4.11. Strain-mediated AB/AC SB defect. (a) AR-TEM image of the SB region. (b) Inverse FFT image excluding WS_2 and graphene lattice information. There is no unusual contrast in the SB region, suggesting that it is only strain-mediated defect without abnormal charge redistribution. Scale bar is 1 nm.

4.4. Formation of AB/AC SBs on wrinkled graphene template

Figure 4.12a illustrates a false-colored BSE–SEM result reflecting the stacking configuration and SBs in multi-layer WS₂ flakes with a large field of view. The region with blue color represents monolayer WS₂, and the regions from purple to yellow (thicker) represent multi-layer WS₂ grains on graphene template. The band-like contrasts in multi-layer WS₂ in the BSE–SEM result represent different stacking configurations similar to the result of DF-TEM image due to the effects of electron channeling¹⁵³. Low magnification and raw SEM data of Figure 4.12a are displayed in Figure 4.13 with simultaneously obtained SE–SEM image, showing graphene wrinkles clearly. SBs, boundaries between different ground states, are distributed predominantly along the graphene wrinkles and exhibit disconnection across the wrinkles in graphene. Figure 4.14a shows that the formation of AB/AC SBs in bilayer WS₂ is strongly suppressed when the WS₂ flakes are directly deposited on a wrinkle-free template of graphene. It is well known that the interface between the synthesized layer and underlying substrate generally has large strains due to lattice mismatch¹⁵⁴, thermal mismatch^{155,156}, and other factors¹⁵⁶. Here, the lattice mismatch could be neglected, because the interface between WS₂ and graphene is interacted *via* weak vdW bonding. Therefore, previous studies demonstrated that the different TECs between the WS₂ epilayer and underlying graphene substrate during cooling process is a main origin of AB/AC SB formation¹⁵⁵. The higher TEC of WS₂ compared to that of graphene applies tensile strain in the WS₂ flakes¹¹. However, as depicted in Figure 4.14c, the density of AB/AC SB is zero in WS₂ grown on the wrinkle-free graphene, suggesting that only TEC-driven strain is not enough for AB/AC SB production. When WS₂ flakes are synthesized on the pristine graphene with some of wrinkles, SBs are only fabricated near the graphene wrinkles. Therefore, formation of SBs in WS₂ are profoundly related to morphological defects in graphene (*e.g.* wrinkles, folding).

The DF-TEM result in Figure 4.12b displays the terminated lateral growth of WS₂ adlayer due to the graphene wrinkle. Moreover, e-beam irradiation for 30 minutes at 80 kV results in discretely moved SBs, and the shape of which follows the orientation of WS₂ flake, suggesting soliton movement as shown in Figure 4.12c,d. However, movement of dislocations does not exceed the graphene wrinkle (overlaid as a green line) under e-beam irradiation, which imparts substantial energy. These experimental observations suggest that wrinkles in graphene substrate act as not only nucleation sites for the multi-layer growth of WS₂ but also vertical barriers with a vertical height around ~ 1.2 nm, as depicted in Figure 4.12e. It suggests that additional stress can be applied in addition to the stress caused by TEC-related strains.

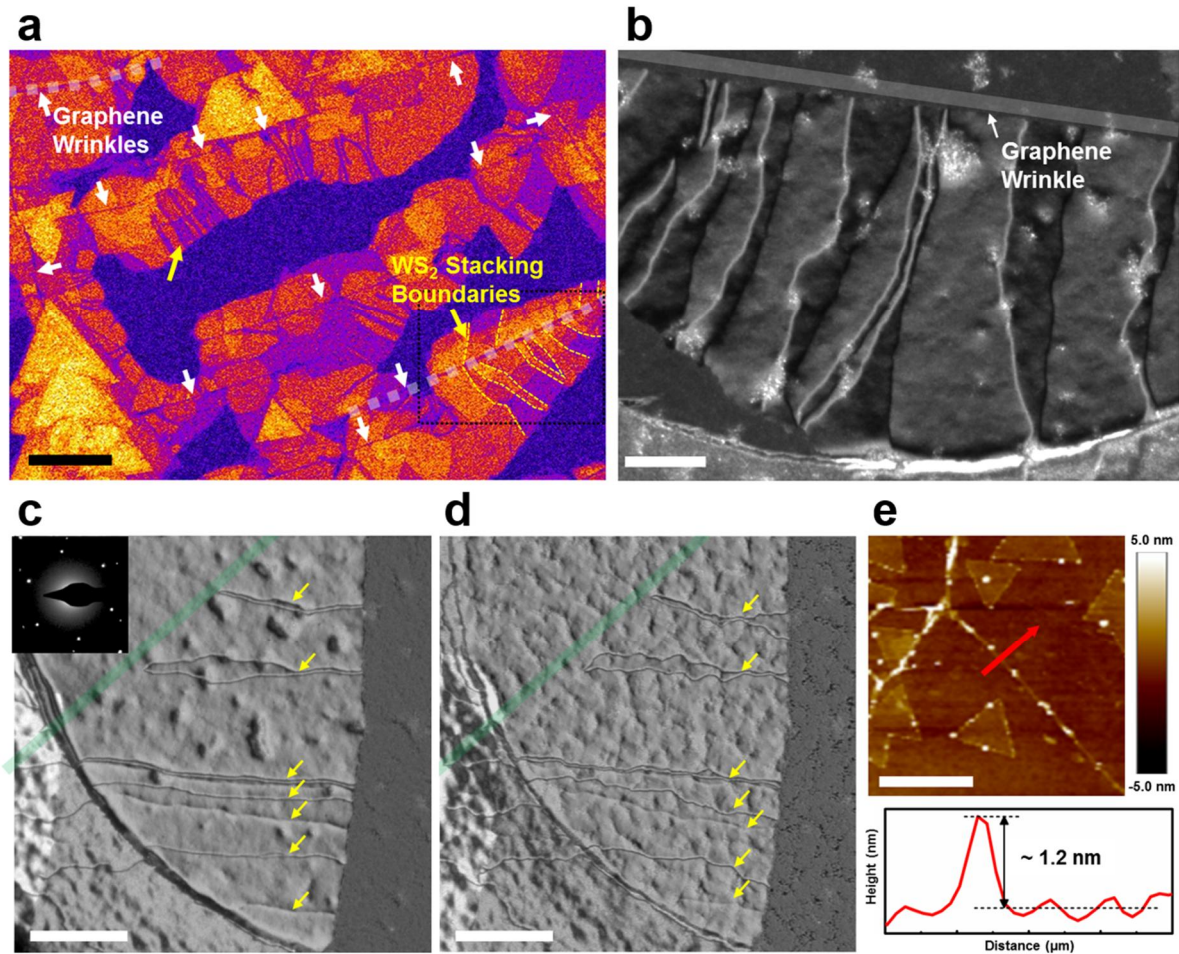


Figure 4.12. Graphene wrinkles act as vertical barriers to WS₂ epilayer. (a) BSE-SEM image of WS₂ with numerous SBs on wrinkled graphene. The distribution of SBs (yellow dotted lines) are along the graphene wrinkles (white dotted lines), suggesting that graphene wrinkles are closely related with formation of SBs. (b) DF-TEM image of bilayer WS₂ including AB/AC SBs. The growth of bilayer WS₂ is prevented beyond the graphene wrinkle (white line). (c,d) DF-TEM image of a SB (yellow arrows): (c) initially and (d) after e-beam irradiation for 30 minutes. The SBs are discretely mobile under the e-beam energy source; however, they do not pass graphene wrinkle (green line). Discrete motion suggests the particle-related motion (*i.e.* soliton). Scale bar is 200 nm. (e) AFM height image (top) and line profile (bottom) of graphene wrinkles, with a vertical height of ~1 nm. Scale bar for (a), (b), (c,d), and (e) are 1 μ m, 100 nm, 200 nm, and 0.5 μ m, respectively.

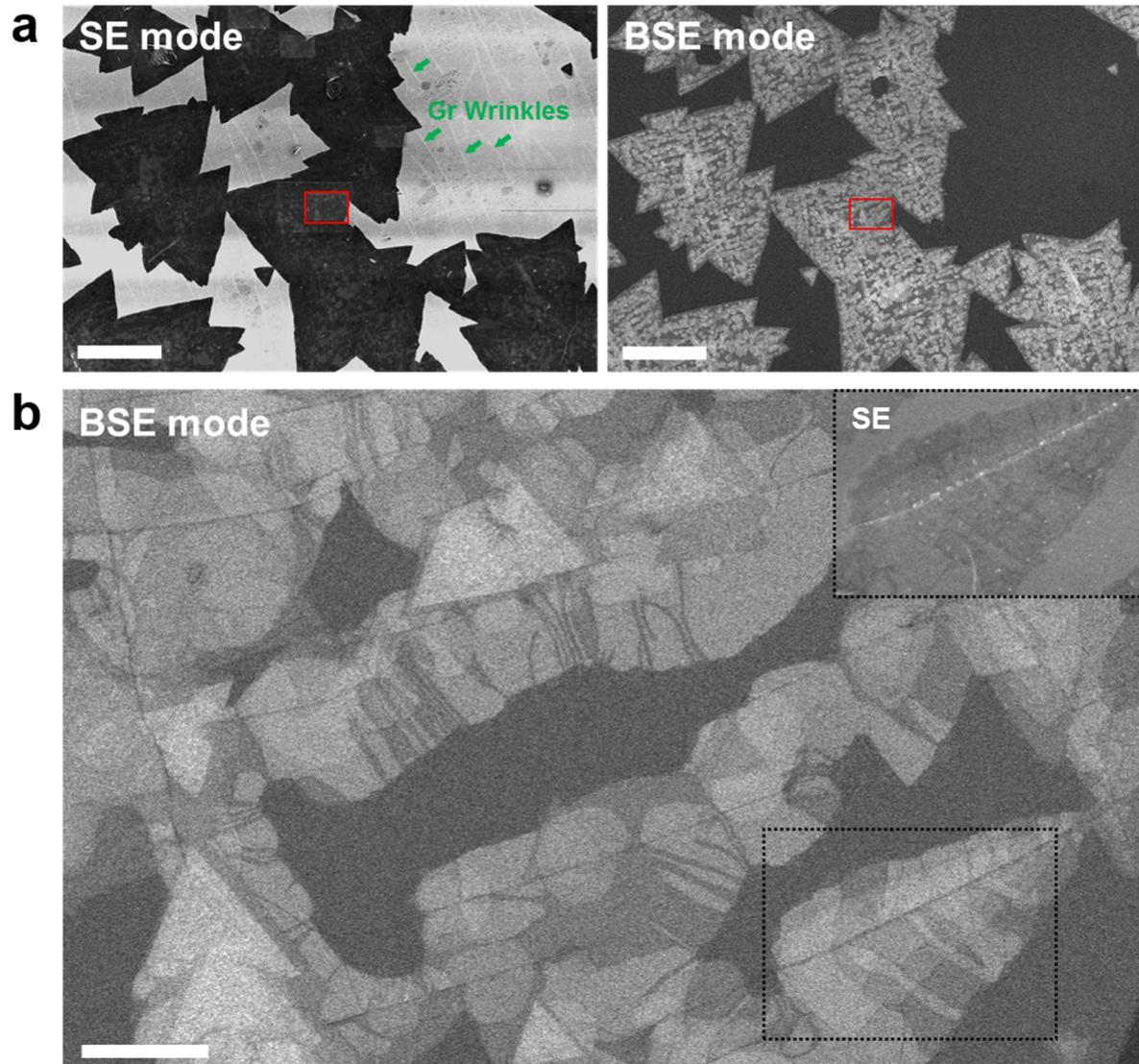


Figure 4.13. Distribution of SBs in WS₂/wrinkle rich graphene heterostructure. (a) Simultaneously obtained SE and BSE mode SEM images with low magnification. (b) Magnified view of red region in (a). False-colored image is displayed in Figure 4.12a. Black dotted square region coincides with the black square region in Figure 4.12a.

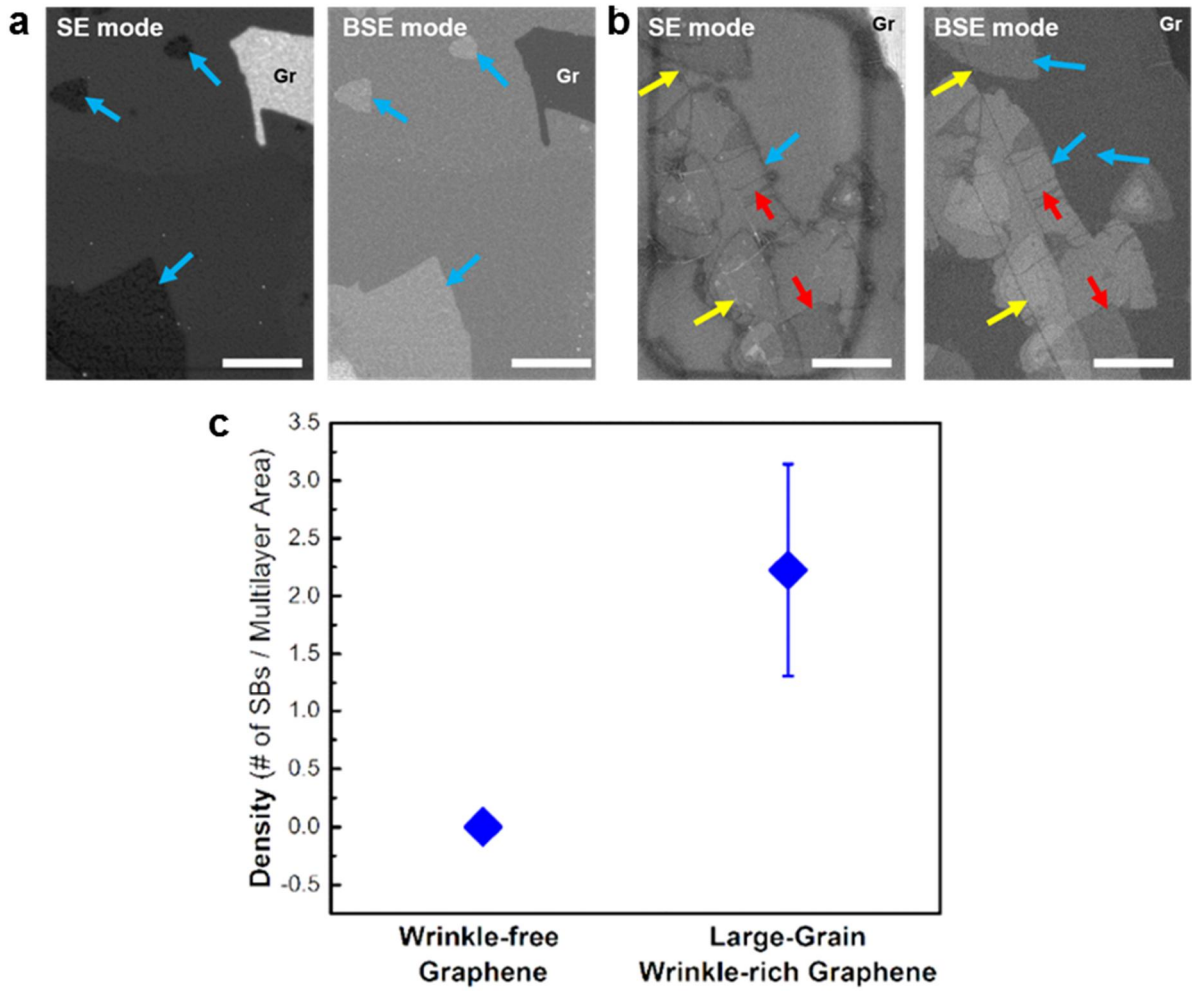


Figure 4.14. Density of SBs in epitaxially grown WS₂ grown on (a) flat graphene and (b) wrinkled graphene. Graphene wrinkles are indicated by yellow arrows. Bilayer WS₂ films are indicated by blue arrows. For wrinkle-rich graphene, bilayer WS₂ growth is significantly enhanced due to high chemical potential and induces SBs (red arrows) with confined partial dislocations. (c) Statistics of SB density grown on a wrinkle-free and a wrinkle-rich graphene, respectively.

Graphene wrinkles with vertical height in graphene are barriers for growth and migration of atoms in WS₂ flakes. Figure 4.15a-c and Figure 4.15d-f show different densities of AB/AC SBs in bilayer WS₂. In other words, Figure 4.15a-c shows high density of SBs, whereas Figure 4.15d-f shows low density of SBs. The direction of perfect basal dislocation along $\{2\bar{1}10\}$ direction, combined with a pair of partial dislocations, is denoted by the dashed arrows in Figure 4.15b and 4.15e. Figure 4.15c and 4.15f show graphene wrinkle directions identified by selecting one of the graphene diffraction spots, and the observed graphene wrinkles exhibits as folded wrinkles. For the case of high density AB/AC SBs, displayed in Figure 4.13a-c, the graphene wrinkle direction is almost perpendicular to the perfect basal dislocation direction; while is more parallel for low density of AB/AC SBs, illustrated in Figure 4.13d-f. Based on these results, Figure 4.15g schematizes the relationship between the direction of dislocation applied in WS₂ flakes and the graphene wrinkle direction. The plot showing the relationship between partial dislocation density (*i.e.* density of AB/AC SBs) and the absolute value of the angle between graphene wrinkle direction and perfect basal dislocation direction is displayed in Figure 4.15h. The partial dislocation density is strongly dependent on the magnitude of the angle. As I mentioned before, the splitting of partial dislocations is closely linked to the balance between attractive forces (related to the minimization of the stacking fault energy), and repulsive forces (related to the strain energy reduction)⁸⁹. For bilayer WS₂, the saddle-point (transition region) shown in the insets of Figure 4.5a might exhibit strain and misalignment energies¹⁴⁵, whereas there is no energy difference between the AB and AC stacking orders. Generally, it is well known that a perfect basal dislocation is dissociated for reducing dislocation energy, according to the Frank's rule ($b_{\text{partial}1}^2 + b_{\text{partial}2}^2 < b_{\text{perfect}}^2$)¹⁵⁷. Both cases of high and low densities of AB/AC SBs show the negligible difference in strain and misalignment energy due to the same sliding barrier, similar SB widths, and same magnitude of burgers vector. Thus, for explaining different partial dislocation densities, another external term, which is driven from the non-flat morphology of graphene wrinkles, should be considered (*e.g.* the non-negligible friction)¹¹. Previous research demonstrated that graphene wrinkles have anisotropic friction with anisotropic bending stiffness depending on the scanning direction of the AFM tip, implying that they could impart significant stress to the WS₂ epilayer¹⁵⁸. In other words, friction coefficient of graphene wrinkle depends on the angle between scanning direction and graphene wrinkle direction¹⁵⁹. For the case of high density of AB/AC SBs, perfect basal dislocation direction is almost perpendicular to the graphene wrinkle direction, resulting in high friction^{158,159}. Graphene wrinkle as vertical barrier hinders the motion of atoms and prevents its growth (Figure 4.12b-d), resulting in strain-induced deformed configurations. Thus, the formation of partial dislocations with high density is desirable to release highly accumulated energy state¹⁵⁷. However, when the perfect basal dislocation direction is nearly parallel to the wrinkles, it allows atoms to move in that direction and deformation resistance is high¹⁵⁸. Thus, low accumulated stress is released with a low density of partial dislocations. These results show that the interfaces in heterostructure considerably affect structure of epilayer, such as 1D SBs.

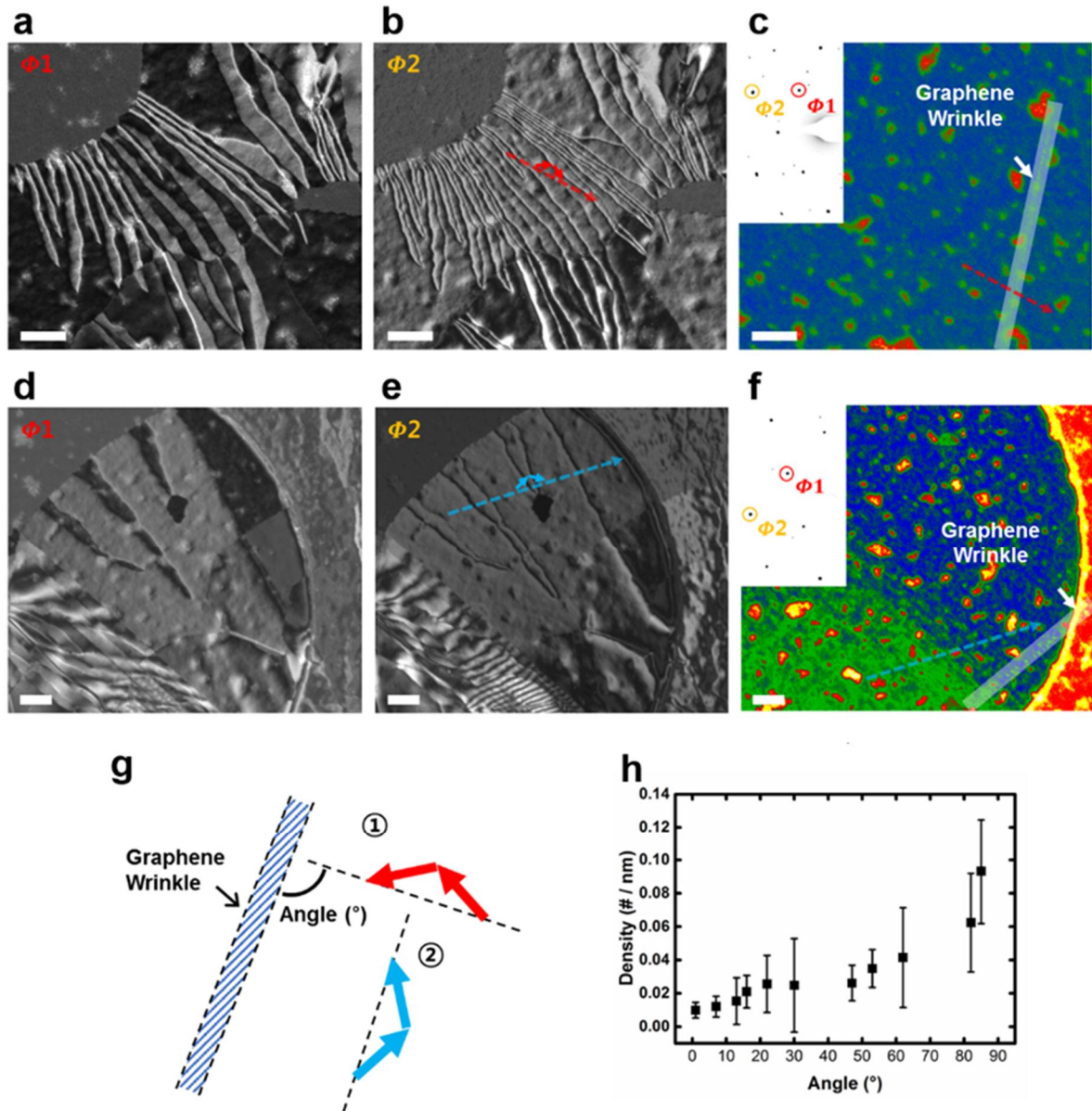


Figure 4.15. Different density of AB/AC SBs from the anisotropic friction of graphene wrinkles. (a-c) High density of partial dislocations. The direction of perfect basal dislocation direction is identified as 4 o'clock direction using 1st and 2nd DF-TEM analysis. (c) DF-TEM image from a graphene diffraction spot shows a brighter line at the right corner, overlaid by a white line, indicating folded wrinkle in the graphene. The perfect dislocation direction is almost perpendicular to the graphene wrinkle direction. (d-f) Low density of partial dislocations. The perfect basal dislocation direction is rather parallel to graphene wrinkle direction. (g) Schematic of the relationship between perfect dislocation direction and graphene wrinkle direction. (h) Partial dislocation density as a function of the absolute value of the angle between the graphene wrinkles and the perfect dislocation direction. Scale bar is 100 nm.

4.5. Buckling of AB/AC SBs and their electronic property

In this section, we discuss the electronic properties of AB/AC SBs in WS₂. Numerous previous reports predicted that a SB has a buckled structure to release the in-plane strain energy from a dislocation^{89,144,160}. Additionally, AB/AC SBs' discontinuous movement under the e-beam source (Figure 4.12d) could be explained by soliton pinning phenomena from the out-of-plane buckled structure¹⁴⁵. However, experimental results of buckled SB structure and its exact height has not yet been determined. Figure 4.16 shows the buckling of AB/AC SBs with a height of 1 nm using the AFM tapping mode, which is well consistent with the estimated value⁸⁹. The SBs in Figure 4.16 exist perpendicular to the graphene wrinkles and do not pass it, corresponding to the BSE–SEM image in Figure 4.12a. Combined with calculated result for checking the stable defect configuration, we can conclude that out-of-plane buckled structures are energetically more favorable and the calculated energy values according to the SB width are summarized in Table 4.1.

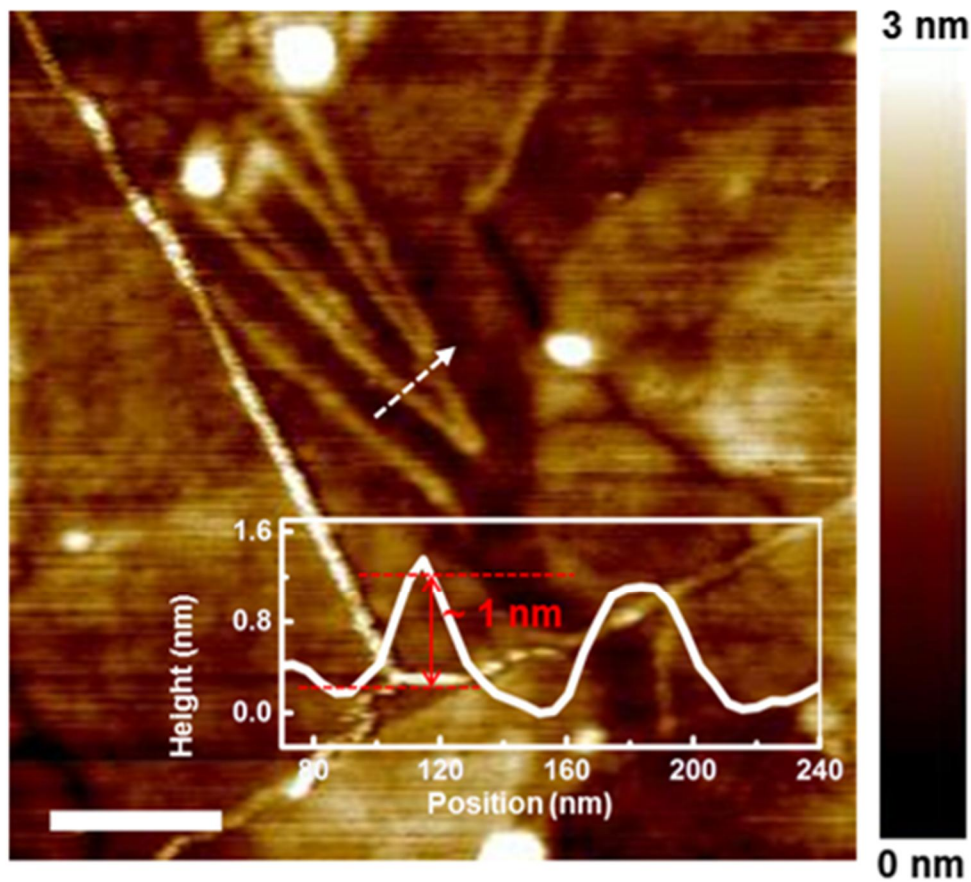


Figure 4.16. Out-of-plane buckled structures of WS₂ SBs. Height image obtained using tapping mode of AFM, showing a buckling structure at a SB with vertical height. Scale bar is 0.2 μ m.

width [Å]	Relative energy [eV / nm]	
	not buckled	buckled
16.4	52.9	35.6
21.8	40.4	25.4
27.3	33.1	20.7
32.7	28.5	18.3

Table 4.1. The relative energies of SBs without and with buckling. The relative energy is zero for the pristine bilayer WS₂.

EEL spectra have proved to be a suitable tool for measuring optical and electrical excitations with a high spatial resolution¹⁶¹. Figure 4.17a shows EELS line spectra across the AB/AC SB. When the number of layers decreases, the $\pi + \sigma$ plasmon peak near 20 eV shifts towards lower energy¹⁶². Compared to pristine bilayer WS₂, $\pi + \sigma$ plasmon peak at AB/AC SB is significantly redshifted and similar to that in monolayer WS₂ region (Figure 4.17c), indicating that AB/AC SBs in WS₂ behave like monolayer WS₂. To investigate a detailed electronic structure of AB/AC SB, DFT calculations were performed for the DOS and band gap (Figure 4.18a and 4.18b). The width of AB/AC SB determines the in-plane strain because the Burgers vectors have the same magnitude. In the AB/AC SB with 3.3 nm width in Figure 4.18b, the band gap shrinks for a SB with non-buckled (*i.e.* flat) morphology due to the dislocation-driven significant in-plane strain at the SB. However, the SB with buckled structure re-expands the band gap due to in-plane strain relaxation through out-of-plane buckling. Interestingly, the band gap for a buckled SB is similar to the band gap of a monolayer WS₂ flake due to the reduced S-S interlayer interactions *via* buckling¹⁶³. Likewise, for the narrower AB/AC SB with 1.6 nm width in Figure 4.18a, in-plane strain at the SB is substantial, leading to a strongly reduced band gap for a flat structure. However, buckling restores the band gap similar to that of the dislocation-free bilayer WS₂. We predicted that the band gap for the 1.6-nm-wide AB/AC SB should expand to match the band gap of monolayer WS₂, in terms of in-plane relaxation and reduced interlayer coupling through buckling, similar to the case of 3.3-nm-wide SB. However, the band gap restoration is relaxed due to significant curvature in the buckled region¹⁶⁴. Earlier publications reported that these bending structures with disrupted vdW interactions induce considerably reduced conductance with scattering-driven reduced electron transmission^{146,165}. To understand the detailed transport mechanism at the SBs, further research should be required to obtain detailed experimental observations of optoelectronic properties at AB/AC SBs and to establish correlations between the reduced transport and density of SBs.

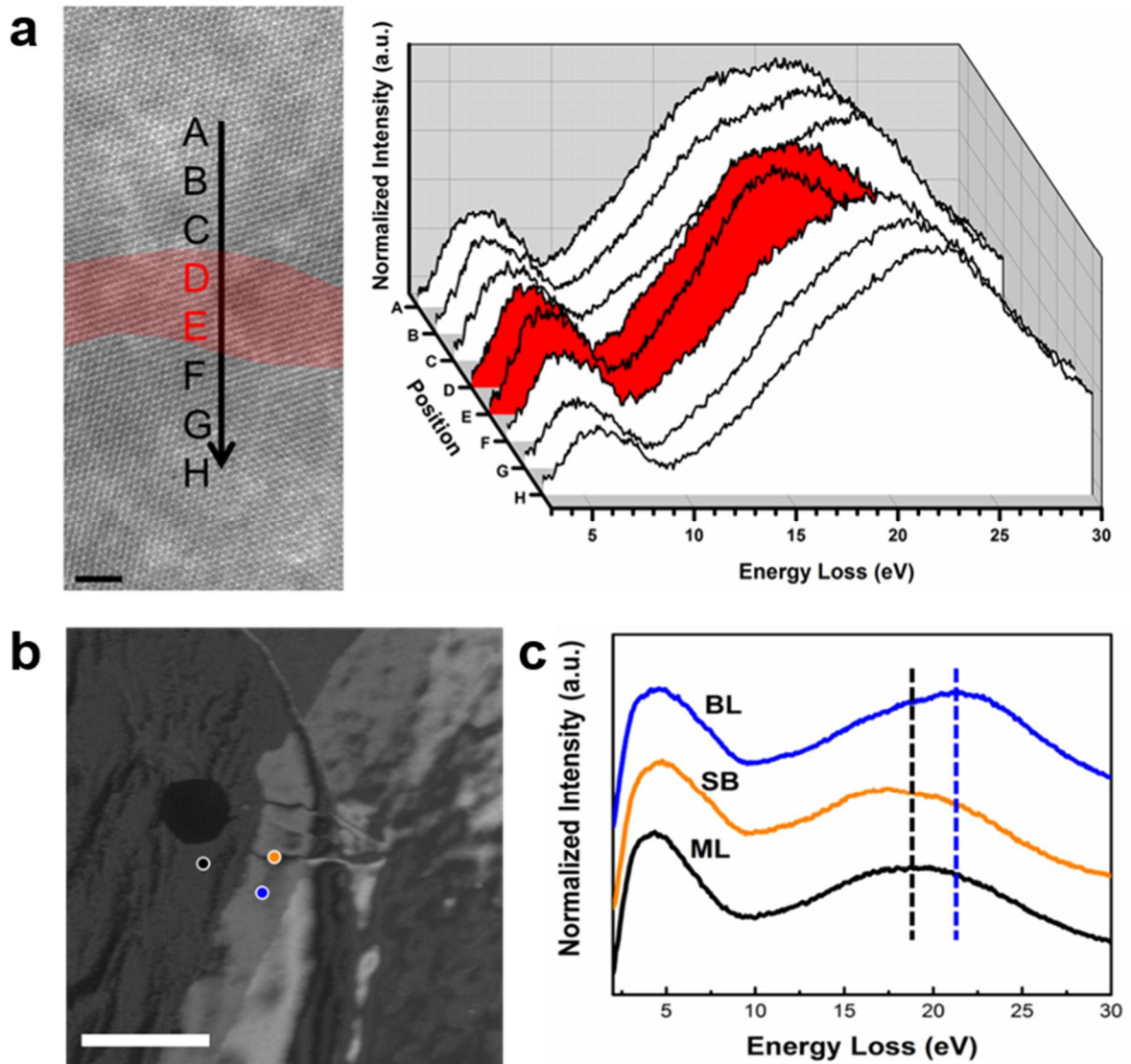


Figure 4.17. EEL spectra analysis for investigating electronic property of AB/AC SBs in bilayer WS_2 . (a) EELS line profile across the AB/AC SB in bilayer WS_2 . The red shaded regions denoted in AR-STEM image (left) and EELS spectra (right) indicate AB/AC SB regions. $\pi + \sigma$ plasmon peak is significantly redshifted at SB. (b-c) EEL spectra of monolayer (black), SB (orange), and AB or AC stacked bilayer WS_2 (blue). All EEL spectra are deconvoluted by zero-loss peak subtraction. Although SB has bilayer structure, it behaves like monolayer WS_2 due to the reduced interlayer coupling from buckling. Scale bar for (a) and (b), 2 nm and 200 nm, respectively.

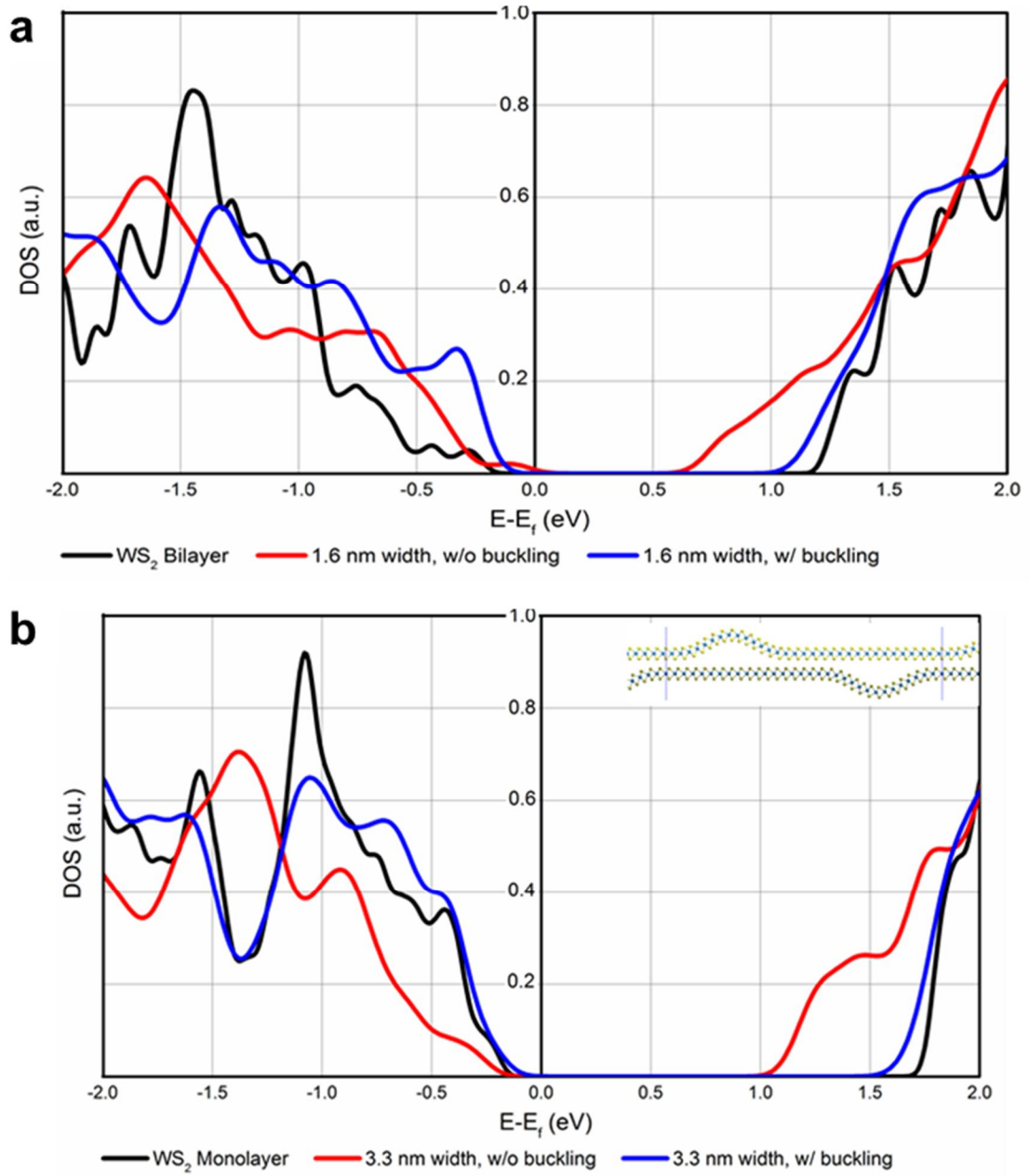


Figure 4.18. Effect of in-plane strain on the electronic properties using DFT calculation. (a-b) DOS calculation results of bilayer WS₂ including (a) 1.6 nm width of SB and (b) 3.3 nm width of SB. Blue and red lines indicate buckled and flat morphology of AB/AC SB. They are compared to (a) pristine bilayer WS₂ and (b) single-layer WS₂ (represented as black line).

4.6. Conclusion and outlook

AB/AC SBs have been received widespread interests due to their novel properties, particularly in the case of bilayer graphene. For example, AB/AC SBs in bilayer graphene could act as valley-polarized transport channels¹⁶⁶ and have linear magnetoresistance¹⁶⁷. Study on the origin and formation mechanism of AB/AC SB is strongly required for further controllable fabrication and property engineering, but they have not been systematically established.

Herein, we observed AB/AC SBs in multilayer WS₂, which were driven by morphological defects (*e.g.* wrinkle) in a graphene substrate. Our results demonstrate that graphene wrinkles act not only as nucleation sites for multilayer growth with high chemical reactivity but also as vertical barriers with non-negligible vertical height, leading to stress accumulation in WS₂ flakes during heterostructure growth. Non-flat interface driven anisotropic friction of graphene wrinkle facilitates the formation of a novel AB/AC SB defect in TMDs. Additionally, we demonstrate that in-plane strain from the partial dislocation leads to an out-of-plane buckled AB/AC SB structure to release in-plane strain and it restores the band gap into the pristine bilayer and even monolayer WS₂.

Our observation indicates that the modification of electronic and optical properties with extended 1D defects can be controlled by adjusting the morphology of the underlying template (*e.g.* graphene wrinkles) and it increases the potential for use in various applications with unique features. We proposed that a monolayer-like behavior at AB/AC SB with reduced interlayer coupling, but further study should be necessary to unravel and discover the other novel transport behavior and optoelectronic properties at AB/AC SBs in TMDs, and it could facilitate to expand the scope of TMD-based applications.

Recently, P. Schweizer *et al.* reported a dislocation node¹⁶⁸, which is the intersection between AB/AC and AC/AB SB. They proposed that a perfect out-of-plane dislocation in the first layer induces partial dislocations during the growth of second layer to minimize the energy of the system. In detail, upon growth of the second layer, the out-of-plane dislocation line turns perpendicular to the original direction. To minimize energy, the dislocation splits into two partial dislocations¹⁶⁸. In this chapter, we claimed that the graphene wrinkles act as vertical barriers with 1 nm height, applying significant stress to the epilayer WS₂. It generates lots of defects such as perfect dislocations. From this result, we can estimate that the perfect dislocation in WS₂ first layer makes dislocation splitting into two partial dislocations in WS₂ second layer for reducing energy. The point where presenting perfect out-of-plane dislocation is a dislocation node. The figure below (Figure 4.19) shows that atomic resolution image of a dislocation node. There is a different contrast at the dislocation node in the image after removing WS₂ and graphene lattice information. It indicates existence of defects at the dislocation node. For the detailed defect and structure analysis at dislocation node, further work should be required.

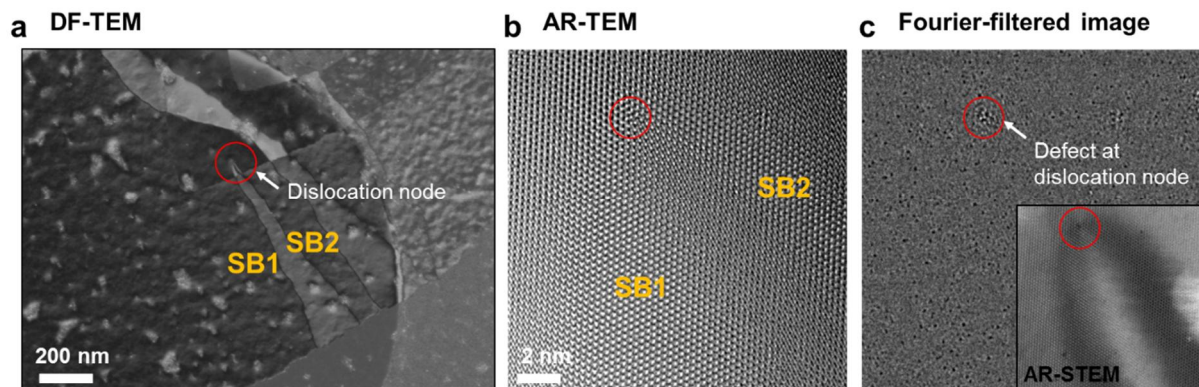


Figure 4.19. Dislocation node, which is intersection of two AB/AC SBs. DF-TEM, AR-TEM, and corresponding Fourier-filtered image at dislocation node, which is obtained by excluding graphene and WS₂ lattice information. Scale bar for (a) and (b), 200 nm and 2 nm, respectively.

Chapter 5. Edge rich multilayered TMDs grown on the nanocrystalline graphene

5.1. TMDs grown on the graphene defects

Defects in the template layer have a huge influence on the nucleation and growth behavior of heterostructures, because the dangling bonds at defective sites (*e.g.* vacancy, wrinkles, and GBs) are more reactive with high chemical reactivity¹¹⁴. Despite their chance to produce heterostructure with novel property using the defects in the template layer, previous theoretical and experimental studies have considered only the defect-free templates¹⁶⁹.

Previously, we demonstrated the impact of the defects in template layer on the heterostructure property using directly synthesized WS₂ on polycrystalline graphene¹³. There are two types of WS₂/graphene heterostructure, (1) WS₂ nucleated at the graphene GBs (D-WS₂) and (2) WS₂ nucleated on the graphene basal plane (B-WS₂). Although both types of WS₂ have the same atomic structure, there are discrepancy in thermal stability and electrical properties between two cases. For example, D-WS₂ flakes shows effective charge transport at the interface, resulting in lower contact resistance compared to the B-WS₂ flakes, because W atomic bridges between WS₂ and graphene layer are introduced at defect sites of the template inducing formation of covalent bond at the interface¹³.

Herein, we demonstrate the WSe₂ flakes grown on graphene with enormous defective sites as an extension of previous research. We synthesized WSe₂ flakes on nanocrystalline graphene (ncG), which has around 70 nm² of grain size, and compared with those on SiO₂/Si substrate under the same growth condition. Interestingly, while WSe₂ flakes grown on the SiO₂/Si or pristine graphene exhibit monolayer-limited thickness based on the lateral growth, WSe₂ flakes grown on the ncG film show edge rich multilayered structure due to high nucleation density at defect sites. One cluster has a single orientation with 3R stacking configuration with a vertical height of 12 nm and it has large amount of Se-terminated edge, suggesting that the flakes are grown under the Se-rich growth condition. Confined Se-terminated edge could be applicable to the enhanced catalytic effect, magnetic moment and might be manipulated to engineer the desirable properties *via* edge engineering. Our result could readily be applicable and expandable to other vdW 2D heterostructures and unravels the profound effect of defective template on the structural properties of heterostructure.

5.2. Experimental section

Synthesis of ncG films. Inductively coupled plasma CVD was utilized to synthesize the ncG at 500 °C with acetylene (C_2H_2) as the carbon source. H_2 plasma treatment was pre-performed for 5 min at a plasma power of 150 W to remove the native oxides from the metals. The detailed method for ncG film synthesis is described in Reference¹⁷⁰.

Synthesis of WSe_2 flakes on ncG film. WSe_2 was synthesized by powder-based CVD. The target substrate was located with the sputtered 3-nm-thick WO_3 precursor face-to-face at the center of the quartz furnace, and 100 mg selenium powder in alumina boats was placed in the upstream of the CVD system. After purging with 50 sccm Ar flow, CVD growth was performed at atmospheric pressure with a continuous flow of 40 sccm Ar and 10 sccm H_2 gas. The temperature of the furnace was gradually raised to 950 °C; the sulfur powder started to melt at ~ 850 °C (heated to 300 °C using an equipped heating jacket). The system remained for 10 min at this growth temperature of 950 °C, followed by slow cooling to room temperature without opening the furnace cover.

Characterization. To investigate the surface morphology and height of synthesized WSe_2 , SEM and AFM measurements were performed, and the detailed methods are described in Chapter 3.2. TEM observations were performed using a FEI Titan cube G2 60-300 equipped with image- and probe-aberration correctors. AR-STEM mode was used for investigating atomic configurations and morphology. For TEM analysis, the WSe_2 /ncG heterostructures grown on SiO_2/Si substrates were directly transferred to TEM grids using the conventional wet transfer method without PMMA coating. All TEM experiments were operated at an acceleration voltage of 200 kV to observe thicker specimen with high resolution.

5.3. Growth behavior of WSe₂ grown on the nanocrystalline graphene

A representative schematic illustration of synthesis of various TMDs (formulated by MX₂; M = Mo, W, X = S, Se) grown on the ncG substrate is depicted in Figure 5.1a. To understand the impact of substrate crystallinity on the growth behavior of TMDs, we compared two types of samples: 1) WSe₂ grown on the SiO₂/Si substrate (denoted as *s*-WSe₂) and 2) WSe₂ grown on the ncG/SiO₂/Si substrate (denoted as *n*-WSe₂). Figure 5.1b and c are representative BSE-SEM images of WSe₂ flakes grown on the SiO₂ and ncG substrate, respectively, using the same growth parameters (detailed description of growth method is depicted in Chapter 5.2). *n*-WSe₂ flakes show higher intensity in BSE-SEM image and reduced lateral size compared to the *s*-WSe₂. Because intensity in BSE-SEM image is proportional to the thickness and atomic number, *n*-WSe₂ indicates the multilayered growth rather than the lateral growth. Likewise, ncG template plays an important role in high nucleation density and multilayer growth of WSe₂, while pristine graphene template facilitates lateral growth with confined lattice orientation showing aligned monolayer WSe₂ triangular flakes¹⁷¹. It indicates that there is a notable difference in interface energy according to the crystallinity of graphene.

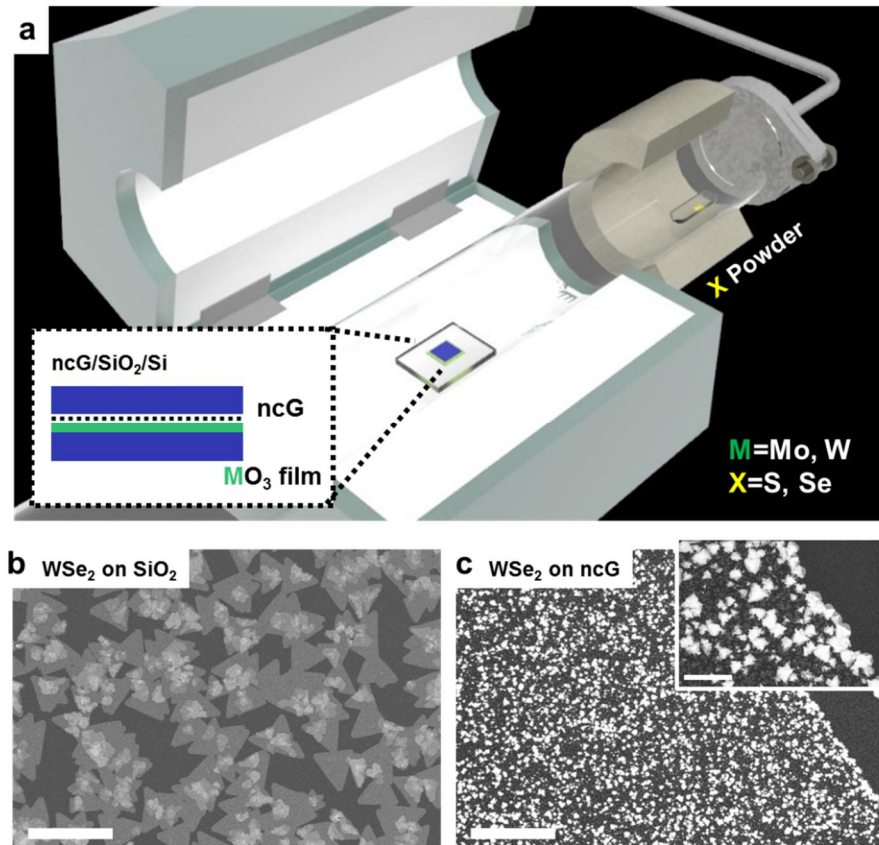


Figure 5.1. The growth behavior of WSe₂ grown on the SiO₂/Si and ncG. (a) Schematic of synthesis of various TMDs on ncG substrate using powder-based CVD. (b,c) BSE-SEM images of *s*-WSe₂ (WSe₂ grown on the SiO₂ substrate) and *n*-WSe₂ (WSe₂ grown on the ncG substrate). Higher intensity of flakes means thicker WSe₂ flakes. Scale bar for (b,c) and inset in (c), 5 μm and 1 μm, respectively

Raman spectra (Figure 5.2a) show that WSe₂ peak (degenerated E_{2g}+A_{1g} peak ~250 cm⁻¹)¹⁷² is clearly observed, indicating that the WSe₂ flakes are successfully synthesized for both templates (ncG and SiO₂/Si substrate). Although significant difference in thickness between *s*-WSe₂ and *n*-WSe₂ as shown in BSE-SEM image (Figure 5.1b,c), there is no any WSe₂ peak shift, because it is not dependent on a thickness of WSe₂. As shown in Figure 5.2b, as-grown ncG represents significant D band (~1354 cm⁻¹) due to the occurrence of any kind of disorder in sp² hybridized graphene matrix. The D' band (~1620 cm⁻¹) is related with disordered structure and is often found in the nanocrystalline graphite¹⁷³, indicating that the ncG template has the large number of defect sites with nanocrystallinity. There is no peak shift of G and 2D band between bare ncG and WSe₂/ncG heterostructure, indicating that the ncG template act as free from friction and strain effects.

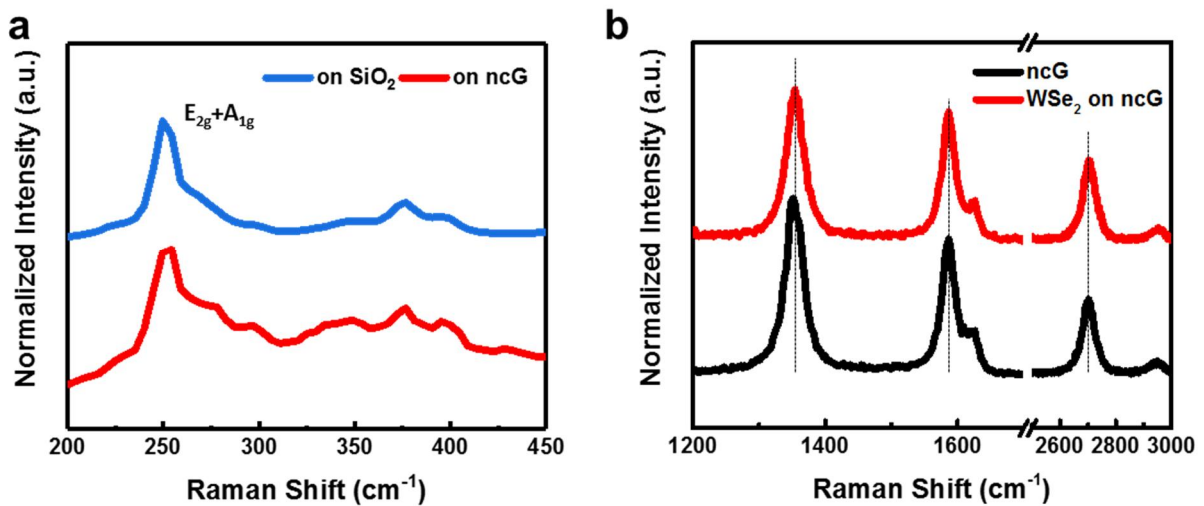


Figure 5.2. Raman analysis of WSe₂/ncG heterostructure. (a) Degenerated E_{2g}+A_{1g} peak of WSe₂ flakes grown on the ncG (red) and SiO₂/Si (blue), respectively. (b) Carbon peak of ncG before (black) and after (red) WSe₂ growth.

For investigating the morphology and thickness of n -WSe₂, we performed AFM analysis using tapping mode (Figure 5.3). From the outer to the center of a cluster, the cluster becomes thicker as the contrast becomes brighter. The corresponding height profile across the cluster (Insets in height image of Figure 5.3) displays that the maximum height is around 12 nm at the center, relative to the ncG. Simultaneously obtained phase image shows the brighter contrast at WSe₂ cluster, compared to the exposed ncG surface, indicating that the different material is successfully synthesized, which is WSe₂ flakes.

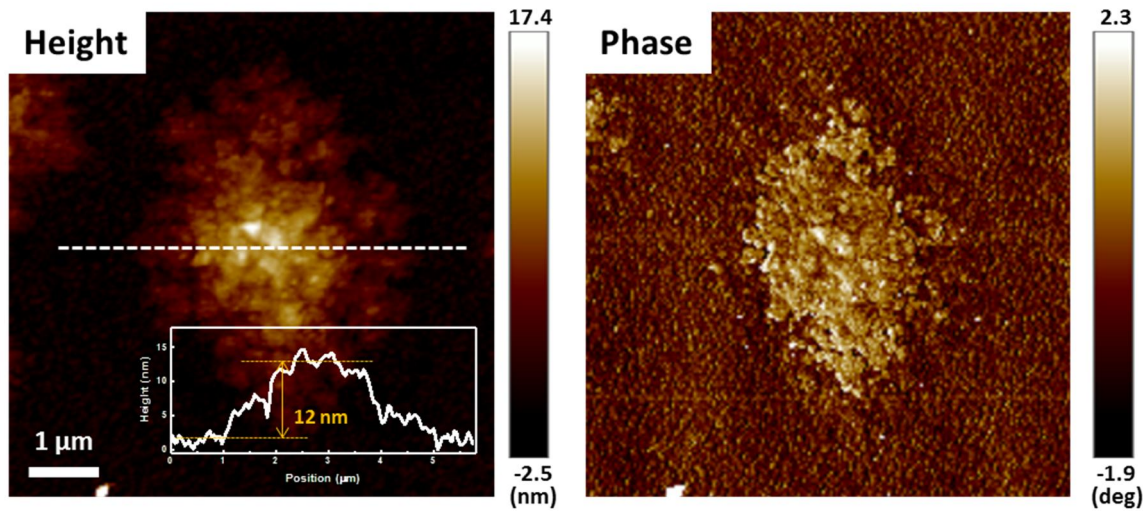


Figure 5.3. AFM height and phase image of WSe₂/ncG heterostructure using tapping mode. Inset in height image is line profile across the one cluster of WSe₂. Scale bar is 1 μm.

5.4. Edge rich multilayered WSe₂

To investigate the orientation and atomic structure of WSe₂ clusters grown on the ncG films, we performed TEM experiment. Figure 5.4 depicts the *n*-WSe₂ cluster in high magnification. The transition from purple to yellow in Figure 5.4a and 4b means an increase in the thickness of WSe₂, which is consistent with the AFM height image in that the cluster center has the highest thickness. Although its shape roughly follows a triangular shape, it has fractal morphology rather than a regular triangular flake. It means that the WSe₂ domains grow in the diffusion-limited regime, in other words, the rate of attachment is higher than the rates of edge diffusion and surface diffusion¹⁷⁴. Figure 5.4b represents the outer region of a cluster, indicating large amount of edge states with saw-toothed shape for maintaining energetically stable edge configuration. Figure 5.4c shows atomic resolution image of corner region of a cluster having 1 to 6 layers of WSe₂ and Figure 5.4d represents SAED pattern of WSe₂ cluster and ncG heterostructure. Ring diffraction pattern is reflected by ncG film showing its nanocrystallinity, and one set of hexagonal diffraction spot is reflected from the synthesized WSe₂ cluster. The corresponding intensity line profile shows asymmetric intensity in 1st order diffraction spots, indicating that the grown multilayered WSe₂ has AB-stacked (called 3R stacking geometry) structure due to the 3-fold symmetry of WSe₂. It is consistent with the AB-stacked atomic structure of bilayer region as shown in Figure 5.4c. Table 5.1 shows the d-spacing of ncG before and after WSe₂ growth, showing no significant strain, consistent with the Raman result (Figure 5.2b). Nanobeam diffraction (NBD) allows determining strain and orientation in crystalline materials with high spatial resolution using atomically probed beam¹⁷⁵, instead of finite size of aperture. Figure 5.5a depicts the highly aligned between WSe₂ domains and one nano-sized grain in ncG, similar to the grown on the defective graphene (Figure 5.5b).

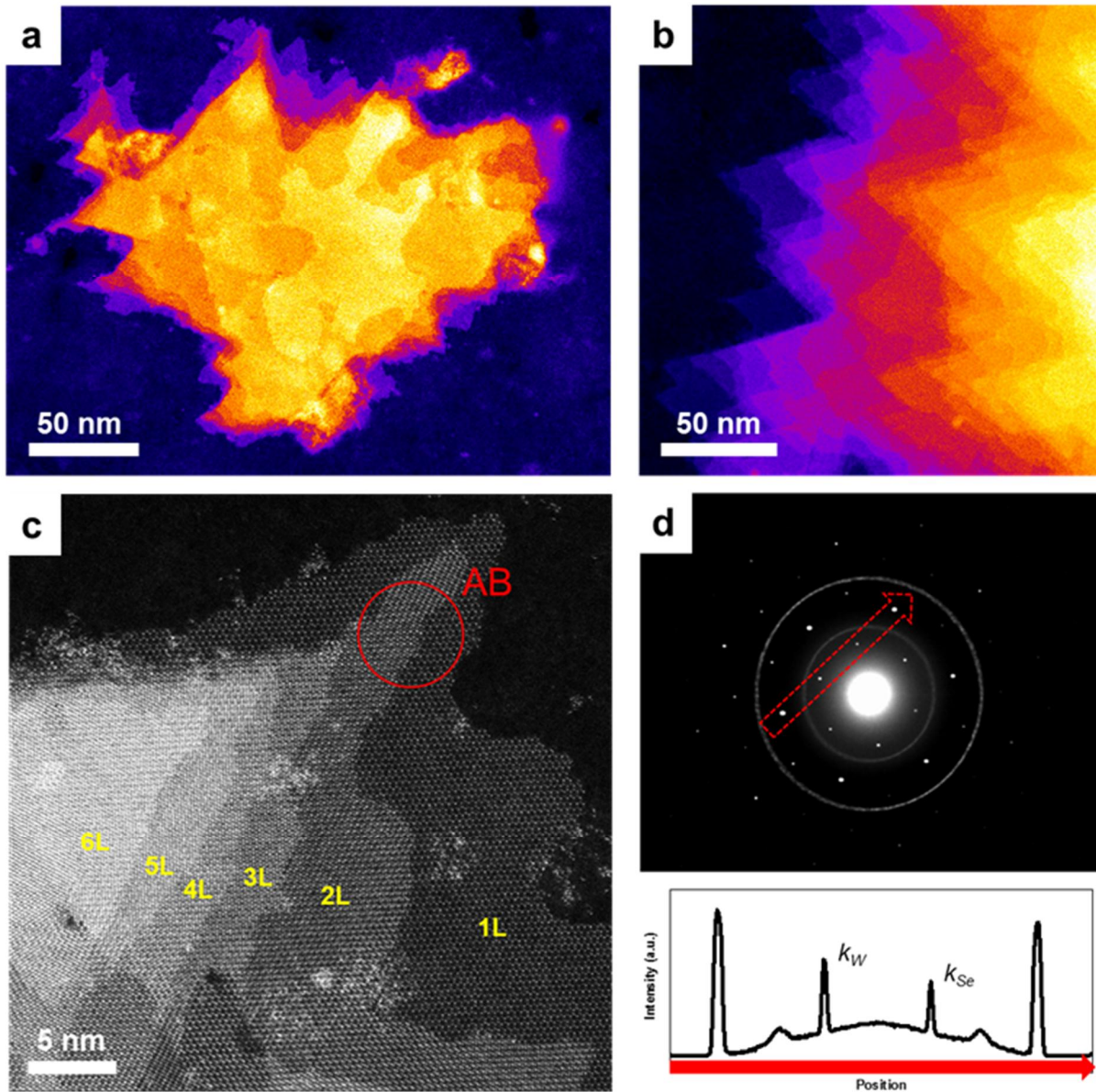
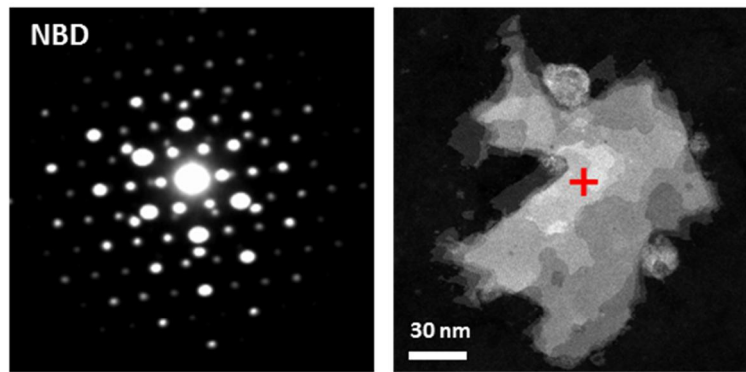


Figure 5.4. Edge rich multilayered WSe₂ cluster grown on the ncG template. (a,b) False-colored STEM images of one WSe₂ cluster, showing (a) whole cluster and (b) a magnified view. (c) AR-STEM image of synthesized WSe₂ of 1 - 6 layers. (d) SAED pattern of synthesized WSe₂, showing anisotropic intensity of 1st order diffraction pattern, indicating 3R stacking order of WSe₂. Scale bar for (a,b) and (c), 50 nm and 5 nm, respectively.

d-spacing (nm)		ncG			Graphene
		As grown	ncG (annealed)	WSe ₂ /ncG	Theo.
1 st	AVE.	0.206961	0.207194	0.2059	0.213
	STD.	0.002168	0.002141	0.002162	
2 nd	AVE.	0.119456	0.119478	0.119556	0.1235
	STD.	0.001203	0.001322	0.002258	

Table 5.1. Lattice spacing of ncG before and after WSe₂ growth on ncG substrate.

a WSe₂ grown on ncG



b WS₂ grown on Graphene GB

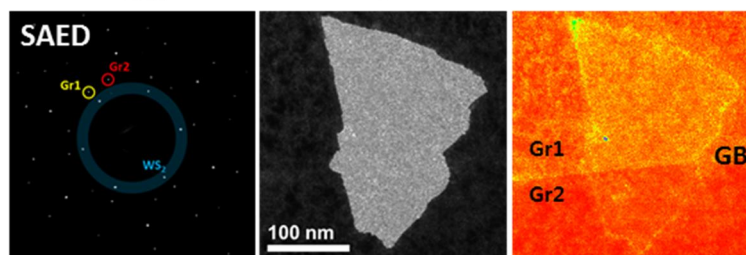


Figure 5.5. Orientation relationship between WSe₂ domain and ncG film with high spatial resolution. (a) NBD analysis of WSe₂/ncG heterostructure, indicating highly aligned orientation between WSe₂ and a ncG grain. Because we used atomic size of probe beam, we can obtain highly localized structural information. (b) SAED pattern, DF-TEM of WS₂ and graphene in WS₂/graphene heterostructure, when the WS₂ flake is nucleated at the GB of graphene. (b) is reproduced from ref¹³.

Synthesized WSe₂ domains have edge rich state, depicted in Figure 5.4a and 4b. For examining the atomic configuration of WSe₂ edge, we performed AR-STEM analysis. Compared to the W-terminated edge in WS₂/graphene heterostructure (as shown in Figure 3.1 and 3.2), *n*-WSe₂ has Se terminated edge with some of kinks (Figure 5.6a; orange arrows) and it indicates that *n*-WSe₂ is grown under the high Se flux environment¹⁷⁴. The formation energy of WSe₂ nanoribbon according to the chemical potential of Se displays the Se-terminated edge is the most stable edge configuration in the whole range of chemical environment condition and much more stable under the Se-rich condition¹⁷⁶. The corresponding intensity profile across the edge displays negligible intensity difference between the outermost edge and 2Se column. From these results, we can deduce that the *n*-WSe₂ has Se-edge with 100% Se coverage, which is predicted to have magnetic moment from the unpaired *p* electrons of the Se atom¹³⁴. Interestingly, there are many discrete W atoms near the WSe₂ domains (Figure 5.6a; green arrows), assuming that due to the higher attachment rate than the edge and surface diffusion rate¹⁷⁴. In addition, there are many intrinsic defect sites (*e.g.* adatom, chalcogen vacancy). Adatom distribution is much higher than the TMD grown on the pristine graphene (Figure 5.6a; red arrows), suggesting that it is appreciated to the W atomic bridge, but further work should be required, such as cross-section analysis.

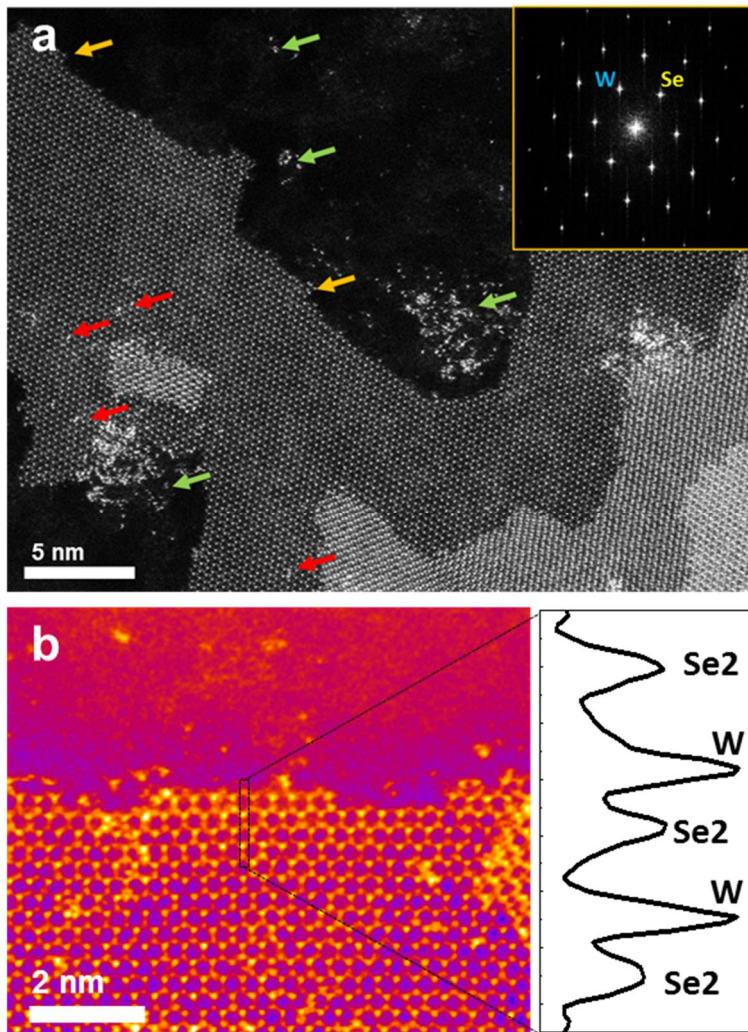


Figure 5.6. Atomic scale edge configuration of n -WSe₂. (a) AR-STEM image of n -WSe₂. Whole layers are aligned with same orientation. Orange, green and red arrows indicate the kink, discretely attached W atoms and adatoms, respectively. (b) Magnified AR-STEM image of edge region of n -WSe₂ and corresponding intensity line profile, indicating Se edge with 100% Se coverage.

5.5. Electronic property of WSe₂/ncG heterostructure

Work function (WF) of heterostructure is strongly important because it is closely related with the FET performance¹⁷⁷. For investigating WF of our heterostructure, we performed ultraviolet photoelectron spectroscopy (UPS) using He I source with 21.2 eV of photon energy. As shown in Figure 5.7, the WSe₂/ncG heterostructure has down-shifted WF due to the pinning effect to the charge neutrality point of WSe₂. Generally, it is well known that the valence band maximum of WSe₂ is around 5.2 eV¹⁶⁹, therefore *n*-WSe₂/ncG could have improved carrier-injection contact with small Schottky barrier height. However, further study of the detailed electronic properties of *n*-WSe₂ is necessary for a deep understanding the interface-driven metal–semiconductor junctions and their applications in WF engineering.

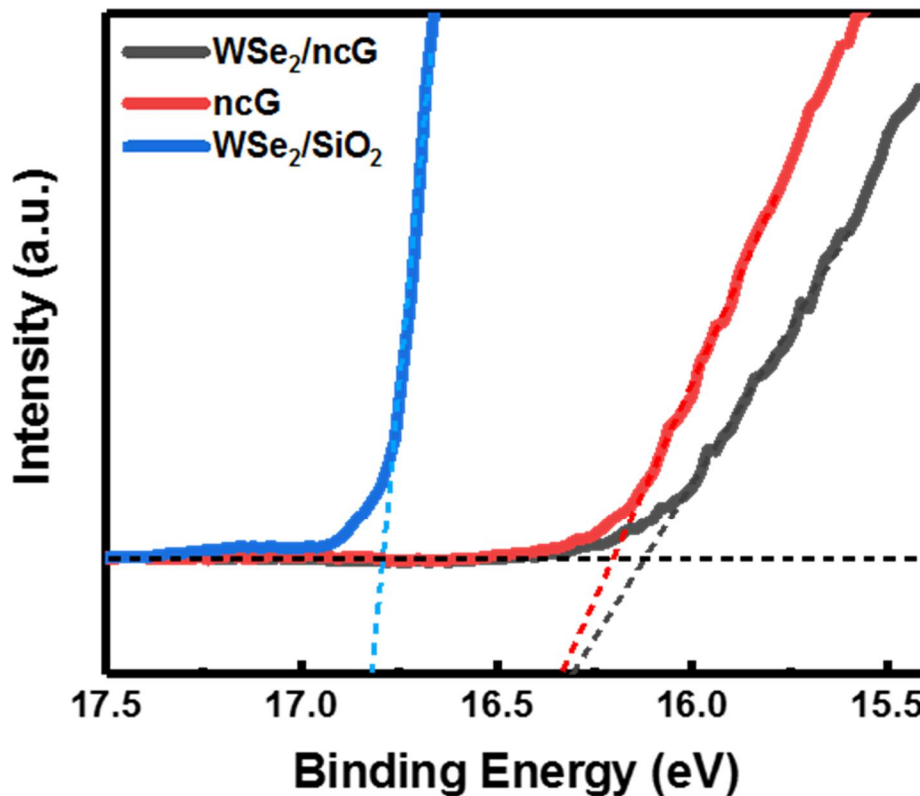


Figure 5.7. UPS spectra of WSe₂ on SiO₂ (blue), ncG (red) and *n*-WSe₂ (black) using He I source ($h\nu = 21.2$ eV) and measured WF.

5.6. Conclusion and outlook

Defects have been considered the cause of deterioration of material performance, so defect-free growth of 2D crystals has been extensively studied. In addition, the vdW epitaxial growth mechanism enables us to fabricate the epilayer in a defined orientation depending on the orientation of substrate. Therefore, large grain graphene substrates have been utilized to synthesize less defective TMD in TMD/graphene heterostructures. However, previous research reported that WS₂ grown on GB of graphene substrate strongly induces other interlayer properties of WS₂/graphene heterostructure compared to WS₂ on basal plane of graphene¹³. In this sense, the influence of the crystallinity of the graphene substrate on the growth behavior and interlayer properties of the epilayer TMDs is very curious.

In summary of this chapter, we synthesized edge-rich multilayer WSe₂ domains using graphene with nanocrystallinity as a template. The synthesized domain exhibits a fractal morphology with an edge-rich state instead of straight triangular flake due to the diffusion-limited regime, which has a diffusion rate lower than the rate of attachment due to the highly defective sites. ncG template act as free from friction and strain effects in that no significant d-spacing of ncG, no peak shift of WSe₂, carbon-related D, G and 2D bands. Locally, WSe₂ domains are oriented with one of grains in ncG matrix *via* vdW epitaxy. Our WSe₂ domains are terminated by Se-terminated edge, predicted to appear ferromagnetic property with unpaired electrons. Edge engineering based on the edge-rich WSe₂ template could be useful for designing desirable properties and expanding the various applications. In addition, WSe₂/ncG heterostructure has down-shifted WF, which is comparable to valence band maximum of WSe₂, which could be potential for p-type FET.

Edges, especially in various TMDs, have been received extensive interests due to their novel properties driven by unpaired electrons. For example, edges in TMDs show magnetic moments with confined edges configurations and magnetic properties could be strongly magnified by decorating appropriate transition metals *via* edge engineering. To date, edge decoration using various transition metal¹³⁵ (*e.g.* Co, Mn, Fe) has been theoretically studied to predict stability, magnetic and electronic properties, but the experimental results have not yet been demonstrated because they are easy to oxidize. Therefore, experiments have been carried out by decorating novel metals (*e.g.* Au) using the solution method^{178,179} and previous reports showed that the Au-decorated MoS₂ shows *p*-doping effects without degrading intrinsic electrical properties¹⁷⁸. In this sense, edge engineering using edge-rich TMDs should be further studied to induce magnetism and achieve 2D magnets.

Chapter 6. Conclusion

In this thesis, I have studied the effect of the structural features of a graphene template on the heterostructure configuration and its corresponding properties using aberration corrected modern TEM. Various modes of TEM (*e.g.* DF-TEM, AR-TEM, AR-STEM) and STEM-based spectroscopy (*e.g.* EELS, EDS) are highly advantageous for defect studies with high-spatial and energy resolution.

Pristine graphene template, which is free of friction and dangling bonds, leads to the APB defects of TMDs *via* vdW epitaxy. Previously, APB in the 2H phase of TMDs attracted broad interest as a 1D metallic wire embedded in a semiconducting matrix. Highly manipulated APB defects in a CVD-synthesized W(Mo)S₂/graphene heterostructure show the anisotropic features of APBs, which are unpredicted through calculation. Depending on which elements meet front-facing (*i.e.* W/Mo-facing, S-facing) atomic-scale configurations of APBs have no significant difference; however, they do have a significant effect on the overall features (*i.e.* straight for chalcogen-facing APB and saw-toothed for transition-metal-facing APB) and electronic properties. Although both types of APBs have metallic properties, two-probe FET results show that the saw-toothed APB with many kinks results in a considerably lower electron mobility than the straight APB, indicating that the kinks of APBs are dominant scattering centers.

The wrinkle-rich graphene template, inducing additional friction, manipulates the Shockley partial dislocation-driven SBs in multilayer WS₂. Graphene wrinkles function as highly reactive nucleation sites for the WS₂ epilayer growth; at the same time, however, they impede lateral growth and induce additional stress in the epilayer due to the non-negligible friction from the non-flat structure. Anisotropic friction of graphene wrinkles leads to the different density of SBs depending on the angle between the dislocation direction and graphene wrinkle direction, which are closely related with the anisotropic friction of graphene wrinkle, reported in previous research. Moreover, partial dislocation-driven in-plane strain facilitates out-of-plane buckling with a height of 1 nm to release the in-plane strain. Remarkably, in-plane strain relaxation at partial dislocations restores the band gap to that of monolayer WS₂ due to reduced interlayer interaction.

Nanocrystalline graphene with many dangling bonds causes edge rich multilayered WSe₂ domains. A defect-based diffusion rate lower than the attachment rate leads to the diffusion-limited regime condition and displays the fractal morphology of WSe₂ domains with edge rich states. The Fermi level of a WSe₂/ncG heterostructure has a strongly down-shifted Fermi level similar to the valence band maximum of WSe₂, which might pave the way to applying the effective hole injection layer. In addition, atomic-resolution analysis shows that the WSe₂ domains have Se-terminated edges, which have been predicted to have a magnetic moment from unpaired electrons. Edge-rich states with confined edge configurations could have potential in catalytic and magnetic applications and with, effective edge

engineering, can be used to significantly improve performance (*e.g.* edge decoration with transition metals for enhanced magnetic properties)

Our findings clarify the profound effects of substrate morphology and crystallinity on the structural features and corresponding properties of vdW heterostructures. Our understanding of interface-mediated novel defect structures and the relationship between the structure and corresponding property could be appreciable for designing desirable properties and expanding the range of application of vdW heterostructures *via* interface engineering.

Chapter 7. Perspective and outlook

We revealed the profound effect of the structural features of substrates on the growth behavior, interface-driven novel defects of heterostructures, and the corresponding properties, using various graphene templates: 1) Pristine, 2) folded wrinkle-rich graphene (morphological defect), and 3) nanocrystalline graphene (crystallinity defect). Our results indicate that controlling the structural features of substrate templates could be one of the most effective ways to design desirable properties of 2D vdW heterostructures and it could have the potential for a wide range of future applications.

Pristine graphene manipulates two types of APBs and has a critical impact on the electron transport behavior of TMD-based FET devices. The straight features of APBs show slightly enhanced transport behavior, while the saw-toothed features of APBs strongly degrade the electrical properties. The vdW epitaxy confines the epilayer orientation but both types of APBs are inevitably generated due to the bi-element nature of TMDs. Recently, J.S. Lee *et al.* reported the use of genuine single-crystal h-BN film with liquid gold¹⁸⁰ to eliminate the inevitable defect lines. Considering that the straight features APBs enhance transport behavior, it would be desirable to manipulate only the chalcogen-facing APB *via* controlling site-specific growth¹⁸¹ and edge configuration (related to the synthesis condition).

Wrinkle-rich graphene manipulates the high density of AB/AC SBs with out-of-plane buckled structure. Out-of-plane deformed structures are closely related to friction¹⁸², which suggests a new way to modulate the friction property of vdW heterostructures by controlling wrinkle structures¹⁸³. In addition, AB/AC SBs in bilayer graphene show insulating-like behavior explained by scattering on boundaries¹⁴⁶. Likewise, a detailed investigation of optical, electronic and mechanical properties of AB/AC SBs in TMDs is required to correlate the properties and out-of-plane buckled defects and to widen their range of applications.

Highly defective nanocrystalline graphene manipulates edge-rich multilayered TMD flakes due to the diffusion-limited growth regime. Edges in various TMDs have been extensively researched due to their novel catalytic¹⁸⁴, magnetic⁴³, and electronic¹⁸⁵ properties driven by unpaired electrons. Magnetic moments with confined edges configurations could be strongly magnified by decorating appropriate transition metals *via* edge engineering. Magnetic 2D materials have garnered much interest but have not been experimentally researched, because generally well-known magnetic 2D materials (*e.g.* Fe₃GeTe₂) are easily oxidized in ambient conditions. In this sense, edge engineering using edge rich TMDs could be one of the most effective approaches for inducing magnetism and achieving 2D magnets.

REFERENCES

- 1 Zhan, Y. J., Liu, Z., Najmaei, S., Ajayan, P. M. & Lou, J. Large-Area Vapor-Phase Growth and Characterization of MoS₂ Atomic Layers on a SiO₂ Substrate. *Small* **8**, 966-971 (2012).
- 2 Chen, K. *et al.* Lateral Built-In Potential of Monolayer MoS₂-WS₂ In-Plane Heterostructures by a Shortcut Growth Strategy. *Adv. Mater.* **27**, 6431-6437 (2015).
- 3 Lee, Y. H. *et al.* Synthesis of Large-Area MoS₂ Atomic Layers with Chemical Vapor Deposition. *Adv. Mater.* **24**, 2320-2325 (2012).
- 4 Ago, H. *et al.* Visualization of Grain Structure and Boundaries of Polycrystalline Graphene and Two-Dimensional Materials by Epitaxial Growth of Transition Metal Dichalcogenides. *ACS Nano* **10**, 3233-3240 (2016).
- 5 Gong, Y. J. *et al.* Vertical and In-Plane Heterostructures from WS₂/MoS₂ Monolayers. *Nat. Mater.* **13**, 1135-1142 (2014).
- 6 Kim, S. Y., Kwak, J., Ciobanu, C. V. & Kwon, S. Y. Recent Developments in Controlled Vapor-Phase Growth of 2D Group 6 Transition Metal Dichalcogenides. *Adv. Mater.* **31**, 1804939 (2019).
- 7 Chen, L. *et al.* Step-Edge-Guided Nucleation and Growth of Aligned WSe₂ on Sapphire via a Layer-over-Layer Growth Mode. *ACS Nano* **9**, 8368-8375 (2015).
- 8 Shi, J. P. *et al.* Substrate Facet Effect on the Growth of Mono layer MoS₂ on Au Foils. *ACS Nano* **9**, 4017-4025 (2015).
- 9 Peng, B. *et al.* Ultrafast Charge Transfer in MoS₂/WSe₂ *p-n* Heterojunction. *2D Mater.* **3**, 025020 (2016).
- 10 Geim, A. K. & Grigorieva, I. V. Van der Waals heterostructures. *Nature* **499**, 419-425 (2013).
- 11 Kim, S. Y. *et al.* Substantial Improvements of Long-term Stability in Encapsulation-free WS₂ using Highly Interacting Graphene Substrate. *2D Mater.* **4**, 011007 (2017).
- 12 Lin, Y. C. *et al.* Direct Synthesis of van der Waals Solids. *ACS Nano* **8**, 3715-3723 (2014).
- 13 Kim, S. Y. *et al.* The Impact of Substrate Surface Defects on the Properties of Two-Dimensional van der Waals Heterostructures. *Nanoscale* **10**, 19212-19219 (2018).
- 14 Li, S. L. *et al.* Thickness-Dependent Interfacial Coulomb Scattering in Atomically Thin Field-Effect Transistors. *Nano Lett.* **13**, 3546-3552 (2013).
- 15 Radisavljevic, B. & Kis, A. Mobility Engineering and a Metal-Insulator Transition in Monolayer MoS₂. *Nat. Mater.* **12**, 815-820 (2013).
- 16 Jariwala, D. *et al.* Band-like Transport in High Mobility Unencapsulated Single-layer MoS₂ Transistors. *Appl. Phys. Lett.* **102**, 173107 (2013).
- 17 English, C. D., Shine, G., Dorgan, V. E., Saraswat, K. C. & Pop, E. Improved Contacts to MoS₂ Transistors by Ultra-High Vacuum Metal Deposition. *Nano Lett.* **16**, 3824-3830 (2016).
- 18 McDonnell, S., Addou, R., Buie, C., Wallace, R. M. & Hinkle, C. L. Defect-Dominated Doping and Contact Resistance in MoS₂. *ACS Nano* **8**, 2880-2888 (2014).

- 19 Tosun, M. *et al.* Air-Stable *n*-Doping of WSe₂ by Anion Vacancy Formation with Mild Plasma Treatment. *ACS Nano* **10**, 6853-6860 (2016).
- 20 Najmaei, S. *et al.* Electrical Transport Properties of Polycrystalline Monolayer Molybdenum Disulfide. *ACS Nano* **8**, 7930-7937 (2014).
- 21 Zhang, K. H. *et al.* Manganese Doping of Monolayer MoS₂: The Substrate Is Critical. *Nano Lett.* **15**, 6586-6591 (2015).
- 22 Mishra, R., Zhou, W., Pennycook, S. J., Pantelides, S. T. & Idrobo, J. C. Long-Range Ferromagnetic Ordering in Manganese-Doped Two-Dimensional Dichalcogenides. *Phys. Rev. B* **88**, 144409 (2013).
- 23 Voiry, D., Mohite, A. & Chhowalla, M. Phase Engineering of Transition Metal Dichalcogenides. *Chem. Soc. Rev.* **44**, 2702-2712 (2015).
- 24 Choe, D. H., Sung, H. J. & Chang, K. J. Understanding Topological Phase Transition in Monolayer Transition Metal Dichalcogenides. *Phys. Rev. B* **93**, 125109 (2016).
- 25 Kappera, R. *et al.* Phase-Engineered Low-Resistance Contacts for Ultrathin MoS₂ Transistors. *Nat. Mater.* **13**, 1128-1134 (2014).
- 26 Wang, L. F., Xu, Z., Wang, W. L. & Bai, X. D. Atomic Mechanism of Dynamic Electrochemical Lithiation Processes of MoS₂ Nanosheets. *J. Am. Chem. Soc.* **136**, 6693-6697 (2014).
- 27 Kwak, J. *et al.* Single-Crystalline Nanobelts Composed of Transition Metal Ditellurides. *Adv. Mater.* **30**, 1707260 (2018).
- 28 Lin, Y. C. *et al.* Single-Layer ReS₂: Two-Dimensional Semiconductor with Tunable In-Plane Anisotropy. *ACS Nano* **9**, 11249-11257 (2015).
- 29 Komsa, H. P., Kurasch, S., Lehtinen, O., Kaiser, U. & Krasheninnikov, A. V. From Point to Extended Defects in Two-Dimensional MoS₂: Evolution of Atomic Structure under Electron Irradiation. *Phys. Rev. B* **88**, 035301 (2013).
- 30 Cho, S. *et al.* Phase Patterning for Ohmic Homojunction Contact in MoTe₂. *Science* **349**, 625-628 (2015).
- 31 Ke, Q. Q. *et al.* Strong Charge Transfer at 2H-1T Phase Boundary of MoS₂ for Superb High-Performance Energy Storage. *Small* **15**, 1900131 (2019).
- 32 Sahoo, P. K., Memaran, S., Xin, Y., Balicas, L. & Gutierrez, H. R. One-Pot Growth of Two-Dimensional Lateral Heterostructures via Sequential Edge-Epitaxy. *Nature* **553**, 63-67 (2018).
- 33 Sahoo, P. K. *et al.* Bilayer Lateral Heterostructures of Transition-Metal Dichalcogenides and Their Optoelectronic Response. *ACS Nano* **13**, 12372-12384 (2019).
- 34 van der Zande, A. M. *et al.* Grains and Grain Boundaries in Highly Crystalline Monolayer Molybdenum Disulfide. *Nat. Mater.* **12**, 554-561 (2013).
- 35 Zhou, W. *et al.* Intrinsic Structural Defects in Monolayer Molybdenum Disulfide. *Nano Lett.* **13**, 2615-2622 (2013).

- 36 Azizi, A. *et al.* Dislocation Motion and Grain Boundary Migration in Two-Dimensional Tungsten Disulphide. *Nat. Commun.* **5**, 4867 (2014).
- 37 Ly, T. H. *et al.* Misorientation-Angle-Dependent Electrical Transport Across Molybdenum Disulfide Grain Boundaries. *Nat. Commun.* **7**, 10426 (2016).
- 38 Dumcenco, D. *et al.* Large-Area MoS₂ grown using H₂S as the sulphur source. *2D Mater.* **2**, 044005 (2015).
- 39 Cao, D., Shen, T., Liang, P., Chen, X. S. & Shu, H. B. Role of Chemical Potential in Flake Shape and Edge Properties of Monolayer MoS₂. *J. Phys. Chem. C* **119**, 4294-4301 (2015).
- 40 Wang, S. S. *et al.* Shape Evolution of Monolayer MoS₂ Crystals Grown by Chemical Vapor Deposition. *Chem. Mater.* **26**, 6371-6379 (2014).
- 41 Wang, S. S. *et al.* Atomically Sharp Crack Tips in Monolayer MoS₂ and Their Enhanced Toughness by Vacancy Defects. *ACS Nano* **10**, 9831-9839 (2016).
- 42 Ly, T. H., Zhao, J., Cichocka, M. O., Li, L. J. & Lee, Y. H. Dynamical Observations on the Crack Tip Zone and Stress Corrosion of Two-Dimensional MoS₂. *Nat. Commun.* **8**, 14116 (2017).
- 43 Chen, Q. *et al.* Atomically Flat Zigzag Edges in Monolayer MoS₂ by Thermal Annealing. *Nano Lett.* **17**, 5502-5507 (2017).
- 44 Sang, X. H. *et al.* *In situ* edge engineering in two-dimensional transition metal dichalcogenides. *Nat. Commun.* **9**, 2051 (2018).
- 45 Huang, W., Wang, X. W., Ji, X. J., Zhang, Z. & Jin, C. H. *In-situ* Fabrication of Mo₆S₆-Nanowire-Terminated Edges in Monolayer Molybdenum Disulfide. *Nano Res.* **11**, 5849-5857 (2018).
- 46 Li, M. Y. *et al.* Epitaxial Growth of a Monolayer WSe₂-MoS₂ Lateral *p-n* Junction with an Atomically Sharp Interface. *Science* **349**, 524-528 (2015).
- 47 Zhang, Z. W. *et al.* Robust Epitaxial Growth of Two-Dimensional Heterostructures, Multiheterostructures, and Superlattices. *Science* **357**, 788-792 (2017).
- 48 Xie, S. E. *et al.* Coherent, Atomically Thin Transition-Metal Dichalcogenide Superlattices with Engineered Strain. *Science* **359**, 1131-1135 (2018).
- 49 Georgiou, T. *et al.* Vertical Field-Effect Transistor Based on Graphene-WS₂ Heterostructures for Flexible and Transparent Electronics. *Nat. Nanotechnol.* **8**, 100-103 (2013).
- 50 Chiu, M. H. *et al.* Determination of Band Alignment in the Single-Layer MoS₂/WSe₂ Heterojunction. *Nat. Commun.* **6**, 7666 (2015).
- 51 Novoselov, K. S. *et al.* Electric Field Effect in Atomically Thin Carbon Films. *Science* **306**, 666-669 (2004).
- 52 Banhart, F., Kotakoski, J. & Krashennnikov, A. V. Structural Defects in Graphene. *ACS Nano* **5**, 26-41 (2011).

- 53 Urban, K. W. Studying Atomic Structures by Aberration-Corrected Transmission Electron Microscopy. *Science* **321**, 506-510 (2008).
- 54 Muller, D. A. *et al.* Atomic-Scale Chemical Imaging of Composition and Bonding by Aberration-Corrected Microscopy. *Science* **319**, 1073-1076 (2008).
- 55 Sawada, H., Sasaki, T., Hosokawa, F. & Suenaga, K. Atomic-Resolution STEM Imaging of Graphene at Low Voltage of 30 kV with Resolution Enhancement by Using Large Convergence Angle. *Phys. Rev. Lett.* **114**, 166012 (2015).
- 56 Wang, H. T. *et al.* Interaction Between Single Gold Atom and the Graphene Edge: A Study via Aberration-Corrected Transmission Electron Microscopy. *Nanoscale* **4**, 2920-2925 (2012).
- 57 Warner, J. H. *et al.* Dislocation-Driven Deformations in Graphene. *Science* **337**, 209-212 (2012).
- 58 Meyer, J. C. *et al.* Direct Imaging of Lattice Atoms and Topological Defects in Graphene Membranes. *Nano Lett.* **8**, 3582-3586 (2008).
- 59 Hetherington, C. Aberration Correction for TEM. *Mater. Today* **7**, 50-55 (2004).
- 60 Phillipp, F., Hoschen, R., Osaki, M., Mobus, G. & Ruhle, M. New High-Voltage Atomic-Resolution Microscope Approaching 1-Angstrom Point Resolution Installed in Stuttgart. *Ultramicroscopy* **56**, 1-10 (1994).
- 61 Smith, B. W. & Luzzi, D. E. Electron Irradiation Effects in Single Wall Carbon Nanotubes. *J. Appl. Phys.* **90**, 3509-3515 (2001).
- 62 Jiang, N. Electron Beam Damage in Oxides: a Review. *Rep. Prog. Phys.* **79**, 016501 (2016).
- 63 Rakhovskaya, O. V., Elovikov, S. S., Dubinina, E. M., Shakhurin, E. S. & Dementjev, A. P. Electron-Stimulated Desorption Process from Ionic Compound Surface. *Surf. Sci.* **274**, 190-198 (1992).
- 64 Bleloch, A. & Lupini, A. Imaging at the Picoscale. *Mater. Today* **7**, 42-48 (2004).
- 65 Krivanek, O. L., Nellist, P. D., Dellby, N., Murfitt, M. F. & Szilagyi, Z. Towards Sub-0.5 Angstrom Electron Beams. *Ultramicroscopy* **96**, 229-237 (2003).
- 66 Haider, M., Braunshausen, G. & Schwan, E. Correction of the Spherical-Aberration of a 200-kB TEM by Means of a Hexapole-Corrector. *Optik* **99**, 167-179 (1995).
- 67 Haider, M. *et al.* Electron Microscopy Image Enhanced. *Nature* **392**, 768-769 (1998).
- 68 Krivanek, O. L. *et al.* Atom-by-Atom Structural and Chemical Analysis by Annular Dark-Field Electron Microscopy. *Nature* **464**, 571-574 (2010).
- 69 Rose, H. Outline of an Ultracorrector Compensating for all Primary Chromatic and Geometrical Aberrations of Charged-Particle Lenses. *Nucl. Instrum. Meth. A* **519**, 12-27 (2004).
- 70 Bangert, U. *et al.* STEM Plasmon Spectroscopy of Freestanding Graphene. *Phys. Status Solidi A* **205**, 2265-2269 (2008).

- 71 Eberlein, T. *et al.* Plasmon Spectroscopy of Free-standing Graphene Films. *Phys. Rev. B* **77**, 233406 (2008).
- 72 Scholl, J. A., Koh, A. L. & Dionne, J. A. Quantum Plasmon Resonances of Individual Metallic Nanoparticles. *Nature* **483**, 421-427 (2012).
- 73 Hong, H. K. *et al.* Atomic Scale Study on Growth and Heteroepitaxy of ZnO Monolayer on Graphene. *Nano Lett.* **17**, 120-127 (2017).
- 74 Gu, L. *et al.* Band-Gap Measurements of Direct and Indirect Semiconductors Using Monochromated Electrons. *Phys. Rev. B* **75**, 195214 (2007).
- 75 Kim, N. Y., Yim, T., Song, J. H., Yu, J. S. & Lee, Z. Microstructural Study on Degradation Mechanism of Layered $\text{LiNi}_{0.6}\text{Co}_{0.2}\text{Mn}_{0.2}\text{O}_2$ Cathode Materials by Analytical Transmission Electron Microscopy. *J. Power Sources* **307**, 641-648 (2016).
- 76 Senga, R. & Suenaga, K. Single-Atom Electron Energy Loss Spectroscopy of Light Elements. *Nat. Commun.* **6**, 7943 (2015).
- 77 Ramasse, Q. M. *et al.* Probing the Bonding and Electronic Structure of Single Atom Dopants in Graphene with Electron Energy Loss Spectroscopy. *Nano Lett.* **13**, 4989-4995 (2013).
- 78 Luo, C., Wang, C. L., Wu, X., Zhang, J. & Chu, J. H. *In Situ* Transmission Electron Microscopy Characterization and Manipulation of Two-Dimensional Layered Materials Beyond Graphene. *Small* **13**, 1604259 (2017).
- 79 Lin, Y. C., Dumcencu, D. O., Huang, Y. S. & Suenaga, K. Atomic Mechanism of the Semiconducting-to-Metallic Phase Transition in Single-Layered MoS_2 . *Nat. Nanotechnol.* **9**, 391-396 (2014).
- 80 Fei, L. F. *et al.* Direct TEM Observations of Growth Mechanisms of Two-Dimensional MoS_2 Flakes. *Nat. Commun.* **7**, 12206 (2016).
- 81 Sang, X. *et al.* Atomic Insight into Thermolysis-Driven Growth of 2D MoS_2 . *Adv. Func. Mater.* **29**, 1902149 (2019).
- 82 Asayesh-Ardakani, H. *et al.* Direct Evidence of M_2 Phase During the Monoclinic-Tetragonal (Rutile) Phase Transition of W-Doped VO_2 nanowires. *Appl. Phys. Lett.* **110**, 053107 (2017).
- 83 Xi, X. X. *et al.* Strongly Enhanced Charge-Density-Wave Order in Monolayer NbSe_2 . *Nat. Nanotechnol.* **10**, 765-769 (2015).
- 84 Kim, K. *et al.* Dedicated Preparation for *In Situ* Transmission Electron Microscope Tensile Testing of Exfoliated Graphene. *Applied Microscopy* **49**, 3 (2019).
- 85 Wang, X. G. *et al.* Growth Conditions Control the Elastic and Electrical Properties of ZnO Nanowires. *Nano Lett.* **15**, 7886-7892 (2015).
- 86 Brown, L. *et al.* Twinning and Twisting of Tri- and Bilayer Graphene. *Nano Lett.* **12**, 1609-1615 (2012).
- 87 Kim, C. J. *et al.* Stacking Order Dependent Second Harmonic Generation and Topological Defects in h-BN Bilayers. *Nano Lett.* **13**, 5660-5665 (2013).

- 88 Kim, J. H. *et al.* Interface-Driven Partial Dislocation Formation in 2D Heterostructures. *Adv. Mater.* **31**, 1807486 (2019).
- 89 Butz, B. *et al.* Dislocations in Bilayer Graphene. *Nature* **505**, 533-537 (2014).
- 90 Kim, J. H., Kim, K. & Lee, Z. The Hide-and-Seek of Grain Boundaries from Moire Pattern Fringe of Two-Dimensional Graphene. *Sci. Rep.-Uk* **5**, 12508 (2015).
- 91 Grantab, R., Shenoy, V. B. & Ruoff, R. S. Anomalous Strength Characteristics of Tilt Grain Boundaries in Graphene. *Science* **330**, 946-948 (2010).
- 92 Huang, P. Y. *et al.* Grains and Grain Boundaries in Single-Layer Graphene Atomic Patchwork Quilts. *Nature* **469**, 389-392 (2011).
- 93 Zhang, J. F., Zhao, J. J. & Lu, J. P. Intrinsic Strength and Failure Behaviors of Graphene Grain Boundaries. *ACS Nano* **6**, 2704-2711 (2012).
- 94 Yazyev, O. V. & Louie, S. G. Topological Defects in Graphene: Dislocations and Grain Boundaries. *Phys. Rev. B* **81**, 195420 (2010).
- 95 Kim, K. *et al.* Grain Boundary Mapping in Polycrystalline Graphene. *ACS Nano* **5**, 2142-2146 (2011).
- 96 Nyakiti, L. O. & Jankowski, A. F. Characterization of Strain-Rate Sensitivity and Grain Boundary Structure in Nanocrystalline Gold-Copper Alloys. *Metall. Mater. Trans. A* **41**, 838-847 (2010).
- 97 Nyakiti, L. O., Chaudhuri, J. & Jankowski, A. F. High-Resolution Electron Microscopy Characterization of Nanocrystalline Grain Boundaries in Gold-Copper Alloys. *Thin Solid Films* **517**, 1182-1185 (2008).
- 98 Abolhassani, M. & Mirzaei, M. Unification of Formulation of Moire Fringe Spacing in Parametric Equation and Fourier Analysis Methods. *Appl. Optics* **46**, 7924-7926 (2007).
- 99 Hetherington, C. J. D., Brown, P. D. & Duninborkowski, R. E. Applications of the Optical Moire Technique in HREM. *Inst. Phys. Conf. Ser.* **138**, 255-258 (1993).
- 100 Lu, C. C. *et al.* Twisting Bilayer Graphene Superlattices. *ACS Nano* **7**, 2587-2594 (2013).
- 101 Warner, J. H., Rummeli, M. H., Gemming, T., Buchner, B. & Briggs, G. A. D. Direct Imaging of Rotational Stacking Faults in Few Layer Graphene. *Nano Lett.* **9**, 102-106 (2009).
- 102 Komsa, H. P. *et al.* Two-Dimensional Transition Metal Dichalcogenides Under Electron Irradiation: Defect Production and Doping. *Phys. Rev. Lett.* **109**, 035503 (2012).
- 103 Ryu, G. H. *et al.* Line-Defect Mediated Formation of Hole and Mo Clusters in Monolayer Molybdenum Disulfide. *2D Mater.* **3**, 014002 (2016).
- 104 Liu, K., Feng, J. D., Kis, A. & Radenovic, A. Atomically Thin Molybdenum Disulfide Nanopores with High Sensitivity for DNA Translocation. *ACS Nano* **8**, 2504-2511 (2014).
- 105 Lehtinen, O. *et al.* Atomic Scale Microstructure and Properties of Se-Deficient Two-Dimensional MoSe₂. *ACS Nano* **9**, 3274-3283 (2015).

- 106 Ryu, G. H. *et al.* Atomic Structure and Dynamics of Self-Limiting Sub-Nanometer Pores in Monolayer WS₂. *ACS Nano* **12**, 11638-11647 (2018).
- 107 Hong, J. H. *et al.* Exploring Atomic Defects in Molybdenum Disulphide Monolayers. *Nat. Commun.* **6** (2015).
- 108 Zou, X. L., Liu, Y. Y. & Yakobson, B. I. Predicting Dislocations and Grain Boundaries in Two-Dimensional Metal-Disulfides from the First Principles. *Nano Lett.* **13**, 253-258 (2013).
- 109 Huang, Y. L. *et al.* Bandgap tunability at single-layer molybdenum disulphide grain boundaries. *Nat. Commun.* **6**, 6293 (2015).
- 110 Zou, X. L. & Yakobson, B. I. Metallic High-Angle Grain Boundaries in Monolayer Polycrystalline WS₂. *Small* **11**, 4503-4507 (2015).
- 111 Barja, S. *et al.* Charge Density Wave Order in 1D Mirror Twin Boundaries of Single-Layer MoSe₂. *Nat. Phys.* **12**, 751-756 (2016).
- 112 Komsa, H. P. & Krasheninnikov, A. V. Engineering the Electronic Properties of Two-Dimensional Transition Metal Dichalcogenides by Introducing Mirror Twin Boundaries. *Adv. Electron. Mater.* **3**, 1600468 (2017).
- 113 Dumcenco, D. *et al.* Large-Area Epitaxial Monolayer MoS₂. *Acs Nano* **9**, 4611-4620 (2015).
- 114 Shi, Y. M. *et al.* van der Waals Epitaxy of MoS₂ Layers Using Graphene As Growth Templates. *Nano Lett.* **12**, 2784-2791 (2012).
- 115 Yu, H. *et al.* Precisely Aligned Monolayer MoS₂ Epitaxially Grown on h-BN Basal Plane. *Small* **13**, 1603005 (2017).
- 116 Liu, H. J. *et al.* Dense Network of One-Dimensional Midgap Metallic Modes in Monolayer MoSe₂ and Their Spatial Undulations. *Phys. Rev. Lett.* **113**, 066105 (2014).
- 117 Zhou, S. *et al.* Atomically Sharp Interlayer Stacking Shifts at Anti-Phase Grain Boundaries in Overlapping MoS₂ Secondary Layers. *Nanoscale* **10**, 16692-16702 (2018).
- 118 Delley, B. An All-Electron Numerical-Method for Solving the Local Density Functional for Polyatomic-Molecules. *J. Chem. Phys.* **92**, 508-517 (1990).
- 119 Delley, B. From Molecules to Solids with the DMol³ Approach. *J. Chem. Phys.* **113**, 7756-7764 (2000).
- 120 Perdew, J. P., Burke, K. & Ernzerhof, M. Generalized Gradient Approximation Made Simple. *Phys. Rev. Lett.* **77**, 3865-3868 (1996).
- 121 Monkhorst, H. J. & Pack, J. D. Special Points for Brillouin-Zone Integrations. *Phys. Rev. B* **13**, 5188-5192 (1976).
- 122 Halgren, T. A. & Lipscomb, W. N. Synchronous-Transit Method for Determining Reaction Pathways and Locating Molecular Transition-States. *Chem. Phys. Lett.* **49**, 225-232 (1977).
- 123 Meyer, J. C. *et al.* Experimental Analysis of Charge Redistribution due to Chemical Bonding by High-Resolution Transmission Electron Microscopy. *Nat. Mater.* **10**, 209-215 (2011).

- 124 Schweiger, H., Raybaud, P., Kresse, G. & Toulhoat, H. Shape and Edge Sites Modifications of MoS₂ Catalytic Nanoparticles Induced by Working Conditions: A Theoretical Study. *J. Catal.* **207**, 76-87 (2002).
- 125 Bollinger, M. V., Jacobsen, K. W. & Norskov, J. K. Atomic and Electronic Structure of MoS₂ Nanoparticles. *Phys. Rev. B* **67**, 085410 (2003).
- 126 Morrissey, K. J. & Carter, C. B. Faceted Grain-Boundaries in Al₂O₃. *J. Am. Ceram. Soc.* **67**, 292-301 (1984).
- 127 Gao, J. *et al.* Aging of Transition Metal Dichalcogenide Monolayers. *ACS Nano* **10**, 2628-2635 (2016).
- 128 Liu, X. L., Balla, I., Bergeron, H. & Hersam, M. C. Point Defects and Grain Boundaries in Rotationally Commensurate MoS₂ on Epitaxial Graphene. *J. Phys. Chem. C* **120**, 20798-20805 (2016).
- 129 Jolie, W. *et al.* Tomonaga-Luttinger Liquid in a Box: Electrons Confined within MoS₂ Mirror-Twin Boundaries. *Phys. Rev. X* **9**, 011055 (2019).
- 130 Kim, C. *et al.* Fermi Level Pinning at Electrical Metal Contacts of Monolayer Molybdenum Dichalcogenides. *ACS Nano* **11**, 1588-1596 (2017).
- 131 Cutler, M. & Mott, N. F. Observation of Anderson Localization in an Electron Gas. *Phys Rev* **181**, 1336-1340 (1969).
- 132 Eda, G. *et al.* Coherent Atomic and Electronic Heterostructures of Single-Layer MoS₂. *ACS Nano* **6**, 7311-7317 (2012).
- 133 Bollinger, M. V. *et al.* One-Dimensional Metallic Edge States in MoS₂. *Phys. Rev. Lett.* **87**, 196803 (2001).
- 134 Tao, L. *et al.* Experimental and Theoretical Evidence for the Ferromagnetic Edge in WSe₂ Nanosheets. *Nanoscale* **9**, 4898-4906 (2017).
- 135 Saab, M. & Raybaud, P. Tuning the Magnetic Properties of MoS₂ Single Nanolayers by 3d Metals Edge Doping. *J. Phys. Chem. C* **120**, 10691-10697 (2016).
- 136 Yazyev, O. V. & Chen, Y. P. Polycrystalline Graphene and Other Two-Dimensional Materials. *Nat. Nanotechnol.* **9**, 755-767 (2014).
- 137 Jiang, L. L. *et al.* Soliton-Dependent Plasmon Reflection at Bilayer Graphene Domain Walls. *Nat. Mater.* **15**, 840-844 (2016).
- 138 Tapasztó, L. *et al.* Mapping the Electronic Properties of Individual Graphene Grain Boundaries. *Appl. Phys. Lett.* **100**, 053114 (2012).
- 139 Sitenko, Y. A. & Vlasii, N. D. Electronic Properties of Graphene with a Topological Defect. *Nucl. Phys. B* **787**, 241-259 (2007).
- 140 Li, Q. C. *et al.* Grain Boundary Structures and Electronic Properties of Hexagonal Boron Nitride on Cu(111). *Nano Lett.* **15**, 5804-5810 (2015).

- 141 Ju, L. *et al.* Topological valley transport at bilayer graphene domain walls. *Nature* **520**, 650-655 (2015).
- 142 Yin, L. J., Jiang, H., Qiao, J. B. & He, L. Direct Imaging of Topological Edge States at a Bilayer Graphene Domain Wall. *Nat. Commun.* **7**, 11760 (2016).
- 143 Abadi, R., Uma, R. P., Izadifar, M. & Rabczuk, T. The Effect of Temperature and Topological Defects on Fracture Strength of Grain Boundaries in Single-Layer Polycrystalline Boron-Nitride Nanosheet. *Comp. Mater. Sci.* **123**, 277-286 (2016).
- 144 Lin, J. H. *et al.* AC/AB Stacking Boundaries in Bilayer Graphene. *Nano Lett.* **13**, 3262-3268 (2013).
- 145 Alden, J. S. *et al.* Strain Solitons and Topological Defects in Bilayer Graphene. *P. Nat'l Acad. Sci. USA* **110**, 11256-11260 (2013).
- 146 San-Jose, P., Gorbachev, R. V., Geim, A. K., Novoselov, K. S. & Guinea, F. Stacking Boundaries and Transport in Bilayer Graphene. *Nano Lett.* **14**, 2052-2057 (2014).
- 147 He, J. G., Hummer, K. & Franchini, C. Stacking Effects on the Electronic and Optical Properties of Bilayer Transition Metal Dichalcogenides MoS₂, MoSe₂, WS₂, and WSe₂. *Phys. Rev. B* **89**, 075409 (2014).
- 148 Tao, P., Guo, H. H., Yang, T. & Zhang, Z. D. Stacking Stability of MoS₂ Bilayer: An *ab initio* Study. *Chinese Phys. B* **23**, 106801 (2014).
- 149 Azizi, A. *et al.* Freestanding van der Waals Heterostructures of Graphene and Transition Metal Dichalcogenides. *ACS Nano* **9**, 4882-4890 (2015).
- 150 Kresse, G. & Furthmuller, J. Efficient Iterative Schemes for *ab initio* Total-Energy Calculations Using a Plane-Wave Basis Set. *Phys. Rev. B* **54**, 11169-11186 (1996).
- 151 Grimme, S., Antony, J., Ehrlich, S. & Krieg, H. A Consistent and Accurate *ab initio* Parametrization of Density Functional Dispersion Correction (DFT-D) for the 94 Elements H-Pu. *J. Chem. Phys.* **132**, 154104 (2010).
- 152 Henkelman, G., Uberuaga, B. P. & Jonsson, H. A Climbing Image Nudged Elastic Band Method for Finding Saddle Points and Minimum Energy Paths. *J. Chem. Phys.* **113**, 9901-9904 (2000).
- 153 Kamaladasa, R. J. & Picard, Y. N. Basic Principles and Application of Electron Channeling in a Scanning Electron Microscope for Dislocation Analysis. *Microscopy: Science, Technology, Education and Applications* **4**, 1583 (2011).
- 154 Kuo, C. P., Vong, S. K., Cohen, R. M. & Stringfellow, G. B. Effect of Mismatch Strain on Band-Gap in III-V Semiconductors. *J. Appl. Phys.* **57**, 5428-5432 (1985).
- 155 Ly, T. H., Yun, S. J., Thi, Q. H. & Zhao, J. Edge Delamination of Monolayer Transition Metal Dichalcogenides. *ACS Nano* **11**, 7534-7541 (2017).
- 156 Zhang, D. *et al.* Probing Thermal Expansion Coefficients of Monolayers Using Surface Enhanced Raman Scattering. *RSC Adv.* **6**, 99053-99059 (2016).

- 157 Bollmann, W. *CRYSTAL DEFECTS AND CRYSTALLINE INTERFACES*. (Springer, 1970).
- 158 Choi, J. S. *et al.* Friction Anisotropy-Driven Domain Imaging on Exfoliated Monolayer Graphene. *Science* **333**, 607-610 (2011).
- 159 Long, F., Yasaei, P., Yao, W. T., Salehi-Khojin, A. & Shahbazian-Yassar, R. Anisotropic Friction of Wrinkled Graphene Grown by Chemical Vapor Deposition. *ACS Appl. Mater. Inter.* **9**, 20922-20927 (2017).
- 160 Lehtinen, O., Kurasch, S., Krasheninnikov, A. V. & Kaiser, U. Atomic Scale Study of the Life Cycle of a Dislocation in Graphene from Birth to Annihilation. *Nat. Commun.* **4**, 2098 (2013).
- 161 Nerl, H. C. *et al.* Probing the Local Nature of Excitons and Plasmons in Few-Layer MoS₂. *npj 2D Materials and Applications* **1**, 2 (2017).
- 162 Johari, P. & Shenoy, V. B. Tunable Dielectric Properties of Transition Metal Dichalcogenides. *ACS Nano* **5**, 5903-5908 (2011).
- 163 Tongay, S. *et al.* Thermally Driven Crossover from Indirect Toward Direct Bandgap in 2D Semiconductors: MoSe₂ versus MoS₂. *Nano Lett.* **12**, 5576-5580 (2012).
- 164 Zhao, W., Li, Y. C., Duan, W. H. & Ding, F. Ultra-Stable Small Diameter Hybrid Transition Metal Dichalcogenide Nanotubes X-M-Y (X, Y = S, Se, Te; M = Mo, W, Nb, Ta): A Computational Study. *Nanoscale* **7**, 13586-13590 (2015).
- 165 Kushima, A., Qian, X. F., Zhao, P., Zhang, S. L. & Li, J. Rippllocations in van der Waals Layers. *Nano Lett.* **15**, 1302-1308 (2015).
- 166 Li, J. *et al.* Gate-Controlled Topological Conducting Channels in Bilayer Graphene. *Nat. Nanotechnol.* **11**, 1060-1065 (2016).
- 167 Kisslinger, F. *et al.* Linear Magnetoresistance in Mosaic-like Bilayer Graphene. *Nat. Phys.* **11**, 650-653 (2015).
- 168 Schweizer, P., Dolle, C. & Spiecker, E. *In Situ* Manipulation and Switching of Dislocations in Bilayer Graphene. *Sci. Adv.* **4**, eaat4712 (2018).
- 169 Zhang, F., Li, W., Ma, Y. Q., Tang, Y. N. & Dai, X. Q. Tuning the Schottky Contacts at the Graphene/WS₂ Interface by Electric Field. *RSC Adv.* **7**, 29350-29356 (2017).
- 170 Lee, C. S. *et al.* Fabrication of Metal/Graphene Hybrid Interconnects by Direct Graphene Growth and Their Integration Properties. *Adv. Electron. Mater.* **4**, 1700624 (2018).
- 171 Lin, Y. C. *et al.* Atomically Thin Heterostructures Based on Single-Layer Tungsten Diselenide and Graphene. *Nano Lett.* **14**, 6936-6941 (2014).
- 172 Tonndorf, P. *et al.* Photoluminescence Emission and Raman Response of Monolayer MoS₂, MoSe₂, and WSe₂. *Opt. Express* **21**, 4908-4916 (2013).
- 173 Rosenberg, F., Ionescu, E., Nicoloso, N. & Riedel, R. High-Temperature Raman Spectroscopy of Nano-Crystalline Carbon in Silicon Oxycarbide. *Materials* **11**, 93 (2018).
- 174 Chen, S. *et al.* Origin of Ultrafast Growth of Monolayer WSe₂ via Chemical Vapor Deposition. *npj Comput. Mater.* **5**, 28 (2019).

- 175 Favia, P. *et al.* Nanobeam Diffraction: Technique Evaluation and Strain Measurement on Complementary Metal Oxide Semiconductor Devices. *J. Electrochem. Soc.* **158**, 438-446 (2011).
- 176 Addou, R. *et al.* One Dimensional Metallic Edges in Atomically Thin WSe₂ Induced by Air Exposure. *2D Mater.* **5**, 025017 (2018).
- 177 Li, Q. H. *et al.* Ohmic Contacts Between Monolayer WSe₂ and Two-Dimensional Titanium Carbides. *Carbon* **135**, 125-133 (2018).
- 178 Shi, Y. M. *et al.* Selective Decoration of Au Nanoparticles on Monolayer MoS₂ Single Crystals. *Sci. Rep.-Uk* **3**, 1839 (2013).
- 179 Rao, B. G., Matte, H. S. S. R. & Rao, C. N. R. Decoration of Few-Layer Graphene-Like MoS₂ and MoSe₂ by Noble Metal Nanoparticles. *J. Clust. Sci.* **23**, 929-937 (2012).
- 180 Lee, J. S. *et al.* Wafer-Scale Single-Crystal Hexagonal Boron Nitride Film *via* Self-Collimated Grain Formation. *Science* **362**, 817-821 (2018).
- 181 Li, Y. *et al.* Site-Specific Positioning and Patterning of MoS₂ Monolayers: The Role of Au Seeding. *ACS Nano* **12**, 8970-8976 (2018).
- 182 Lu, W. J. *et al.* Engineering Graphene Wrinkles for Large Enhancement of Interlaminar Friction Enabled Damping Capability. *ACS Appl. Mater. Inter.* **11**, 30278-30289 (2019).
- 183 Bao, W. Z. *et al.* Controlled Ripple Texturing of Suspended Graphene and Ultrathin Graphite Membranes. *Nat. Nanotechnol.* **4**, 562-566 (2009).
- 184 Jaramillo, T. F. *et al.* Identification of Active Edge Sites for Electrochemical H₂ Evolution from MoS₂ Nanocatalysts. *Science* **317**, 100-102 (2007).
- 185 Guo, M. *et al.* Edge Dominated Electronic Properties of MoS₂/Graphene Hybrid 2D Materials: Edge State, Electron Coupling and Work Function. *J. Mater. Chem. C* **5**, 4845-4851 (2017).

*Chapter 2.3.2 is reproduced in part with permission of “The Hide-and-Seek of Grain Boundaries from Moiré Pattern Fringe of Two-Dimensional Graphene”, *Scientific Reports*, 5, 12508 (2015). Copyright 2015 Springer Nature.

*Chapter 4 is reproduced in part with permission of “Interface-Driven Partial Dislocation Formation in 2D Heterostructures”, *Advanced Materials*, 31, 1807486 (2019). Copyright 2019 WILEY-VCH.

CURRICULUM VITAE

JUNG HWA KIM

ADDRESS	50 UNIST-Gil, Ulsan 44919, South Korea	SCHOOL	School of Materials Science and Engineering
BIRTHDAY	May 11 th , 1991	AFFILIATION	Ulsan National Institute Science and Technology (UNIST)
EMAIL	kjh1113@unist.ac.kr	PHONE	+82-10-5655-9818
RESEARCH PROFILE	https://orcid.org/0000-0002-2615-963X https://www.researchgate.net/profile/Jung_Hwa_Kim		

EDUCATION

Mar 2014 ~ Feb 2020	Combined M.S. & Ph.D. in Materials Science and Engineering Ulsan National Institute of Science and Technology, Republic of Korea Advisor: Prof. Zonghoon Lee (zhlee@unist.ac.kr, http://ASEMlab.org) (Dissertation title: Study on Growth of Two-Dimensional Transition Metal Dichalcogenides on Graphene: The Interface-Driven Defects and Properties Relationship)
Mar 2010 ~ Feb 2014	B.S. in Materials Science and Engineering Ulsan National Institute of Science and Technology, Republic of Korea

RESEARCH EXPERIENCES

Mar 2014 ~ Feb 2020	Ph.D. student in Prof. Zonghoon Lee's Group (Atomic-Scale Electron Microscopy (ASEM) Lab.) Ulsan National Institute of Science and Technology, Republic of Korea
Mar 2012 ~ Feb 2014	Undergraduate intern in Prof. Zonghoon Lee's Group Ulsan National Institute of Science and Technology, Republic of Korea

PUBLICATIONS

1. **J.H. Kim**, S.-Y. Kim, Y. Cho, H.J. Park, H.-J. Shin, S.-Y. Kwon, and Z. Lee, "Interface-driven formation of partial dislocations in two-dimensional heterostructures," *Advanced Materials*, 31, 1807486, February 2019.
2. K. Kim[§], **J.H. Kim**[§], B.-E. Park, H. Kim, and Z. Lee, "Direct observation of leakage currents in a metal-insulator-metal capacitor using in-situ transmission electron microscopy," *Nanotechnology*, 29, 435705, August 2018.
- [§]Co-first author
3. **J.H. Kim**, K. Kim, and Z. Lee, "The hide-and-seek of grain boundaries from moiré pattern fringe of two-dimensional graphene," *Scientific Reports*, 5, 12508, July 2015.
4. H.J. Park, J. Cha, M. Choi, **J.H. Kim**, R.Y. Tay, E.H.T. Teo, N. Park, S. Hong, Z. Lee, "One-Dimensional Hexagonal Boron Nitride Conducting Channel," *Science Advances*, accepted.
5. Y. Choi, K. Kim, S.Y. Lin, J. Kim, J.M. Park, **J.H. Kim**, Z. Lee, and H. Cheong, "Complete determination of the crystallographic orientation of ReX₂ (X=S, Se) by polarized Raman spectroscopy," online published, *Nanoscale Horizons*, DOI: 10.1039/c9nh00487d.
6. H.J. Park, R.Y. Tay, X. Wang, W. Zhao, **J.H. Kim**, R.S. Ruoff, F. Ding, E.H.T. Teo, and Z. Lee, "Screw dislocation-driven growth of double-spiral hexagonal boron nitride," *Nano Letters*, 19, 4229-4236, July 2019.
- Selected as a Journal Cover of July 2019.
7. Y.R. Lim, J.K. Han, Y. Yoon, J.-B. Lee, C. Jeon, M. Choi, H. Chang, N. Park, **J.H. Kim**, Z. Lee, W. Song, S. Myung, S.S. Lee, K.-S. An, J.-H. Ahn, and J. Lim, "Atomic-Level Customization of 4 in. Transition Metal Dichalcogenide Multilayer Alloys for Industrial Applications," *Advanced Materials*, 1901405, June 2019.
8. K. Kim, J.C. Yoon, J. Kim, **J.H. Kim**, S.W. Lee, A. Yoon, and Z. Lee, "Dedicated preparation for in situ transmission electron microscope tensile testing of exfoliated graphene," *Applied Microscopy*, 49, 1-7, April 2019.
9. S. Song, S.-Y. Kim, J. Kwak, Y. Jo, **J.H. Kim**, J.H. Lee, J.-U. Lee, J.U. Kim, H.D. Yun, Y. Sim, D.H. Lee, S.-H. Seok, T.-I. Kim, H. Cheong, Z. Lee, and S.-Y. Kwon, "Electrically robust single-crystalline WTe₂ nanobelts for nanoscale electrical interconnects," *Advanced Science*, 6, 1801370, December 2018.
- Featured as Journal Frontpiece Article (Vol. 6, Issue:3)

10. S.-Y. Kim, **J.H. Kim**, S. Lee, J. Kwak, Y. Jo, E. Yoon, G.-D. Lee, Z. Lee, and S.-Y. Kwon, “The impact of substrate surface defects on the properties of two-dimensional van der Waals heterostructures,” *Nanoscale*, 10, 19212-19219, September 2018.
- Featured as Editor’s Choice: van der Waals heterostructures
11. K.Y. Ko, S. Lee, K. Park, Y. Kim, W.J. Woo, D. Kim, J.-G. Song, J. park, **J.H. Kim**, Z. Lee, H. Kim, “High-Performance Gas Sensor Using a Large-Area $\text{WS}_{2x}\text{Se}_{2-2x}$ Alloy for Low-Power Operation Wearable Applications,” *ACS Appl. Mater. Interfaces*, 10, 34163-34171, September 2018.
12. J. Kwak, Y. Jo, S. Song, **J.H. Kim**, S.-Y. Kim, J.-U. Lee, S. Lee, J. Park, G.-D. Lee, J.-W. Yoo, S.Y. Kim, Y.-M. Kong, G.-H. Lee, W.-G. Lee, X. Xu, H. Cheong, E. Yoon, Z. Lee, and S.-Y. Kwon, “Single-crystalline nanobelts composed of transition metal ditellurides,” *Advanced Materials*, 1707260, June 2018.
- Highlighted in Media and Newspapers
13. H. Bark, Y. Choi, J. Jung, **J.H. Kim**, H. Kwon, J. Lee, Z. Lee, J.H. Cho, and C. Lee, “Large-area niobium disulfide thin films as transparent electrodes for devices based on two-dimensional materials,” *Nanoscale*, 10, 1056-1062, December 2017.
14. H. Jeong, S. Yoon, **J.H. Kim**, D.-H. Kwak, S.H. Heo, D.H. Gu, H. Kim, S. Park, H.W. Ban, J. Park, Z. Lee, J.-S. Lee, K. An, and J.S. Son, “Transition metal-based thiometallates for surface functionalization of nanocrystals,” *Chemistry of Materials*, 29 (24), 10510-10517, November 2017.
15. J. Lee, T.Y. Ko, **J.H. Kim**, H. Bark, B. Kang, S.-G. Jung, T. Park, Z. Lee, S. Ryu, and C. Lee, “Structural and optical properties of single- and few-layer magnetic semiconductor CrPS_4 ,” *ACS Nano*, 11, 10935-10944, October 2017.
16. N.Y. Kim, H.Y. Jeong, **J.H. Kim**, G. Kim, H.S. Shin, and Z. Lee, “Evidence of local commensurate state with lattice match of graphene on hexagonal boron nitride,” *ACS Nano*, 11(7), 7084-7090, June 2017.
17. H.K. Hong, J. Jo, D. Hwang, J. Lee, N.Y. Kim, S. Son, **J.H. Kim**, M.J. Jin, Y.C. Jun, R. Erni, S.K. Kwak, J.W. Yoo, and Z. Lee, “Atomic scale study on growth and heteroepitaxy of ZnO monolayer on graphene,” *Nano Letters*, 17(1), 120–127, December 2017.
18. K. Akbar, **J.H. Kim**, Z. Lee, M. Kim, Y. Yi, and S.H. Chun, “Superaerophobic graphene nano-hills for direct hydrazine fuel cells,” *NPG Asia Materials*, 9, e378, May 2016.

19. Y.W. Park, S.K. Jerng, J.H. Jeon, S.B. Roy, K. Akbar, J. Kim, Y. Sim, M.J. Seong, **J.H. Kim**, Z. Lee, M. Kim, Y.Yi, J. Kim, D.Y. Noh, and S.H. Chun, “Molecular beam epitaxy of large-area SnSe₂ with monolayer thickness fluctuation,” *2D Materials*, 4, 014006, January 2016
20. S.-Y. Kim, J. Kwak, **J.H. Kim**, J.-U. Lee, Y. Jo, S.Y. Kim, H. Cheong, Z. Lee, and S.-Y. Kwon, “Substantial improvements of long-term stability in encapsulation-free WS₂ using highly interacting graphene substrate,” *2D Materials*, 4, 011007, December 2016.
21. M. Kim, S. Han, **J.H. Kim**, J.-U. Lee, Z. Lee, and H. Cheong, “Determination of the thickness and orientation of few-layer tungsten ditelluride using polarized Raman spectroscopy,” *2D Materials*, 3, 034004, August 2016.
22. **J.H. Kim**, and Z. Lee, “Silicene of two-dimensional materials: formation of heterostructure,” *Applied Microscopy*, 44(4), pp.123-132, December 2014. (*review article*)

PATENTS

Korea Patents

1. Z. Lee, K. Kim, **J.H. Kim**, M. Choe, “Graphene tensile testing method”, Korea Patent No. 10-2017-0108128, August 2017

ON-GOING RESEARCH (MANUSCRIPTS IN PREPARATION)

1. Antiphase Boundaries as Faceted metallic wires in Two-dimensional Transition Metal Dichalcogenides, *Under Consideration*.
2. The impact of substrate crystallinity on growth behavior of transition metal dichalcogenides
3. Ultimate brittle fracture in anisotropic two-dimensional materials
4. Phase transformation of rhenium disulfide using *in situ* heating

RESEARCH INTERESTS

- **Atomic-scale imaging, spectroscopy, simulation** on aberration corrected TEM/STEM
- **Relationship between microstructures and properties** of 2D crystals and van der Waals heterostructures
- **Study on growth mechanism of transition metal dichalcogenides on other 2D crystals**
- **Manipulation of nanostructures and defect engineering** using various chemical and physical methods
- ***in situ* TEM**: study on growth mechanism, novel nanostructure and property transition under the external stimulus
- **Various phases of transition metal dichalcogenides (TMDs)**: Metallic (WTe₂, 1T-TaS₂), Semiconducting (ReS₂, ReSe₂, MoS₂, WS₂, WSe₂, MoTe₂, GaSe), Alloys, Doped structure, heterostructure

TECHNICAL EXPERIENCE

Atomic-Resolution Transmission Electron Microscopy (TEM)

1. Atomic imaging of 2D materials using **aberration corrected TEM**
 - 1) **FEI Titan G2 (60-300)**
 - Double aberration corrector
 - Monochromator
 - 2) **JEOL 2100F**
 - Probe corrector
2. Spectroscopic analysis
 - 1) **Electron Energy Loss Spectroscopy (EELS)**
 - Energy resolution: 0.16 eV
 - 2) **Energy dispersive X-ray spectroscopy (EDS)**

Simulation

1. **Atomic modeling** using VESTA and Jmol (freeware)
2. **TEM/STEM image and Bloch-wave simulations** using MacTempasX and JEMS

Synthesis and Thin Film Deposition

1. Synthesis of high-quality graphene by **chemical vapor deposition (CVD)** and **inductively coupled plasma CVD** method
2. **Chemical and Mechanical exfoliation** for obtaining transition metal dichalcogenides sheet
3. Thin film deposition using **PECS (Precision Etching and Coating System)** and **Sputter**
4. Manipulation of novel phase of 2D materials using *in situ* heating

Modification of Materials using Chemical and Physical Methods

1. **Plasma treatments** on 2D materials (physical method)
2. **UV/Ozone treatments** on 2D materials (chemical method)

Other Analytical Equipment

1. **Focused Ion Beam (FIB)**
- TEM cross-section sample prep, site-specific analysis, Pt / C deposition, ablation of materials
2. **Scanning Electron Microscopy (SEM)**
- analyzing morphology and composition of solid materials
3. Raman, *in situ* Raman (temperature; 77 K–873 K), PL, UV-Vis spectroscopy
4. X-ray Powder Diffraction (XRD)
5. Electrical characterization (4-point probe, IV characteristic)

CONFERENCE PRESENTATIONS

Conference Proceedings / Extended Abstracts

1. **J.H. Kim**, K. Kim, and Z. Lee, “The Identification of Grain Boundaries in Two-dimensional Graphene using Moire Pattern Fringe,” *Microscopy 2015*, 64, November 24-27, 2015, Himeji, Japan, pp. i40.
2. **J.H. Kim**, S.-Y. Kim, H.J. Park, S.-Y. Kwon, and Z. Lee, “Monolayer-like Behavior of Bilayer Transition-Metal Dichalcogenides,” *Microscopy & Microanalysis 2019*, Portland, United States

Presentations

1. **J.H. Kim**, S.-Y. Kim, H.J. Park, S.-Y. Kwon, Z. Lee, "Interface-Driven Stacking Boundaries in Bilayer Transition Metal Dichalcogenides," The 5th International Conference on Advanced Electromaterials (ICAE 2019), Nov. 5-8, 2019, Jeju, Korea (Poster)
2. **J.H. Kim**, S.-Y. Kim, H.J. Park, S.-Y. Kwon, Z. Lee, "Monolayer-like Behavior of Bilayer Transition-Metal Dichalcogenides," Microscopy and Microanalysis (M&M), Aug 4-8, 2019, Portland, United States (Oral)
3. **J.H. Kim**, S.-Y. Kim, Y. Cho, H.J. Park, H.-J. Shin, S.-Y. Kwon, Z. Lee, "Dislocations in Bilayer Transition Metal Dichalcogenides: Effects of Morphological Defects in Substrate", The 6th Korean Graphene Symposium, Mar 28-29, 2019, Buyeo, Korea (Poster)
4. S. Song, Y. Sim, S.-Y. Kim, **J.H. Kim**, I. Oh, W.K. Na, D.H. Lee, J. Wang, H. Cheong, J.-W. Yoo, Z. Lee, and S.-Y. Kwon, "Atomically Thin Transition-Metal Tellurides Electrodes toward Schottky Barrier-Tunable Field Effect Transistors", The 5th International Conference on Advanced Electromaterials (ICAE 2019), Nov. 5-8, 2019, Jeju, Korea (Oral)
5. H.J. Park, J. Cha, **J.H. Kim**, R.Y. Tay, E.H.T. Teo, S. Hong, Z. Lee, "One-Dimensional Hexagonal Boron Nitride Semiconductor", International Microscopy Conference 19, Sep 09-14, 2018, Sydney, Australia (Oral)
6. H.J. Park, **J.H. Kim**, Z. Lee, "Screw Dislocation-Driven Growth of Double-Helical Hexagonal Boron Nitride", International Microscopy Conference 19, Sep 09-14, 2018, Sydney, Australia (Poster)
7. **J.H. Kim**, S.-Y. Kim, Y. Cho, H.-J. Shin, H.J. Park, S.-Y. Kwon, Z. Lee, "Dislocations in Bilayer Transition Metal Dichalcogenides", International Microscopy Conference 19, Sep 09-14, 2018, Sydney, Australia (Poster)
8. H.J. Park, **J.H. Kim**, Z. Lee, "Screw-Dislocation Driven Growth of Multilayer Hexagonal Boron Nitride", 2018 Korean Society of Microscopy Conference, Jun 20-22, 2018, Jeju, Korea (Poster)
9. N.Y. Kim, **J.H. Kim**, Z. Lee, "Evidence of Local Lattice Match for Commensurate State of Graphene/hBN van der Waals Heterostructure with TEM Analysis", 2018 Korean Society of Microscopy Conference, Jun 20-22, 2018, Jeju, Korea (Poster)
10. K. Kim, **J.H. Kim**, J.C. Yoon, S.W. Lee, A. Yoon, Z. Lee, "In-situ TEM experiments for exfoliated graphene sheets", The 5th Korean Graphene Symposium, Mar 29-30, 2017, Buyeo, Korea (Poster)
11. Y. Lee, H.S. Kim, J. Lee, S. Ramzan, S. Son, **J.H. Kim**, N.Y. Kim, Y. Kim, Z. Lee, "Surface Oxidation of Atomically Thin MoS₂ by UVO treatment", Korea Global Ph.D. Fellowship Conference, Dec 14-15, 2017, Seoul, Korea (Oral)
12. K. Kim, **J.H. Kim**, J.C. Yoon, S.W. Lee, A. Yoon, Z. Lee, "In-situ TEM experiments for exfoliated graphene sheets", The 10th International Conference on Advanced Materials and Devices, Dec 5-8, 2017, Jeju, Korea (Poster)

13. N.Y. Kim, H.Y. Jeong, **J.H. Kim**, G. Kim, H.S. Shin, Z. Lee, “Evidence of local lattice match of graphene on hexagonal boron nitride”, The 10th International Conference on Advanced Materials and Devices, Dec 5-8, 2017, Jeju, Korea (Poster)
14. S.-Y. Kim, J. Kwak, **J.H. Kim**, J.-U. Lee, Y. Jo, S.Y. Kim, H. Cheong, Z. Lee, S.-Y. Kwon, “Highly enhanced air stability of monolayer WS₂ with graphene substrate”, The 10th International Conference on Advanced Materials and Devices, Dec 5-8, 2017, Jeju, Korea (Poster)
15. S. Song, J. Kwak, J.H. Lee, J.-U. Lee, S.-Y. Kim, **J.H. Kim**, S. Lee, Y. Sim, Y. Jo, G.-D. Lee, H. Cheong, E. Yoon, Z. Lee, S.-Y. Kwon, “Single-crystalline 1D WTe₂ nanobelts grown from eutectic alloy reservoir”, The 10th International Conference on Advanced Materials and Devices, Dec 5-8, 2017, Jeju, Korea (Poster)
16. S. Song, J. Kwak, J.H. Lee, J.-U. Lee, S.-Y. Kim, **J.H. Kim**, S. Lee, Y. Sim, Y. Jo, G.-D. Lee, H. Cheong, E. Yoon, Z. Lee, S.-Y. Kwon, “Single-Crystalline Tungsten Ditelluride (WTe₂) Nanobelts Grown from Eutectic Alloy Reservoir”, 2017 Fall Materials Research Society, Nov 26 – Dec 1, 2017, Boston, United States (Poster)
17. **J.H. Kim**, S.-Y. Kim, H.J. Park, S.-Y. Kwon, Z. Lee, “Direct Growth of Bilayer WS₂ with Topological Defects induced by Morphological Defects of Graphene”, The 3rd East-Asia Microscopy Conference, Nov 7-11, 2017, Busan, Korea (Poster)
18. K. Kim, **J.H. Kim**, J.C. Yoon, S.W. Lee, A. Yoon, Z. Lee, “In-situ TEM experiments for exfoliated graphene sheets”, The 3rd East-Asia Microscopy Conference, Nov 7-11, 2017, Busan, Korea (Poster)
19. N.Y. Kim, H.Y. Jeong, **J.H. Kim**, G. Kim, H.S. Shin, Z. Lee, “Evidence of Local Lattice Match for Commensurate State of Graphene on Hexagonal Boron Nitride”, The 3rd East-Asia Microscopy Conference, Nov 7-11, 2017, Busan, Korea (Oral)
20. H.J. Park, X. Wang, W. Zhao, **J.H. Kim**, F. Ding, Z. Lee, “Screw-Dislocation Driven Growth of Multilayer Hexagonal Boron Nitride”, The 3rd East-Asia Microscopy Conference, Nov 7-11, 2017, Busan, Korea (Oral)
21. Y. Lee, H.S. Kim, J. Lee, S. Ramzan, S. Son, **J.H. Kim**, N.Y. Kim, Y. Kim, Z. Lee, “Surface Oxidation of Atomically Thin MoS₂ by UVO treatment”, The 3rd East-Asia Microscopy Conference, Nov 7-11, 2017, Busan, Korea (Poster)
22. H.K. Hong, J. Lee, N.Y. Kim, S. Son, **J.H. Kim**, R. Erni, Z. Lee, “Atomic Scale Study on Growth and Heteroepitaxy of ZnO Monolayer on Graphene”, European Microbeam Analysis Society & International Union of Microbeam Analysis Societies, May 7-11, 2017, Konstanz, Germany (Oral, Poster)
23. N.Y. Kim, **J.H. Kim**, Z. Lee, “Distribution of superlattice domains in stacked graphene on hBN”, The 4th Korean Graphene Symposium, Apr 6-7, 2017, Buyeo, Korea (Poster)
24. Y. Lee, S. Son, **J.H. Kim**, N.Y. Kim, Z. Lee, “Surface Oxidation of Atomically Thin MoS₂ by UVO treatment”, The 4th Korean Graphene Symposium, Apr 6-7, 2017, Buyeo, Korea (Poster)

25. S.-Y. Kim, J. Kwak, **J.H. Kim**, J.-U. Lee, Y. Jo, S.Y. Kim, H. Cheong, Z. Lee, S.-Y. Kwon, "Improved Air-Stability of Encapsulation-Free, Monolayer WS₂ Using Graphene Substrate", The 24th Korean Conference on Semiconductors, Feb 13-15, 2017, Hongcheon, Korea (Oral)
26. S.-Y. Kim, J. Kwak, **J.H. Kim**, J.-U. Lee, Y. Jo, S.Y. Kim, H. Cheong, Z. Lee, S.-Y. Kwon, "Encapsulation-Free Highly Air-Stable Monolayer WS₂ Using Graphene Substrate", Korean Material Society Conference, Nov 17-18, 2016, Gyeongju, Korea (Oral)
27. S. Lim, J.-U. Lee, H. Cheong, **J.H. Kim**, Z. Lee, N.T.T. Huong, S.-L. Cho, "Raman study of stacking order in 2-dimensional GaSe", Korean Physics Society Conference, Oct 19-21, 2016, Gwangju, Korea (Oral)
28. H.K. Hong, J. Jo, D. Hwang, J. Lee, N.Y. Kim, S. Son, **J.H. Kim**, M. Jin, Y.C. Jun, R. Erni, S.K. Kwak, J.W. Yoo, Z. Lee, "Epitaxial Grown Monolayer ZnO on Graphene", International Symposium on microscopy and microanalysis of materials, Sep 23-26, 2016, Nanjing, China (Poster)
29. H.K. Hong, J. Jo, D. Hwang, J. Lee, N.Y. Kim, S. Son, **J.H. Kim**, M. Jin, Y.C. Jun, R. Erni, S.K. Kwak, J.W. Yoo, Z. Lee, "Epitaxially Grown Single-atom-thick Layer of ZnO on Graphene", Korean Society of Microscopy Conference, Jun 2-3, 2016, Gumi, Korea (Oral)
30. M. Kim, **J.H. Kim**, J.-U. Lee, Z. Lee, H. Cheong, "Polarization and thickness dependent Raman spectrum of WTe₂", the 3rd Korean Graphene Symposium, Apr 14-15, 2016, Buyeo, Korea (Poster)
31. H.K. Hong, J. Jo, D. Hwang, J. Lee, N.Y. Kim, S. Son, **J.H. Kim**, M. Jin, Y.C. Jun, R. Erni, S.K. Kwak, J.W. Yoo, Z. Lee, "Epitaxially Grown Monolayer ZnO on Graphene", the 3rd Korean Graphene Symposium, Apr 14-15, 2016, Buyeo, Korea (Oral)
32. **J.H. Kim**, K. Kim, Z. Lee, "The Identification of Grain Boundaries in Two-Dimensional Graphene Using Moire Pattern Fringe", The 2nd East Asia Microscopy Conference (EAMC2), Nov 24-27, 2015, Himeji, Japan (Oral)
33. G.H. Ryu, H.J. Park, **J.H. Kim**, N.Y. Kim, Z. Lee, "Characterization of Defects in 2D Materials at Atomic Scale using Aberration Corrected Transmission Electron Microscopy", International Symposium on Microscopy & Microanalysis of Materials, Nov 11-14, 2015, Changwon, Korea (Invited)
34. G.H. Ryu, H.J. Park, **J.H. Kim**, N.Y. Kim, Z. Lee, "Characterization of Defects in 2D Materials at Atomic Scale using Aberration Corrected Transmission Electron Microscopy", Dasan Conference, Dimensional Properties Materials Research, Nov 2-4, 2015, Jeju, Korea (Invited)
35. G.H. Ryu, H.J. Park, N.Y. Kim, **J.H. Kim**, H.K. Hong, Z. Lee, "Atomic-scale Research on 2D Materials using Aberration-corrected TEM", 2015 Collaborative Conference on 3D and Materials Research, Jun 15-19, 2015, Korea (Invited)
36. **J.H. Kim**, K. Kim, Z. Lee, "Observation of Grain Boundaries from Moire Fringe of Two-dimensional Graphene", Korean Society of Microscopy Conference, May 28-29, 2015, Seoul, Korea (Poster)

37. **J.H. Kim**, S.W. Lee, Z. Lee, “The hide-and-seek of grain boundaries from moire pattern fringe of two-dimensional graphene”, the 2nd Korean Graphene Symposium, Mar 26-27, 2015, Buyeo, Korea (oral)
38. G.H. Ryu, **J.H. Kim**, S. Son, H.J. Park, K.Kim, M.J. Lee, N.Y. Kim, H. Hong and Z. Lee, "Investigation of stacking structure and grain boundary of bilayer 2D materials using aberration-corrected TEM", Korean Society of Microscopy Conference, May 22-23, 2014, Jeonju, Korea (Poster)
39. G.H. Ryu, H.J. Park, N.Y. Kim, **J.H. Kim**, K.Kim, M.J. Lee, S. Son , H. Hong and Z. Lee, "Investigation of stacking structure and grain boundary of bilayer 2D materials using aberration-corrected TEM", the 1st Korean Graphene Symposium, Apr 3-4, 2014, Buyeo, Korea (Poster)
40. G.H. Ryu, H.J. Park, N.Y. Kim, **J.H. Kim**, K.Kim, M.J. Lee and Z. Lee, "Investigation of stacking structure and defects of bilayer graphene using aberration corrected TEM", International Conference of Surface Engineering, ICSE2013, Nov 18-21, 2013, Korea

ACTIVITIES / AWARDS

- **Global Ph. D. Fellowship (GPF)** sponsored by National Research Foundation of Korea.
 - Title: Atomic-Scale Property Visualization of Layered 2D Materials: Bridging between Microstructure and Properties with Phase-Contrast
 - Received for 2015-2020
- **The Scientific Photo Award (Gold medal)** sponsored by FEI Company, Hitachi High-Tech Co., Jeonju, Korea, 2014.
- **Best Poster Award** in Microscopy Conference, Jeonju, Korea, 2014, “Investigation of stacking structure and grain boundary of bilayer 2D materials using aberration-corrected TEM.”
- **Excellent Award** in 2015 University Invention Contest, Seoul, Korea, 2015.
- **Best Poster Award** in Korean Graphene Symposium, Buyeo, Korea, 2016, “Polarization and thickness dependent Raman spectrum of WTe₂.”
- **Best Oral Presentation Award** in Korean Graphene Symposium, Buyeo, Korea, 2016, “Epitaxially Grown Monolayer ZnO on Graphene.”
- **Best Poster Award** in International Symposium on microscopy and microanalysis of materials, Nanjing, China, 2016, “Epitaxial Grown Monolayer ZnO on Graphene.”
- **Best Poster Award** in the 4th Korean Graphene and 2D Materials Symposium, Buyeo, Korea, 2017, “Distribution of superlattice domains in stacked graphene on hBN.”

- **Early Career Scholarship** sponsored by European Microbeam Analysis Society & International Union of Microbeam Analysis Societies, Konstanz, Germany, 2017, “Atomic Scale Study on Growth and Heteroepitaxy of ZnO Monolayer on Graphene.”
- **Best Poster Award** in Microscopy Conference, Jeju, Korea, 2018, “Screw-Dislocation Driven Growth of Multilayer Hexagonal Boron Nitride.”
- **Best Poster Award** in the 6th Korean Graphene and 2D Materials Symposium, Buyeo, Korea, 2019, “Dislocations in Bilayer Transition Metal Dichalcogenides: Effects of Morphological Defects in Substrate.”
- **Best Poster Award (Gold)** in the 5th International Conference on Advanced Electromaterials, Jeju, Korea, 2019, “Interface-Driven Stacking Boundaries in Bilayer Transition Metal Dichalcogenides.”

EDUCATION CERTIFICATE

Period	Education	Educational institution
2015.04.28-2015.04.29	2015 TEM Advanced Course Workshop (GERI, Gumi)	Korean Society of Microscopy
	Education of fundamental principle and various applications of Transmission Electron Microscope	
2015.07.21-2015.07.24	The 22 nd TEM Workshop (KIST, Jeonbuk)	Korean Society of Microscopy
	Training using aberration corrected Transmission Electron Microscope	
2017.12.05-2017.12.07	Gatan EELS & EFTEM Analysis School (Korea)	Gatan Inc.
	Training of EELS and EFTEM	

RESEARCH PROJECT PARTICIPATED

1. Atomic-scale Property Visualization of Layered 2D Materials: Bridging between Microstructure and Properties with Phase-Contrast, Global Ph.D Fellowship Program, National Research Foundation, S. Korea (2015.03.01 - 2020.02.29).
2. In situ study of induced defects in binary 2D materials at atomic scale, National Research Foundation, S. Korea (2015.05.01 ~ 2018.04.30)
3. In Situ TEM Study of Structural Properties in 2D Materials, National Research Foundation, S. Korea (2018.03.01 ~ 2020.02.29)